Department of Precision and Microsystems Engineering

Quench Detection Study for a HTS Model Dipole Magnet

Kristiaan Broekens

Report no	: 25
Coach	: Glyn Kirby, Gijs de Rijk (CERN)
Professor	: Fred van Keulen
Specialisation	: Engineering Mechanics, Mechatronics
Type of report	: Master Thesis
Date	: 14/10/2016

Delft University of Technology

Challenge the future

ABSTRACT

Future high-energy physics demands higher magnetic fields to attain higher beam energies and thus needs novel superconducting materials in accelerator magnet applications. Current superconductors operate in the temperature range between 1.8 and 4.2 K and attain 8 T in modern operational machines. Meanwhile, prototypes have been built to operate up to 12 T, which approaches the foreseen maximum attainable practical dipole field of 16 T of modern low temperature superconductors. In the framework of the long-term European development project Eucard-2, within the work package 'Future Magnets', the technology for dipole magnets in the 16 to 20 Tesla range is explored. High Temperature Superconductor (HTS) materials have the ability to provide these high magnetic fields, but are in an early stage of development. In the recent past, significant improvements have been achieved by increasing current density and reducing cost, which implies the conductors' future potential.

The superconducting regime stretches much higher in both temperature and flux density compared to modern Low Temperature Superconductors (LTS), offering a new range of operating regimes. Higher current densities can be reached at the same operating temperature or, equal current densities can be reached at higher temperatures. The increased operating current density reduces the required conductor volume which leads, consequently, to more compact designs, while a higher operating temperature poses less restraints on the cryogenic cooling facilities. This versatility offers great potential for future magnet applications, however complicates thermal stability. Higher current densities and larger thermal margins result in very local normal zones with high peak temperatures endangering the magnet's integrity. Adequate protection is therefore essential for safe operation especially in high energy density applications, such as multi-strand cables in accelerator dipoles. A quench should be detected sufficiently in advance, allowing time for the protection measures to take effect. Earlier studies showed traditional voltage detection not to be sufficient, causing permanent damage before the quench is identified. This report will explore the possibilities for quench detection for HTS magnets, by studying the underlying quench phenomenon in multi-strand Roebel cables using calculations and experiments to discover new possibilities for robust detection methods.

Within this thesis, the multi-physics phenomena preliminary to a quench are analysed using a numerical model and various analytic models. To describe the quench behaviour, the stability of the superconductor is analysed as function of the operating current and cable and magnet properties. Although this analysis focuses on Roebel cable, the locality of HTS quench reduces the influence of the exact cable geometry at hand. As is shown, a quench is predominantly dependent on the local thermal behaviour at the quench location and the macroscopic magnetic and electric properties of the magnet and cable, such as self-induction and inter-strand resistance. LTS quench methods are therefore fairly cumbersome for making HTS quench calculations.

Due to its locality, the quench is difficult to detect especially at high current densities. Detection by measuring directly the quench itself, e.g. temperature and/or voltage, cannot cover its entire operating domain. However the effects of a quench, in particular the current redistribution, will be proven to have measurable effects on a much larger scale. Based on the model, a novel quench detection design to identify a quench in a preliminary stage is presented.

To demonstrate the quench detection method, a prototype is implemented in Feather-M0.4, a HTS racetrack coil with the goal to explore quench behaviour. A compactRIO was used for sensor data acquisition to verify the model and to validate the quench detection. The magnet tests encountered several practical problems for validating the quench detection design, including the ability to reach the higher current densities and artificially quenching the magnet. Although the test only delivered preliminary results, the quench detection design is implemented in Feather M2 based on its promising potential.

CONTENTS

Symbol	Description	Unit
A	Area	[m^2]
$\mathbf{A}$	Redistribution induction matrix	[H]
$\mathbf{B}$	Redistribution resistance matrix	[Ω]
C	Thermal capacity	[$\mathrm{J\,kg^{-1}\,K^{-1}}$]
E_h	Energy of the heater pulse	[J]
h_q	Layer thickness	[m]
h	Tape thickness	[m]
i	Loop redistribution current	[A]
I_c	Critical current	[A]
I_e	Engineering current	[A]
I_{op}	Operating current	[A]
I_{nc}	Normal conductor current	[A]
I_{sc}	Superconductor current	[A]
J	Current density	[$\mathrm{A\,m^{-2}}$]
J_c	Critical current density	[$\mathrm{A\,m^{-2}}$]
J_e	Engineering current density	[$\mathrm{A\,m^{-2}}$]
J_{op}	Operating current density	[$\mathrm{A\,m^{-2}}$]
J_{nc}	Normal conductor current density	[$\mathrm{A\,m^{-2}}$]
J_{sc}	Superconductor current density	[$\mathrm{A\,m^{-2}}$]
k	Thermal conductivity	[$\mathrm{W\,m^{-1}\,K^{-1}}$]
L	Self induction	[H]
m	Number of elements electrical model	[-]
M	Mutual induction	[H]
$\mathbf{M}$ or M_{ij}	Induction matrix	[H]
MQE	Minimum Quench Energy	[J]
n	Number of strands	[-]
p	Number of elements thermal model	[-]
P_e	External disturbance	[W]
P_h	Heater disturbance	[W]
r	Interstrand contact resistance per meter length	[$\Omega\,\mathrm{m}$]
r_c	Interstrand contact resistance	[$\Omega\,\mathrm{m}^2$]
t	Time	[s]
T	Temperature	[K]
T_{cs}	Current sharing temperature	[K]
T_{hs}	Hotspot temperature	[K]
T_t	Transition temperature	[K]
T_c	Critical temperature	[K]
E_0	Voltage criteria for determining I_c	[V]
N	N-factor superconductor	[-]
V_{nz}	Normal zone propagation speed	[$\mathrm{m\,s^{-1}}$]
V	Voltage	[V]
V_{tot}	Voltage over the magnet	[V]
x	Spatial coordinate	[m]
α	Electrical diffusivity	[$\mathrm{m^2\,s^{-1}}$]
η	Scaling of the induction matrix	[-]
ρ	Specific resistance	[$\Omega\,\mathrm{m}$]
ρ_d	Specific density	[$\mathrm{kg\,m^{-3}}$]
λ	Filling factor	[-]
κ	Thermal diffusivity	[$\mathrm{m^2\,s^{-1}}$]
ℓ	Conductor length	[m]
ℓ_h	Thermal model length	[m]
$\mathscr{M}$	Interstrand inductance per meter length	[$\mathrm{H\,m^{-1}}$]
$\mathscr{R}$	Dimensionless disturbance	[-]

1

INTRODUCTION

High energy particle physics studies the fundamental particles which form the basic constituents of matter. These fundamental particles originate by collisions between protons (or electrons) at speeds approaching the speed of light. The observations from these collisions form the basis for the study of the creation of our universe and other fundamental physics problems, including dark matter and energy. These experiments are performed inside particle accelerators, which use both high magnetic and electric fields to attain high kinetic energies. These purpose-built machineries require the application of unconventional materials, including superconductors. Superconductors can carry high current with absolute no resistance, within a bounded operating regime. Since this superconducting state is limited by temperature, the appearance of resistance while carrying high currents can lead to rapid thermal runaways, which is called a quench. Quench stability is of main concern in the operation of superconductors, since it can threaten the magnet's integrity. Hence protection is required for safe operation. Apart from temperature, the superconducting state of a practical superconductor is bounded by other state variables which concern magnet applications, including magnetic field and the current in the superconductor, as will be discussed in Chapter 2.

Future development of accelerator magnets require the application of exotic superconducting materials, including High Temperature Superconductors (HTS), since conventional superconductors, Low Temperature Superconductors (LTS), run into their practical limits. Various superconductor materials exist which can potentially be used in future accelerators, although their application is not trivial. The thermal behaviour of LTS materials is well known, while the understanding of HTS quench behaviour remains limited.

In Section 1.1 particle accelerators in general, the LHC and its future prospects are discussed, which presents the framework of this thesis, the EUCARD-2 project. Within Work Package 10 'Future Magnets', HTS magnets Feather M0 and Feather M2 are being developed and they are briefly introduced in Section 1.2. General applications of superconductors are covered in Section 1.3, which leads to the thesis' problem formulation at the end of this chapter.

1.1. ACCELERATOR MAGNETS

Inside an accelerator charged particles are accelerated by an oscillating electric field. After reaching their target energy they are collided either with a stationary target or with a beam particle moving in the opposite direction. Linear accelerators are limited in maximum attainable collision energy by their dimension and electric field strength, whereas circular accelerators can reach much higher energy by repetitive acceleration. The charged particle is accelerated in a circular motion by the Lorentz force produced by the magnetic dipole field inside the accelerator. The total kinetic energy of a particle in a circular accelerator is bounded by the radius of the accelerator and the maximum attainable centrifugal (Lorentz) force, which is a function of the magnetic dipole field. Hence, the centre of mass collision energy E for a two way accelerator is defined by:

$$E = 0.3RB\,, \tag{1.1}$$

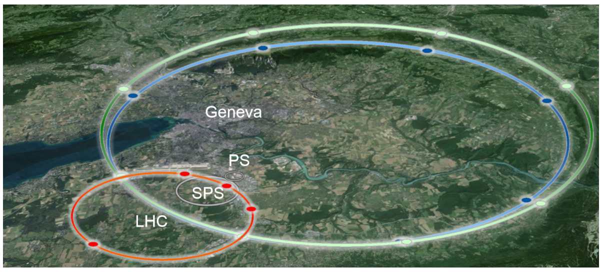

Figure 1.1: Future prospects of FCC design with LHC (red), FCC-hh of 100 km circumfence using Nb_3Sn (green) and FCC-hh of 80 km including HTS materials (blue) [3].

with energy E in GeV, dipole flux density B in T and accelerator radius R in km. Within the remainder of this report, magnetic flux density is referred to as magnetic field.

Apart from dipole magnets, an accelerator consists of magnets for correcting the field quality (Quadro-,Sexta and Octopoles etc.) and focussing the beam. The particles are collided inside several detectors, where the events are analysed to study fundamental particle physics. The particles are linearly accelerated in Radiofrequency Cavities which are located at constant intervals along its path, while the dipole magnets for the circular acceleration span the entire circumference of the accelerator.

The dipole magnets require high current densities J, the current carried per area of conductor, to allow high colission energies. Hence, resistive (Copper) magnets would require complex cooling systems and have low efficiency. Practical resistive magnets are limited to 2 T, although high fields exceptions exist [1]. Superconducting magnets are used instead, although needing cryogenic cooling, they do not require powering during persistent mode.

1.1.1. LHC

The Large Hadron Collider (LHC), with a circumference of 27 km, is the largest scientific instrument worldwide [2]. It is operational since 2009 with the discovery of the Higgs boson in 2012 as its main achievement. The magnetic dipole field is created by 1232 15 meter long dipole magnets with a flux density of 8.34 T, resulting in a maximum (centre of mass) collision energy of 14 TeV. The operation of the current LHC program is foreseen until 2024.

To accommodate higher collision rates in future operation of the LHC, the High Luminsoty LHC program was launched [3]. Since the superconductor $Nb-Ti$ currently used in the LHC is reaching its practical magnetic field limit, a new generation of superconducting magnets is being developed to reach quadrupole fields up to 13 T using the LTS material Nb_3Sn. [4]

1.1.2. FCC: FUTURE MAGNET DEMAND

Future plans are underway for the next generation accelerator: The Future Circular Collider (FCC). The FCC aims to reach a collision energy of 100 TeV, for which two designs are developed in parallel. Due to the demanding requirements, the conventional superconductor $Nb-Ti$ is not capable to meet the required magnetic flux density, hence high performance LTS and HTS materials Nb_3Sn and Yttrium Barium Copper Oxide (YBCO) are considered, which allow higher operating fields. The tunnel layouts of both alternatives are shown in Figure 1.1.

Within the development for future accelerator design, these materials are considered in separate design studies. Since the LTS superconductor Nb_3Sn is limited to a practical dipole field of 16 T, it requires an accelerator circumference of 100 km. Although 16 T is estimated as the practical field limit of the conductor, whether a LTS dipole magnet can attain this flux density is currently being studied [5].

The HTS material YBCO is less restrained by the attainable magnetic fields (As will be shown in Section 2.3.1), potentially enhancing the accelerator performance. Hence, the application of HTS dipole magnets in the 16 to 20 T range is explored in Eucard-2 work package 10 'Future Magnets' [6][7][8]. The FCC alternative including HTS requires an accelerator circumference of 80 km when achieving a dipole field of 20 T.

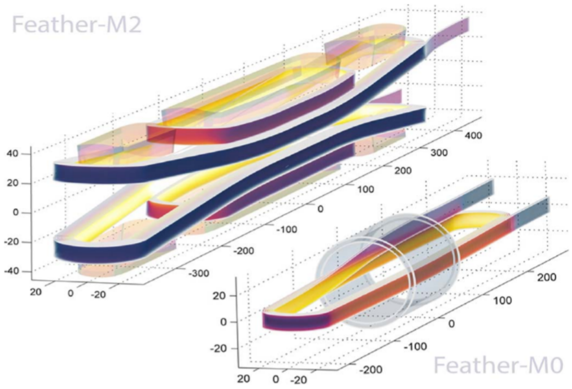

Figure 1.2: Coil winding geometry of the two HTS magnets within the EUCARD-2 project: Feather M0 (right) and Feather M2 (left) [6]. Feather M0 is a simple racetrack coil with a lower lead (+,right) and a upper lead (-,left). Feather M2 is a model dipole magnet with an aligned block geometry consisting of two decks.

1.2. SUPERCONDUCTING MAGNETS

Within the EUCARD-2 project two magnet types are currently being developed. The winding geometry of Feather M0 and Feather M2 are displayed in Figure 1.2. Both coils use YBCO cables as superconductor.

Since HTS is a novelty at CERN, Feather M0 is the initial development step to HTS accelerator magnets. This racetrack coil aims to validate the production method and is used for studying thermal quench behaviour. After several winding and impregnation studies, Feather M0.4 was the first full operational HTS magnet at CERN. The preliminary test results of Feather M0.4 are presented in Chapter 5.

Feather M2 will be the first accelerator quality dipole demonstrator magnet, aiming to achieve a dipole field of 5 T with a clear aparature of 40 mm and an outer diameter of 99 mm. Since YBCO is anisotropic (See Chapter 2), a novel alligned block geometry was introduced to optimise its performance [9].

The outer diameters of both magnets allow the magnet to operate as an insert inside the LTS magnet Fresca-2. While operating as an insert inside a 13 T background field of the LTS magnet, Feather M2 aims to produce a 17 to 20 T accelerator quality dipole field. The standalone and insert design of Feather M2 differ in mechanical structure, since high planar stresses arise when operating in a high background field [10]. The conductor of the standalone Feather M2.1 is currently being wound and is foreseen to be tested by the end of 2016 [7].

1.3. APPLICATIONS

Practical application of superconductors is found in magnetic devices where high fields and/or space restrictions exist. The absence of resistance enables the superconductor to carry much higher current densities compared to conventional conductors like copper, allowing for compact magnet design and the ability to produce high magnetic fields. However, commercial application of superconductors is limited by the material costs and the cryogenics to maintain superconductivity.

As will be discussed in Chapter 2, a practical superconductor is limited in cross-sectional area due to the presence of screening currents in the superconductor caused by electromagnetic fields. Since high power superconductor applications require generally high operating currents, a superconducting cable containing multiple individual superconductors is required. Within this report, a cable consisting of multiple superconductors is referred to as multi-strand cable.

Magnet applications for LTS materials apart from accelerator magnets can be found in commercial medical equipment, such as NMR and MRI scanners, which require high magnetic field (0.5-4 T) [11]. These applications employ solenoids with high quality fields throughout their large apertures. Since conventional LTS superconductors only operate at temperatures around 4.2 K, liquid helium is required as coolant, while HTS superconductors could operate at temperatures above 77 K, which is the boiling point of liquid nitrogen. Nitrogen is in contrast to helium readily obtainable from the atmosphere and poses less demands for the

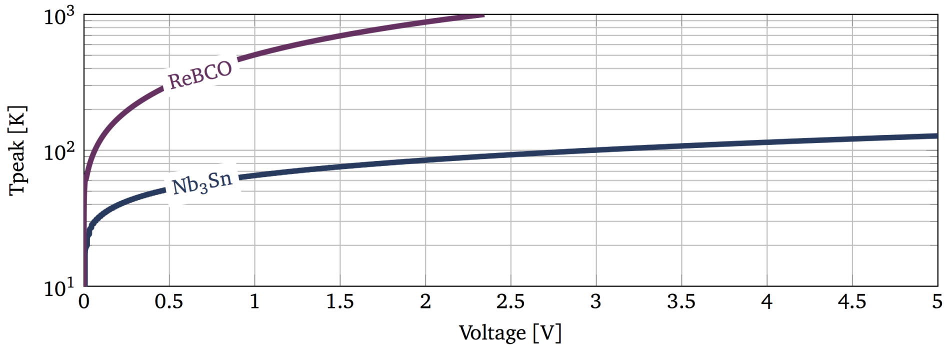

Figure 1.3: Quench hotspot temperature versus voltage over the superconductor for Nb_3Sn (LTS) and YBCO (HTS) [9]. By comparing the quench behaviour of both materials, the locality of a HTS quench causes protection issues, since its hotspot temperature is several times higher for the same voltage. Hence conventional voltage detection will prove not to be sufficient for protection of HTS applications.

cryogenics. Higher operating temperatures are not offering direct benefit for high field magnet applications, due to the reduced maximum attainable current density J. However, HTS materials operated at higher temperatures offer new possibilities for other applications, such as DC power lines. The less demanding cooling requirements enables it to operate in the generally inefficiently shaped cryostat of these power lines. Besides, HTS materials can be found as connection between the power supply at room temperature and a LTS magnet operating at temperatures around 4.2 K. The temperature gradient within the thermal insulation barriers of a cryostat allows for the superconductive operation of these HTS leads. The leads form a thermal barrier for ohmic heat originating at the resistive copper leads preventing it to perturb the delicate thermal stability of the LTS magnet. HTS leads are applied to power the magnets of the LHC [12] and in the current leads of the cryostat used for the test of Feather M0.4 discussed in Chapter 5. Other HTS lead applications are found for example in ITER reactor prototypes [13] and as part of the High Luminosity project, in which cold powering is assessed for the future LHC upgrade [14].

Apart from HTS power leads, potential future applications for HTS are found in situations where space is limited and high power densities are favourable [15]. High power rotary equipment with weight and or size limits offer potential, such as windmill generators, ship engines and high power generators. The application in these fields remain limited, since long lengths of HTS materials required for these applications are not readily available and remain expensive [16].

The high cost of HTS materials is governed by the limited number of high performance HTS material manufactures and its cumbersome manufacturing processes, discussed in Chapter 2. The costs of these materials are expected to decrease when future demand is growing, driving the research for more efficient production processes. Since the FCC would require large amounts of superconductor, the affiliated technological improvements could evolve into developments of other HTS applications [17].

Apart from the cost, the critical current density J is of concern for its potential future applications. The increase of its performance and the availability of longer superconductor lengths will offer the possibility for other future high field magnet applications, such as Superconducting Magnetic Energy Storage devices (SMES). The ongoing development of superconductors will help these high power applications mature [15].

1.4. QUENCH DETECTION

Due to the high currents and the limited operating domain where superconductivity is present, thermal stability issues arise in superconductor applications. The stability of superconductors is of great importance, since abnormal activity can lead to a local loss of superconductivity. The appearence of resistance in this 'normal zone' results in ohmic heating, which can initiate a thermal runaway with potentially destructive effects. The thermal behaviour in LTS materials has been studied extensively in the past [18][19][20], hence its quench causes and its failure modes are well understood. The detection of a resistive voltage together with fast protection measures allows for safe operation in widespread applications including NMR and MRI scanners.

Although HTS materials are already operational as current leads in several applications, HTS high energy accelerator magnets pose additional challenges, since the superconductor has to cope with high magnetic fields within complex geometries. In contrast to LTS, magnet applications of HTS materials remain in a premature stage of development. Especially controlling the thermal stability of HTS materials is a delicate matter. Since the quench behaviour of HTS materials is very local, the ohmic heating from the emerged resistance causes high hotspot temperatures [21]. Due to this locality, the resistive voltage signal remains small, complicating the detection of the quench, as shown in Figure 1.3. Hence conventional quench detection methods offer insufficient protection, as witnessed by [22]. Protection is of great concern for practical application of HTS materials, since quench poses the main threat for the integrity of HTS magnets, causing possible permanent damage from overheating within a fraction of a second.

This report aims to explore potential quench detection methods for HTS magnet applications. It specifically aims for the understanding of quench behaviour of a HTS multi-strand cable within a development model of an accelerator magnet. Insight in the behaviour is gained by analytic and numerical modelling combined with experimental results from testing Feather M0.4. Based on the understanding of the electro and thermo-dynamics behind the quench phenomenon, various alternatives are assessed.

A brief introduction in superconductivity is given in Chapter 2 to develop comprehension of the physics behind a quench. Chapter 3 combines various derivations of analytic equations and attempts to quantify its electric and thermal behaviour. Since quench is a thermal-electro magnetic phenomena, a numerical model is presented to gain insight in the multi-physics coupling. Based on the findings of Chapter 4, various existing quench detection systems are evaluated. Due to the large operating domain of HTS materials, a single quench detection system will prove not to suffice and a combination of systems is proposed. Chapter 5 presents the practical implementation of quench detection in Feather M0.4. Subsequently the test setup including the data acquisition, approach and preliminary results are presented and discussed. The report ends with a general conclusion followed by recommendations for future study.

2

SUPERCONDUCTOR

Superconductivity is a puzzling phenomenon for most engineers without a physics background. Although superconductivity is a complex quantum physics phenomenon which is still not fully understood, its macroscopic behaviour is simple: Under certain conditions a superconductor material has absolutely no resistance. Hence a superconductor can carry high currents without losses, potentially offering an outcome for many global energy problems. Nevertheless, the application of superconductors remains limited, due to the required thermal operating conditions to attain superconductivity. Over the years, research has found new materials, enabling higher performance and higher operating temperatures. This chapter starts with a general introduction to superconductivity followed by a brief description of practical superconductors and their characteristics. A specific type of superconductors, High Temperature Superconductors (HTS), has particular interest, since the operating regime for superconductivity is less restrictive and offers exceptional potential for very high magnetic field applications.

2.1. SUPERCONDUCTIVITY

A brief description of superconductivity is given below for readers who are not familiar with this phenomenon. Its underlying physics is summarized to get an idea of the macroscopic effects of the quantum behaviour. Although superconductivity is a quantum phenomenon, limited quantum physics is required for understanding the problem. Therefore the detail of this introduction is kept minimal, while interested readers are referred to [23].

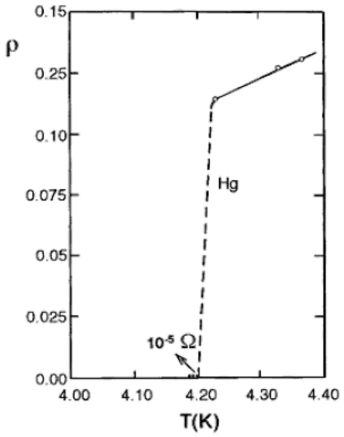

Figure 2.1: Illustration of the discovery of superconductivity in Mercury. The resistance of a superconducting material vanishes below the critical temperature T_c (T_c =4.2 K for Hg) [24].

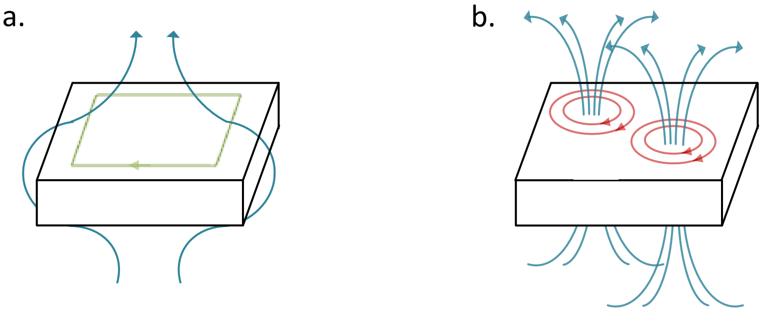

Figure 2.2: Illustration of the superconducting states: a. Meisner state, with full expulsion of the magnetic field (blue) by internal screening currents (green); b. Mixed state, restricting the flux entering the material in so called flux quanta (blue), which are encircled by current vortices (red).

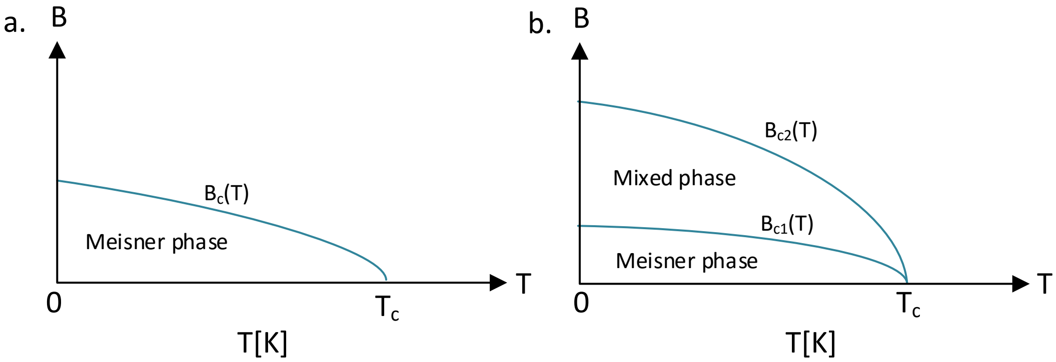

Figure 2.3: Schematic overview of the superconducting state(s) as function of the magnetic flux density B versus operating temperature T of the two superconductor types; a. Type 1 material , b. Type 2 material.

Superconductivity was first discovered in mercury by Kamerlingh-Onnes in 1911 and has been found in a variety of compounds and metals. The phenomenon was revealed by measuring a sudden drop in the electric resistance of the material when the temperature passes below a characteristic temperature, called the critical temperature T_c (Shown in Figure 2.1). Although some physicists claimed the electrical resistance should go to zero at 0 K, a sudden drop was not foreseen. The discovery revealed the existence of a state of the electrons at low temperature in which it is energetically favourable to form pairs, called Cooper pairs. The formation of these pairs allows for a tunnelling effect of the transport current which results in a complete loss of resistance, referred to as superconductivity.

From the classical study of superconductivity, a division is made into two main groups with distinctive properties: Type 1 and Type 2 superconductors. These superconductors and their characteristics are discussed below.

2.1.1. TYPE 1

Classical superconductivity, known as Type 1, emerges for approximately one third of (nearly) pure metallic materials, such as Pb, Al and Hg [23]. A Type 1 superconductor in its superconducting state features perfect diamagnetism for weak flux densities and the affiliated full expulsion of the magnetic field from its bulk material shown in Figure 2.2a. This phenomenon is called the Meissner effect and is bounded by the critical magnetic flux density B_c, as shown in Figure 2.3a. Type 1 superconductors are characterized by sharp transitions between normal and superconducting state when exceeding B_c. Since the critical flux density B_c of Type 1 superconductors lie below 2 T, their application in high fields is limited [25].

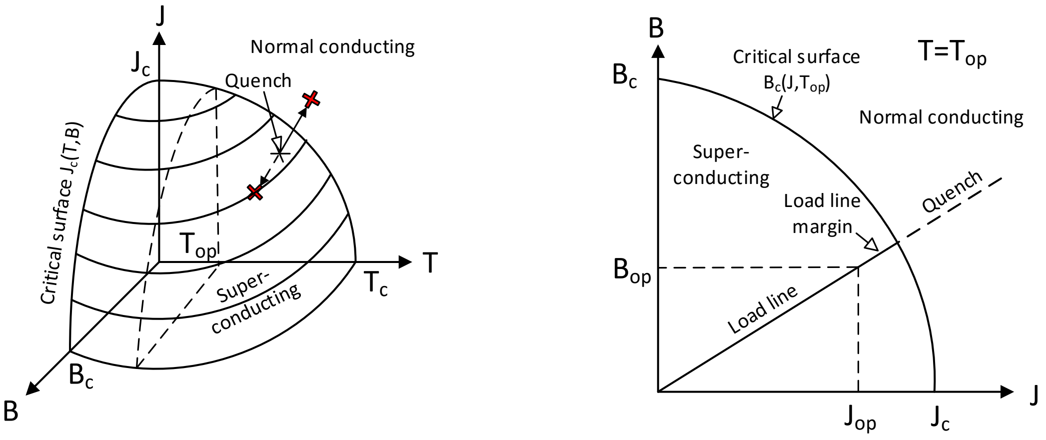

a. Illustration of the critical surface of a superconductor; **b.** Illustration of a magnet's loadline.

Figure 2.4: Schematic overview of the operation of a superconductor: a. Critical surface $J_c(T,B)$ of a superconducting material, the boundary between the normal and superconducting regimes. When the superconductor crosses locally the critical surface, the superconductor quenches; b. Load line of a magnet: The current and magnetic field of a magnet are dependent. At a constant operating temperature T_{op}, the operation regime of a magnet is reduced to a single dimension, the load line. The nominal operating state lies sufficiently within the limits of the critical surface to allow for operational stability.

2.1.2. TYPE 2

If Type 1 superconductor materials are doped, the transition between superconducting and normal state will become transient, which indicate Type 2 superconducting materials. Their pure superconducting state is limited by the first critical flux density B_{c1}, exceeding this limit results in a region where both normal and superconducting states persist simultaneously, called the mixed state, as shown in Figure 2.3b. Within this intermediate state the flux is allowed to penetrate the superconductor, called the Abrikosov effect shown in Figure 2.2b, which enables superconductivity up to higher magnetic fields.

The penetrating flux lines are encircled by screening currents, which are called vortices. The migration or creep of the flux should be restrained, since their movement causes power dissipation. Therefore the flux quanta are pinned by material impurities which make it energetically favourable for the flux to fix its position. The Lorentz force acting on these vortices increases with the current density J. If the Lorentz force exceeds the pinning force the flux starts to move, which results in electric resistance. Therefore, apart from T_c and B_{c2}, the transition boundary of the superconducting state is defined by critical current density J_c. Since high power superconductor applications require high current density, the ability to pin the flux is therefore of great importance. The critical current density J_c is defined as the current density J at which the specific resistivity exceeds $10^{-14}\,\Omega\,\mathrm{m}$, after which the superconductor has a steep ascend in resistivity [24].

The material dependent critical surface bounds the (resistive) normal and superconducting regime in the I, T and B parameter space, as shown in Figure 2.4a. An overview of the current density J versus the magnetic flux density B is shown in Figure 2.5 for various superconductors. For the ease of writing the flux density B is referred to as magnetic field, while the critical magnetic flux density B_{c2}, which is of interest for practical superconductors, is referred to as critical magnetic field B_c within the remainder of this report.

Within the normal operation of a magnet, current and magnetic field are coupled. Hence, assuming the operating temperature T_{op} is kept constant, the operating domain reduces to a single dimension, which is called the load line (shown in Figure 2.4b). The extent to which the current can be increased at nominal operation before the magnet enters its normal state is referred to as load line margin, which is a measure of the magnet's stability. The load line margin is either defined as a ratio between J_{op} and J_c or as $J_c - J_{op}$.

Apart from the Type 1 and Type 2 classification, superconductors are divided based on their critical temperature into Low Temperature Superconductors (LTS) and High Temperature Superconductors (HTS). LTS materials are bounded by a maximum critical temperature T_c of 30 K, while the critical temperatures of HTS materials have been reported up to 135 K at ambient pressure [26].

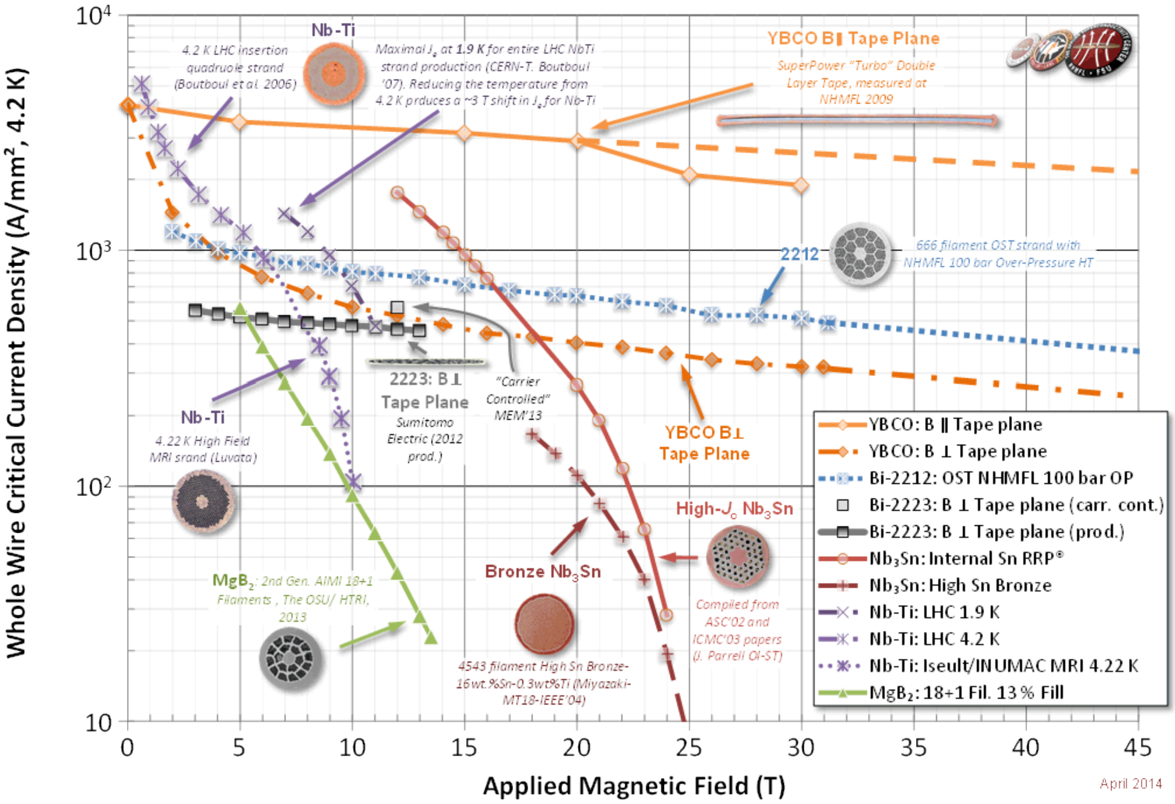

Figure 2.5: Critical current density J_c versus the applied magnetic field B for various LTS and HTS superconductors [NHMFL]. At a temperature of 4.2 K, the graph shows the conditions (Magnetic field B, current density J) below which various LTS and HTS materials are superconducting. YBCO (orange) shows the highest critical current density J for nearly the full applied magnetic field range.

2.2. LOW TEMPERATURE SUPERCONDUCTORS

LTS materials are currently the standard in superconductor applications and can be found in various high field applications, such as particle accelerators and medical instrumentation (as discussed in Section 1.3). The most common low temperature superconductors in present applications are the niobium alloys $Nb-Ti$ and Nb_3Sn:

$Nb-Ti$ is known as the workhorse of superconducting materials: Of all practical Type 2 superconducting materials, $Nb-Ti$ is the only non-brittle material, with a high tensile strength. These properties are favorable for the design and fabrication of high field magnets, which have to deal with high stresses. While the maximum critical field B_c of $Nb-Ti$ is 15 T, the practical limit of a $Nb-Ti$ magnet is roughly 10 T [27]. At higher flux densities B the critical current density J_c is becoming too low for a practical magnet.

Nb_3Sn offers twice as high critical field (up to 30 T), but at a significantly higher production cost. Since Nb_3Sn is a brittle material, the production of the magnet is complicating the design by its limited allowed bending stresses during winding. Winding of small bore magnets is done with an unreacted ductile wire containing niobium and tin, which during heat treatment reacts and turns into the brittle Nb_3Sn, known as 'Wind and React'. Various synthesation procedures exist, such as Restacked Rod Procedure (RRP), powder in tube (PIT), bronze route and internal tube (IT) procedures. However, thermal stresses can pose problems during the sintering process with temperatures up to 740 K [28]. The practical limit of Nb_3Sn is estimated to be 16 T for dipoles and 21 T for solenoids [29]. Due to the higher cost of Nb_3Sn material, designs exist combining low cost $Nb-Ti$ at low field regions with high performance Nb_3Sn at high field regions to limit production cost of the total magnet [30].

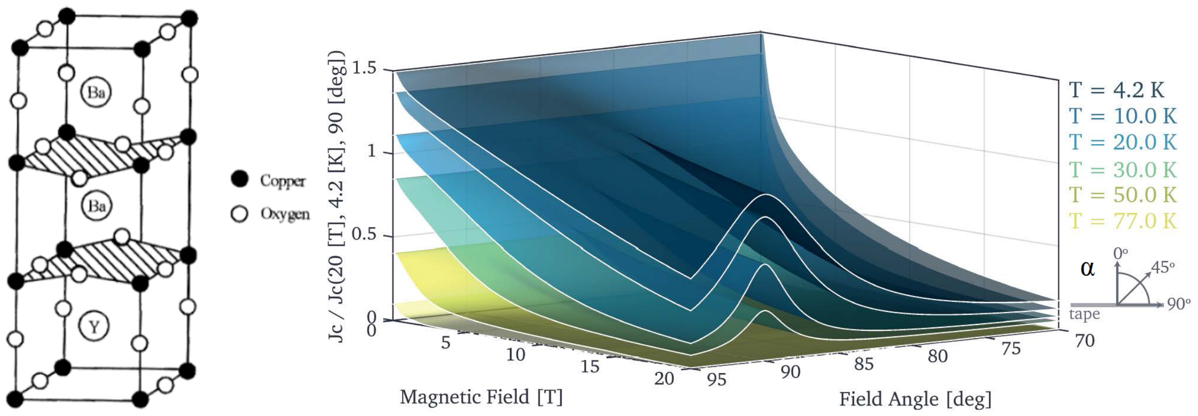

a. Crystalic structure of YBCO **b.** Critical field for YBCO tape [9] analogue to Figure 2.4a

Figure 2.6: Anisotropy of YBCO: a. Crystallic structure of the YBCO material containing copper oxide planes (indicated as marked surfaces); b. Normalized critical current density J_c of a tape as function of flux field B and field angle α for various operating temperatures. The copper oxide planes lie in the tape's plane, hence the field angle α defines the angle with respect to both the tape's and the copper oxide planes' normal vector. Note the high dependency of J_c near perpendicular field angle ($\alpha = 90°$) for higher flux densities B.

2.3. HIGH TEMPERATURE SUPERCONDUCTORS

Although superconductivity physics predicts a maximum attainable critical temperature T_c for any superconducting material of 30 K, several alloys were found to exceed this limit, referred to as High Temperature Superconductors (HTS). No fully satisfactory microscopic theory describing the superconductivity in these materials has been found to date.

The most common HTS materials are Rare Earth Barium Copperoxide (ReBCO) and Bismuth Copper Calcium Copperoxide (BiSCCO) materials. Apart from Yttrium (YBCO, Section 2.3.1), superconductivity in ReBCO materials has been found in other elements as neodymium, samarium, or gadolinium.

BiSCCO materials have a critical temperature T_c up to 123 K and are superconductive in magnetic fields up to 200 T [31]. Apart from the high temperatures during its sintering process (up to 900 K), the heat treatment requires a pressurized oxygen environment [32]. Hence, the production and design of high field magnet applications involving BiSSCO materials is complex.

2.3.1. YBCO

Yttrium Barium Copper Oxide (YBCO), with a critical temperature of 93 K, was discovered as the first superconductor material to remain superconductive above the boiling point of nitrogen (77 K). The material is highly anisotropic due to the copper oxide planes in its crystal structure, shown in Figure 2.6a. The angularity is described by α, the angle between the oxide plane's normal vector and the magnetic field direction. The maximum field for $\alpha = 0°$ is estimated at 120 T, while for $\alpha = 90°$ it ranges up to 250 T [33].

Practical YBCO superconductors are generally based on a tape geometry, as shown in Figure 2.7. The tape consists of several material layers, while the superconductor covers only a fraction of the tape's thickness. The superconductor material's oxide planes are aligned with the tape, ideally forming monocrystalline layers over the full length and width of the tape. The critical current density J_c of a YBCO tape as function of the magnetic field B, angle α and operating temperature T_{op} is shown in Figure 2.6b. The critical current density J_c is in contrast to the critical magnetic magnetic field B_c and critical temperature T_c not a material property. The type of impurity and the amount of doping influence the J_c and its angular dependency.

YBCO tape is produced by Pulse Laser Deposition (PLD) or wet chemical deposition, by depositing a the ceramic layer on a Hasteloy or stainless steal substrate, which acts as mechanical support. Buffering layers are used to ensure correct alignment of the YBCO crystalline structure. Using this deposition, mono crystalline lengths of several kilometres have been reached, which is required for accelerator magnet construction. Copper stabilizer is added on both sides of the tape for protecting the superconductor against a thermal runaway (See Chapter 3). Since a practical superconductors consists often of other materials apart from the super-

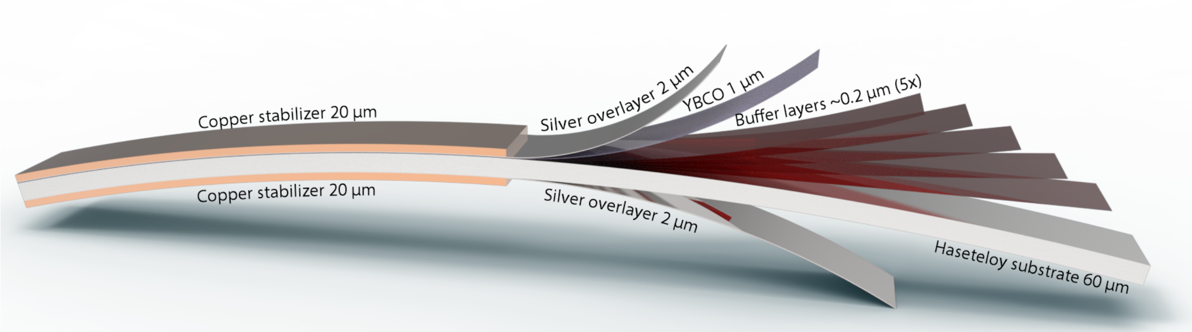

Figure 2.7: Illustration of the layers with thickness h_q composing a YBCO superconductor tape [9]: The superconducting layer (YBCO) represents only 1% of the total tape cross-section. The superconductor layer is deposited via several buffer layers on a Hasteloy substrate, which offers structural rigidity. The copper stabilizer at the outside of the cable offers thermal stability, as will be discussed in Chapter 4.

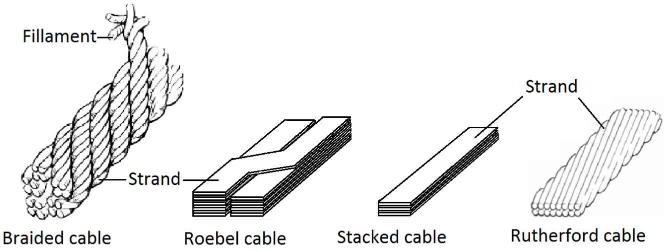

Figure 2.8: Several superconducting cable geometries: Braided, Roebel, stacked tape and Rutherford cable geometry [34].

conductor material itself, such as copper stabilizer, the engineering current density J_e is introduced, which defines the (average) current density over the whole cross-section of the conductor. Since this study only considers the application of a single superconductor material and tape geometry (as depicted in Figure 2.7) the engineering density J_e is referred to as current density J in general, unless stated otherwise.

2.4. CABLE GEOMETRY

As already mentioned in Chapter 1, the diameter of a practical superconductor strands or tape should be limited, due to occurrence of screening currents. Screening currents emerge due to magnetic field changes, similar to eddy currents in resistive materials. However, these screening currents do not fade, therefore locally increasing the current density J. These screening currents can cause the strand to reach the critical current density J_c locally while the overall current I is still below the critical current I_c. The screening currents are minimized by limiting the cross sectional area of the superconductor (typically <1 mm^2) [18].

The current per winding decreases as consequence from the reduced strand size. Hence the number of windings n need to increase to reach the targeted magnetic field B:

$$B \sim nI. \tag{2.1}$$

However, the induction scales with the number of turns squared, causing increased inductive voltages during current ramps, which bounds the ramp speed by the power supply voltage. Cables consisting of multiple superconductor strands are therefore used in accelerator magnets to meet the requirements during commissioning ramp up (100-1000 s for LHC [2]) and protection ramp down when the magnet quenches. [35]

A superconductor cable consists of individual strands woven together, as depicted in Figure 2.8. The interface between the different strands introduces contact resistance, preventing screening currents over the cross-section to occur. In some cases, such as high grade $Ni-Ti$ conductors, the strand itself consists of a bundle of filaments. In ReBCO conductors, the strands are formed by tapes (Figure 2.7).

The simplest cable geometry of ReBCO tapes consists of tapes stacked on top of each other (See Figure 2.8). The stacked tape geometry is due to its simplicity very useful for both analytical and numerical models presented in this report. Another geometry is the Roebel cable shown in Figure 2.9, recently used for YBCO cable

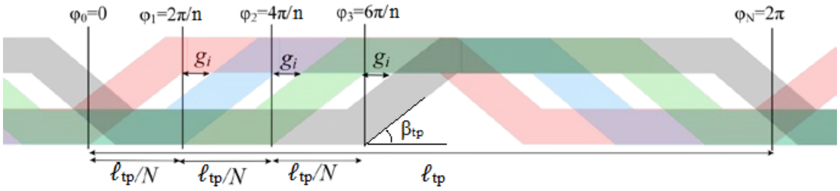

Figure 2.9: Geometry of 4 induvidual tapes forming a Roebel cable [36]. In this picture the phase shift ϕ, the twist pitch ℓ_{tp} and crossover angle β_{tp} of the Roebel geometry are shown.

to reduce AC-losses [8]. A Roebel cable consists of multiple meandering tapes braided together forming two linked stacks of tape. The skew sections at which the tape passes from one tape stack to another is called a cross-over. The length over which the braided pattern repeats itself is referred to as the twist pitch ℓ_{tp}, which is for YBCO Roebel cables of the order of 200 to 300 mm.

Multi-strand cables are used in nearly all high power applications, since the current carried by a single strand is limited by the small cross section of the individual superconductor. Hence this study focusses particularly on the thermal stability and quench detection of multi strand cables. In the next chapter the behaviour of multi-strand cables is studied using analytic and numerical modelling.

3

MODELLING

The design of an adequate quench detection scheme relies on the understanding of the complex multi-physics phenomena. Although LTS quenches have been studied extensively [18] [19], the understanding of quench in HTS remains limited. The goal of this chapter is to get a better understanding on the quench behaviour itself and the sensitivity of the quench to both external factors and the magnet's intrinsic properties. Both analytic and numerical methods were applied for the sake of gaining insight in different parts of the quench behaviour.

The study of LTS and HTS quench are related since the physics behind a quench is comparable for all superconductors, although they quantitatively diverge significantly due to the difference in operating domains and material properties. In the first section of this chapter the possible causes of LTS and HTS quenches are discussed, followed by a common analytic description of LTS and HTS strand or tape quench. The analytic description aims to get a better insight in the quench mechanism and to understand the quantitative difference between quench in LTS and HTS materials. After analysing quench in a single tape, the dynamics of a current redistribution effects in multi-strand are considered analytically.

The analytic models offer valuable understanding of these phenomena, but are limited in detail. Coupling effects between the electric and the thermal domain are complex and too demanding for analytical solving. Hence a multi-physics numerical model is introduced in the second half of this chapter to study the coupled thermal and electric behaviour of a HTS quench.

3.1. QUENCH CAUSES

Superconductors in their superconducting state can carry high currents without resistance. As has been mentioned in the Chapter 2, this state is limited by the critical surface, defined by critical temperature T_c, critical current I_c and critical magnetic field B_c. If this critical surface is exceeded, the superconductor quenches and enters its normal state, with high resistance causing intense ohmic heating as result [18][23].

The known LTS quench causes are shown in Figure 3.1, including the two most common causes: flux jumps and wire movements. As been discussed in the introduction, flux jumps occur when the Lorentz force acting on the flux quanta exceeds its pinning force. Flux jumps are therefore likely to occur at operating currents I_{op} near the critical current I_c, or as consequence of the screening currents (As discussed in Section 2.4). When the flux starts to move, it induces a voltage which causes dissipation. This local dissipation causes the superconductor to heat up, leading up to a possible thermal runaway.

Wire movement occurs when the Lorentz force cracks the coil impregnation or exceeds the friction forces acting on the conductor. Frictional heat is dissipated during the movement, which can cause the LTS magnet to quench. Wire movement is generally seen as an one time event, in which the conductor moves to a position with lower potential energy. Most magnets require therefore initial quenching to reach their target magnetic field, which is called training [18].

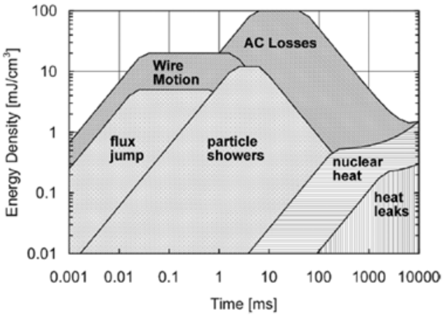

Figure 3.1: Disturbance energy density versus duration for various identified LTS quench causes in accelerator magnets. The energy density defines the locality (volume of conductor which is effected) of initial disturbance, while the duration defines the disturbance power. Wire motion and flux jump are the most common LTS material disturbances, while particle showers and AC losses are application related. Interested readers are reffered to [18].

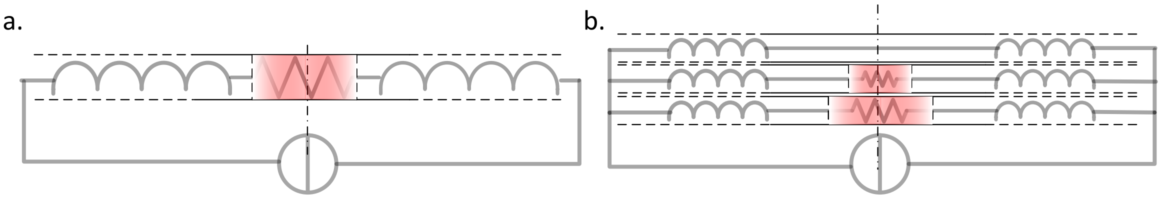

Figure 3.2: Schematic representation of the electrical and thermal behaviour of a normal zone in: a. a single tape with constant current. Assuming an ideal power supply, no inductive effects and operating current variations occur during a quench. In adiabatic conditions and insulated from the surrounding structure, the heat can only spread along the length of the conductor. The electrical behaviour and thus the ohmic heating is governed by a single normal zone described by the superconductor model; b. a multi-strand cable with constant current. During a quench the current can redistribute over the cable, causing a themo-electrodynamic coupling effect.

The LTS quench causes have not sufficient energy to quench a HTS magnet [21], since its practical operation margin makes it very stable compared to LTS. Its stability together with the higher current density also poses its pitfall, with possible disastrous effects. HTS Quench causes are therefore unknown, although their protection remains an issue, as will become clear later in this chapter.

Within this study a constant environment temperature of the superconductor and the magnet is assumed, which regards the cryogenic stability of the cryostat [18]. The cryostat is actively controlled by a separate protection system, which is out of the scope of this report. Hence only the influence of local disturbances with respect to the magnet behaviour is studied.

3.2. ANALYTICAL MODELLING

When analysing the behaviour of a single superconductor tape or strand with constant current (Figure 3.2a), the quench behaviour can be approximated as a linear one dimensional thermal problem. Analysis will start by understanding the thermal behaviour of a single tape, which offers valuable insight based on the analytic expression describing the quench development.

Although the thermal phenomena itself is described accurately in a single dimension, the quench mechanism in multi strand cables is more complex due to the ability of the current to redistribute over the neighbouring strands, as shown in Figure 3.2b. The electrodynamics during a HTS cable quench are studied by simplifying the thermal domain. Based on an analytical description the various current redistribution mechanisms during a quench in a HTS multi-strand cable are studied.

3.2.1. PARAMETER LIST

The thermal analytic model is based on a simplified representation of the behaviour, including constant material properties and operating conditions. The magnet and cable properties used in this analytical study are listed in Table 3.1 and Table 3.2 respectively. Within this study either values applicable to the analysis of Feather M0 and Feather M2, or a common standard in (HTS) quench analysis are chosen.

Parameter	Feather M0	Feather M2	Unit	Description
n	15		[-]	Number of tapes in the cable
ℓ_{tp}	224	300	[mm]	Twist pitch cable (Figure 2.9)
ζ_{tp}	30	30	[°]	Crossover angle (Figure 2.9)
L	40	480	[µH]	Magnet's self induction [9]
M/L	0.97	0.99	[-]	Mutual inductance of neighbouring strands [9]
ℓ	5	25	[m]	Length of the cable
N	4	21	[-]	Number of turns
r	$5.3 \cdot 10^{-5}$		[Ω m]	Electrical contact resistance [37] per meter strand length
k_c	100		[$\mathrm{W\,m^{-2}\,K}$]	Thermal conductivity between strands [38]

Table 3.1: Geometric properties of Feather M0 and M2 [6].

Material properties at 100 K used for the analytic approximations are displayed in Table 3.2. These material properties are derived from the more extensive material description of the numerical model [21].

	Temperature	Tape layers (Figure 2.7)			unit	Description
		Copper (RRR 20)	Hasteloy	Cable average		
t		40	60	100	[μm]	Thickness
w		5	5	5	[mm]	Width
ρ_d	100 K	8.94	7.9	8.5	[$\mathrm{g\,cm^{-3}}$]	Material density
k	100 K	433	9.4	174	[$\mathrm{W\,m^{-1}\,K^{-1}}$]	Thermal conductivity
C_t	100 K	250	219	239	[$\mathrm{J\,kg^{-1}\,K^{-1}}$]	Specific heat capacity
ρ	100 K	4.0	$1.24 \cdot 10^3$	10.0	[nΩ m]	Specific resistance

Table 3.2: Tape geometry and material constants. YBCO, silver and buffer layers are left out in the analytic calculations.

In this report Feather M0 and M2 will be used as case study in the simulation and modelling. The nominal operating conditions of Feather M0 and Feather M2 are shown in Table 3.3.

Property	Value	Unit	
T_{op}	4.5	[K]	Operating temperature
I_{op}	8	[kA]	Operating current
J_{op}	970	[$\mathrm{A\,mm^{-2}}$]	Operating current density
B	17	[T]	Magnetic field
α	4	[deg]	Magnetic field angle
T_{cs}	22.5	[K]	Current sharing temperature
T_c	59.8	[K]	Critical temperature
J_c at T_{op}	3734	[$\mathrm{A\,mm^{-2}}$]	Critical current density

Table 3.3: Design operating conditions of Feather M2.

3.2.2. HEAT BALANCE

A quench is basically a coupled thermal and electro-magnetic phenomenon, whereby this study starts by regarding the quench in the thermal domain. The local heat balance equation of an electrical conductor is given by:

$$C(T)\frac{\partial T}{\partial t} = \nabla \cdot (k(T)\nabla T) + \rho(T)J^2 + P_e - P_c. \tag{3.1}$$

with temperature T, the (volumetric) heat capacity $C(T)$, thermal conductivity $k(T)$, the local resistance ρ, current density J, external heat source P_e and cooling power P_c.

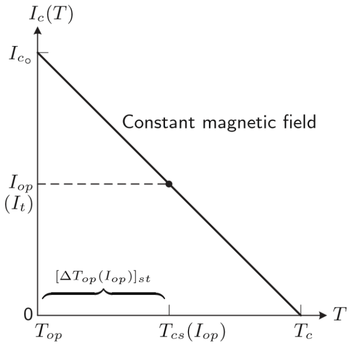

Figure 3.3: Schematic representation of current sharing temperature T_{cs}: Temperature at which the operating current I_{op} is equal to critical current $I_c(T_{cs})$ [20].

A superconductor has no resistance ($\rho = 0$) during nominal operation. When the temperature is constant over the whole magnet, the steady state T_{op} is found when the external source and the cooling power are balanced, i.e. $P_e = P_c$. If an unbalance $P_e > P_c$ occurs, the local temperature of the superconductor will rise. When locally the critical surface of the superconductor is reached (Figure 2.4a), part of the current is shared between the resistive matrix and the superconductor, which is denoted as the current sharing temperature T_{cs}. Since part of the current flows through the resistive material, it experiences resistance $\rho > 0$ which causes ohmic heating to occur.

SUPERCONDUCTOR REGIMES

The current sharing temperature T_{cs} is defined as the temperature where $I_{op} = I_c(T_{cs})$ as shown in Figure 3.3. The state of a HTS superconductor can therefore be divided into 3 temperature regimes (As summarized in Table 3.4):

- Superconductivity regime, bounded by current sharing temperature T_{cs}, where all current flows through the superconductor. The current endures no resistance and therefore no ohmic heating occurs;
- Current sharing regime, ranges from current sharing temperature T_{cs} to critical temperature T_c, where the current has exceeded I_c in the superconductor. The current is divided over the superconductor and stabiliser, whereby ohmic heating occurs within the stabiliser and at the contact interface between stabiliser and superconductor;
- Normal conductor regime, for temperatures exceeding T_c, where virtually all current flows through the stabiliser, since the resistivity of a superconductor increases rapidly after exceeding T_c.

Apart from temperature, the transition between these regimes are defined by the magnetic field B_c and field angle α, as was shown in Figure 2.6b.

When the superconductor reaches T_c the superconductivity vanishes, causing a quench. To get an idea of the possible thermal runaway, the temperature increase can be roughly estimated from Equation 3.1 based on the operating conditions of Table 3.3 and by neglecting the conductivity, external heat source and cooling term:

$$\frac{\partial T}{\partial t} = \frac{\rho J^2}{C} \approx 5 \cdot 10^3 \mathrm{K s}^{-1}. \tag{3.2}$$

This value was found by assuming an average conductor temperature of 100 K, with the material properties found in Table 3.2. Although this is a simplified representation, it shows the potential thermal runaway during a quench. As a consequence, both hotspot temperature and thermal gradients can pose a hazard to the magnet [39]. Note the quadratic current proportionality of the ohmic heating, which increases the instability of the thermal runaway at higher current densities. Protection of the magnet is therefore required to prevent it from overheating.

	Temperature	Superconductor	Matrix
Superconducting	$T < T_{cs}$	I_{op}	0
Current sharing	$T_{cs} \leq T < T_c$	I_c	$I_{op} - I_c$
Normal conducting	$T > T_c$	~ 0	I_{op}

Table 3.4: Subdivision of superconductor regimes.

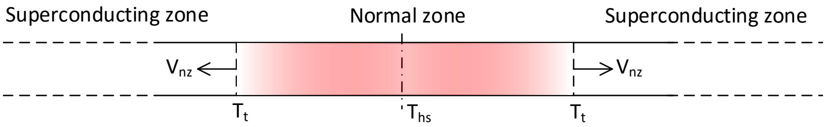

Figure 3.4: One dimensional propagation of the normal zone through a tape, showing the normal zone propagation speed V_{nz}, hotspot temperature T_{hs} and transition temperature T_t.

NORMAL ZONE PROPAGATION SINGLE TAPE

The quenched region or normal zone propagates through the superconductor after a quench. Its propagation in the conductor's longitudinal direction V_{nz} can be described by considering an one dimensional analytical model, as shown in Figure 3.4. Analytic one dimensional models have been studied extensively in the past for LTS applications [18][19]. The quench model is divided in a superconducting and normal conducting region, separated by the transition temperature T_t. An abrupt transition at temperature T_t is assumed for simplification, of which many definitions exist in literature, including:

1. $T_t = T_{cs}$ [40];
2. $T_t = T_c$ [41];
3. $T_t = \frac{T_{cs}+T_c}{2}$ [42].

Since HTS materials are known for their relatively large transient regions, the choice of T_t is affecting directly the analytic results. Although it is difficult to fit the transition T_t on emperical data, the Dresner [42] (3.) approximation was chosen in this derivation. The adiabatic one dimensional heat balance for normal zone and the superconductor region are derived from Equation 3.1 and are respectively given by [20]:

$$C_n(T_n)\frac{\partial T_n}{\partial t} = \frac{\partial}{\partial x}\left[k_n(T_n)\frac{\partial T_n}{\partial x}\right] + \rho_n(T_n)J^2;$$
$$C_s(T_s)\frac{\partial T_s}{\partial t} = \frac{\partial}{\partial x}\left[k_s(T_s)\frac{\partial T_s}{\partial x}\right],$$

with the temperature T, volumetric heat capacity C and thermal conductivity k averaged over the normal zone and superconducting region denoted respectively by subscript n and s. Assuming propagation velocity V_{nz} to be constant, a coordinate system moving with the transition boundary is defined: $z = x - V_{nz}t$. After applying $T(z=0) = T_t$ and $T(z=\infty) = T_{op}$, it follows [43]:

$$T_s(z) = (T_t - T_{op})\exp\left(-\frac{C_s V_{nz}}{k_s}z\right) + T_{op}, \tag{3.3}$$

with operating temperature T_{op}. By applying continuity at the transition boundary of both regions, a direct expression for the propagation V_{nz} is found [20][44]:

$$V_{nz} = J_{op}\sqrt{\frac{k(T_s)\rho(T_t)}{C_n(T_t)\int_{T_{op}}^{T_t} C_s(T)dT}}. \tag{3.4}$$

The difficulty in applying these equations in HTS applications is the choice of transition temperature T_t, due to the high temperature gradient of the transition zone. In [44], by using the Dresner approximation, the normal zone propagation speed in YBCO tapes is found to be nearly indifferent to T_{op} and magnetic field **B**, which is agreement with experimental results [21]. The propagation of the normal zone is therefore geometry dependent and follows a power law with current.

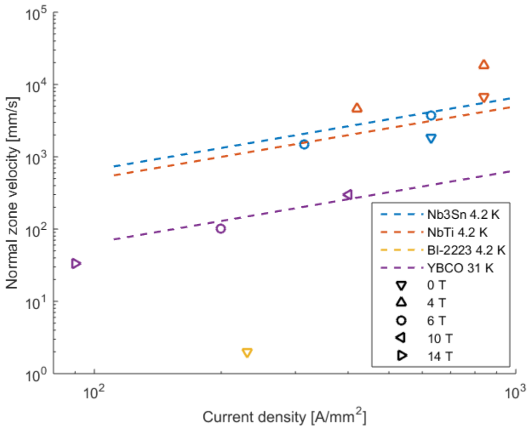

Figure 3.5: Empirically found normal zone propagation (markers) versus current density for various superconductor materials compared to the approximation of Equation 3.5 (dotted line) [20][21]. The empirical data is measured at various temperatures and magnetic fields, which complicates quantitative comparison. Nevertheless, it is observed that HTS normal zone propagates at least an order of magnitude slower compared to LTS materials.

For LTS applications $(T_t - T_{op})/T_{op} \ll 1$ holds, therefore the temperature dependency of the thermal properties can be simplified by introducing $\bar{T} = (T_t + T_{op})/2$ [20]:

$$V_{nz} = \frac{J}{C_m(\bar{T})}\sqrt{\frac{\rho_m(\bar{T})k_m(\bar{T})}{\bar{T}}}\,. \tag{3.5}$$

The approximation of Equation 3.5 and various experimentally found normal zone propagation velocities are shown in Figure 3.5. Quantitative comparison between studies is challenging, due to the large variety of applied materials, cable geometries and test conditions. Nonetheless, the observed normal zone propagation velocity V_{nz} of LTS is at least an order of magnitude higher compared to HTS materials. The large temperature operating margin and the materials' higher heat capacities at higher temperatures causes slow normal zone propagation in HTS, which exposes the superconductor to locally high hotspot temperatures T_{hs} while it poses difficulties for detection (Figure 1.3).

In the analytic description above, only one strand/tape with constant current was considered. The solution was limited to the propagation of the normal zone in the principal direction along the conductor. Although it gives insight in the quench phenomenon, its practical use is rather limited. The next section will have a closer look on the current distribution behaviour within a cable in more detail.

3.2.3. CURRENT REDISTRIBUTION DYNAMICS

The currentdynamics inside a superconducting cable have been studied in the past to analyse the stability of LTS cables [45] [46] [47]. In order to study the behaviour in HTS multi strand cables, several analytic models are considered to gain insight in the current redistribution behaviour during a quench. The analytic study starts by considering an ideal magnet shown in Figure 3.6. The voltage over the magnet is given by:

$$V = L\frac{dI_{op}}{dt} + RI_{op}\,, \tag{3.6}$$

with self induction of the magnet L, resistance R and operating current I_{op}. If the magnet is superconducting no resistance is present and the voltage is governed by induction. The inductive voltage is proportional to the amplitude of the ramp rate, which is one of the reasons to use multistrand cables, as discussed in Section 2.4.

Within a multi-strand cable, the current is divided over its individual strands, as shown in Figure 3.7a. In nominal operation, the transport current I_{op} is evenly spread over the number of strands:

$$I_i(x, t = 0) = \frac{I_{op}}{n} \quad \text{for: } i = 1..n\,, \tag{3.7}$$

where n represents the number of strands and I_i the current in each strand.

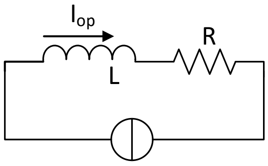

Figure 3.6: Simplified magnet representation.

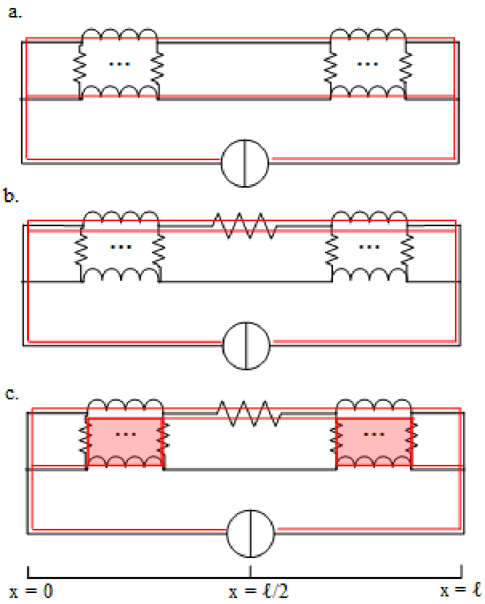

Figure 3.7: Schematic representation of the current redistribution mechanisms; a. nominal operation; b. redistribution over the joint ΔI_j; c. redistribution throughout the length of the cable $\partial I_c(x)$.

In case of abnormal behaviour a difference in voltage potential between the strands can emerge, which causes the current to redistribute from one strand to another, as shown in Figure 3.7. This spontaneous potential difference can be caused by an unbalance of:

1. Resistance, e.g. normal zone;
2. Induction, e.g. external magnetic field changes (not considered in this study).

An unbalance in resistance can arise by a local normal zone. When the external disturbance P_e of Equation 3.1 affects the cable, an inhomogeneous temperature can arise. If the temperature locally exceeds T_{cs}, a normal zone emerges in certain strands, as shown in Figure 3.2b. The unbalance of normal zone resistances will cause a potential difference between the strands, resulting in the current to redistribute.

Understanding the current dynamics is important, since ohmic heating is the main cause of the thermal runaway. Both paths of current redistribution are shown in Figure 3.7:

1. passing the joint ΔI_j: Low joint resistance, high induction path;
2. within the cable $\delta I_c(x)$: Local phenomena with high(er) contact resistance, low induction path.

Although both mechanisms actively participate to the current redistribution during a quench, these mechanisms will be analysed separately in the remainder of this section. To study the currentdynamics, an ideal current source is assumed, hence:

$$\sum_{i=1}^{n} \frac{dI_i}{dt} = 0. \tag{3.8}$$

Since voltages remain generally low during a quench this assumption can be justified.

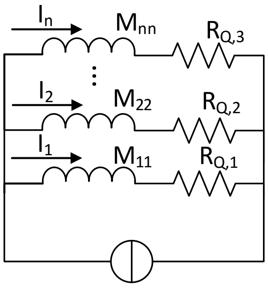

Figure 3.8: Schematic overview of a n-strand cable with insulated strands.

ELECTRICALLY INSULATED STRANDS

The simplest case of current redistribution consists of a cable with individually insulated strands connected in parallel to a current source as shown in Figure 3.8. The current can only distribute over the joints, causing a current redistribution over the whole length of the cable. Assuming a cable with n strands, the system is described by the following equation:

$$\sum_{j=1}^{n} M_{ij}\frac{dI_j}{dt} + R_{Q,i}I_i = V_{tot} \quad \text{with} \quad i = 1..n, \tag{3.9}$$

where indices i and j represent the individual strands, the current I_i, mutual induction M_{ij}, the normal zone resistance in the strand $R_{Q,i}$ and the total voltage over the magnet V_{tot}. All strands are placed in parallel, hence V_{tot} is identical for each strand. The induction matrix $\mathbf{M}$ is symmetric since $M_{ij} = M_{ji}$, while the inductance M_{ii} is known as the self inductance of the individual strand. To simplify the analytic equation the inductance matrix $\mathbf{M}$ is defined as:

$$M_{ij} = \begin{cases} L & \text{for } i = j \\ M & \text{for } i \neq j \end{cases}. \tag{3.10}$$

By simplifying Equation 3.9, the first order differential equation describing the current dynamics is given by:

$$V_{tot} = (L - M)\frac{dI_i}{dt} + R_{Q,i}I_i, \tag{3.11}$$

which consists of an inductive and a resistive part. A characteristic time τ_j is found, which characterises the transient behaviour caused by a constant resistance R_Q in a single strand (analogous to [46]):

$$\tau_j = \frac{n}{n-1}\frac{L-M}{R_Q}. \tag{3.12}$$

To model a quench, a sloped resistance is applied to Strand 1, while the other strands remain superconductive:

$$R_{Q,i} = \begin{cases} r_Q t & \text{for } i = 1 \wedge t > 0; \\ 0 & \text{else.} \end{cases}. \tag{3.13}$$

By assuming nominal operation at $t = 0$, given by Equation 3.7 and Equation 3.8, the following redistribution is obtained:

$$I_1 = \frac{I}{n}\exp\left(-\frac{t^2}{\lambda^2}\right), \tag{3.14}$$

$$I_i = \frac{I}{n}\left[1 + \frac{1}{n-1}(1 - \exp\left(-\frac{t^2}{\lambda^2}\right)\right] \quad \text{for} \quad i = 2..n, \tag{3.15}$$

with redistribution time constant for a sloped resistance λ:

$$\lambda = \sqrt{\frac{2n(L-M)}{(n-1)r_Q}}. \tag{3.16}$$

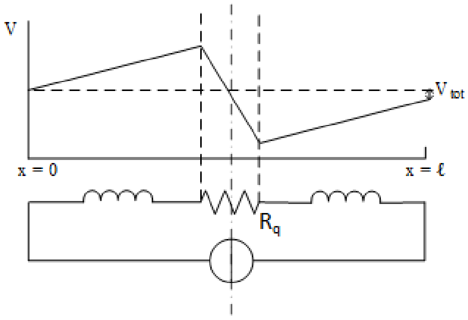

Figure 3.9: Schematic representation of the inductive compensation of a quench resistance in the magnet. Current redistributions will cause an inductive voltage opposing the resistive quench voltage, resulting in a significantly smaller voltage signal over the whole magnet.

The characteristic time constants λ and τ_j are a measure for the decay of the current in the quenched strand. The current will redistribute slower when the cable consists of less strands and/or if the normal zone resistance is lower. Since a higher time constant results in a slower current redistribution, the current will continue flowing through the normal zone of the quenched strand. Assuming a constant R_Q and r_Q, the higher current in the quenched strand causes increased ohmic heating over time. Following Equation 3.1, the temperature of the superconductor will rise, which stimulates the grow of the normal zone. Hence, a higher characteristic time constant lowers the overall stability of the cable. The time constants λ and τ_j for Feather M0 and Feather M2 are displayed in Table 3.5.

The voltage measured over the conductor length V_{tot} can be found by substituting Equation 3.15 into Equation 3.11:

$$V_{tot} = \frac{Ir_Q}{n^2} te^{-t^2/\lambda^2}. \tag{3.17}$$

Equation 3.17 shows clearly an important dilemma of applying voltage quench detection to multi strand cables: The voltage over the magnet during the current redistribution after a single strand quench scales inverse proportional to the square of the number of tapes. The ratio between the voltage over the magnet and the resistive voltage over the normal zone is given by:

$$\frac{V_{tot}}{V_r} = \frac{1}{n}. \tag{3.18}$$

The resistive voltage over the magnet is compensated by the inductive voltage caused by the redistribution to the remaining strands, as shown in Figure 3.9. The inductive voltage cannot be distinguished from resistive voltage by measuring the voltage over the whole magnet alone [18]. These inductive compensation voltages are studied in more detail in Chapter 4. From this analytic result the following can be observed:

- The induction experienced by redistribution is lower than the magnet's self-induction due to mutual induction of the strands, enhancing the ability for the current to redistribute.
- Characteristic time constant τ_j defines the current decay of the current after a single strand quench with constant resistance R_Q.
- The inductive voltage compensates the resistive voltage, therefore only $1/n$th of the resistive voltage over the quenched strand is measured;

Due to the mutual coupling between the strands, the induction experienced by current redistribution is $L-M$. Mutual induction M for long slender cables ($\ell \gg w$) approaches the self induction L, therefore the inductive load experienced by the redistribution is only a fraction of the self induction of the magnet L. For Feather M0 and Feather M2 L/M ratios of 97 % and 99% were found (Section 3.2.1) [9].

Based on the observations of this simplified analysis the cable's stability and the challenges of voltage quench detection is demonstrated. In the next section the current redistribution inside the cable is analysed in greater detail.

	Stepped resistance - 1 mΩ		Sloped resistance - $0.1\,\mu\Omega\,s^{-1}$	
Magnet	τ	V_{max}	λ	V_{max}
Feather M0	1.3 ms	35.6 mV	5.1 ms	7.7 mV
Feather M2	5.1 ms	35.6 mV	10.1 ms	10.1 mV

Table 3.5: Current redistribution characteristics of FM0 and FM2 assuming insulated strands for both ramped and stepped resistance. The resistance values were observed in the numerical simulations of Section 3.3.

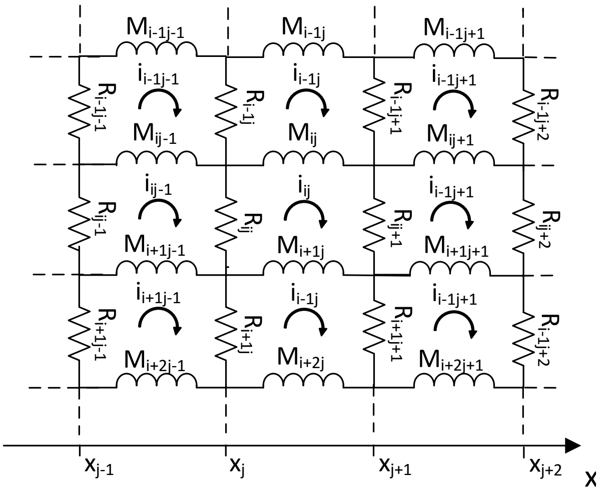

Figure 3.10: Schematic representation of current redistribution within a multi-strand cable. The redistribution loop current i_{ij} describes the local current redistributed from Strand $i-1$ to i in current element j.

ELECTRICALLY NON-INSULATED STRANDS

In most applications the strands in a cable are not insulated from each other, making it possible for the current to redistribute along the length of the cable [48]. Since the current redistribution in the cable can occur over part of the cable's length (Figure 3.7c), it experiences less inductive effects, allowing the redistribution to occur faster. However, the strand contact interfaces in the cable introduce interstrand resistances [38]. Hence, this mechanism is likely to be present in transients of non-insulated superconductor multi-strand cables experiencing high inductive loads, such as quench behaviour in magnet applications [47].

The electrodynamics of a quench are studied by deriving an analytic description of a non-insulated multi-strand cable. A cable consisting of n strands is discretized into m elements as depicted in Figure 3.10. By introducing the loop current i_{ij} and applying Kirchoff's current law to Element j of Strand i, the following equation is obtained:

$$\sum_{k=1}^{n-1}\sum_{l=1}^{m}\left[(M_{ij,kl}-M_{ij,k+1l}-M_{i+1j,kl}+M_{i+1j,k+1l})\frac{di_{kl}}{dt}\right]+(R_{ij}+R_{ij+1})i_{ij}-R_{ij}I_{ij+1}-R_{ij+1}i_{ij-1}=0, \tag{3.19}$$

with redistribution current i_{ij} and interstrand resistance R_{ij} and mutual induction between elements M_{ij}. To limit the number of equations two infinitly long strands are considered as shown in Figure 3.11, although this expression can be extended for multiple strands [46]. The current redistribution inside a 2 strand cable with constant transport current (Equation 3.8) is governed by:

$$\sum_{l=1}^{m}\left[(M_{1j,1l}-M_{1j,2l}-M_{2j,1l}+M_{2j,2l})\frac{di_{l}}{dt}\right]+(R_{ij}+R_{ij+1})i_{j}-R_{ij}i_{j+1}-R_{ij+1}i_{1j-1}=0. \tag{3.20}$$

Since the material's bulk behaviour is considered, the gradient of current redistribution is assumed to remain small:

$$\frac{di^2}{dxdt}\approx 0, \tag{3.21}$$

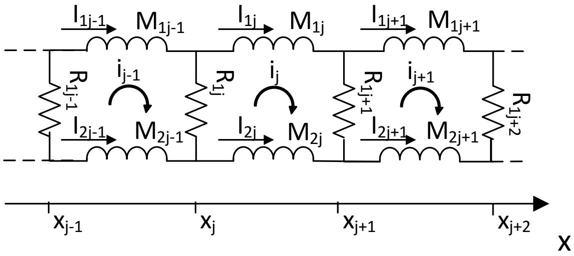

Figure 3.11: Schematic representation of current redistribution within a 2 strand cable derived from Figure 3.10.

or:

$$\frac{di_j}{dt} \approx \frac{di_l}{dt} \quad \text{if} \quad j \sim l. \tag{3.22}$$

The cable is assumed to be long and slender, therefore the mutual induction between elements spaced far apart, i.e. $x_j - x_k \gg dx$, is neglected. The mutual induction coupling is simplified to:

$$(M_{ij,kl} - M_{ij,k+1l} - M_{i+1j,kl} + M_{i+1j,k+1l})\frac{di_l}{dt} \approx \begin{cases} 2(L-M)\frac{di_j}{dt} & \text{if: } j \sim l \\ 0 & \text{else} \end{cases}, \tag{3.23}$$

with L and M as self and mutual induction of the whole magnet. The contact resistance R_{ij} is assumed constant along the conductor and is defined as:

$$R_{ij} = \frac{r}{\mathrm{d}x}, \tag{3.24}$$

with element size dx and interstrand contact resistance r. From Equation 3.24, Equation 3.20 and the assumptions of Equation 3.21 and Equation 3.23, the continuous differential equation can be derived:

$$2\mathscr{M}\frac{di}{dt} - r\frac{d^2 i}{dx^2} = 0, \tag{3.25}$$

where r is the resistance per unit length between the two wires and $\mathscr{M}$ the induction experienced by cable redistributions. The induction term $\mathscr{M}$ features:

$$\mathscr{M} = l - m,$$

with l and m as the self and mutual induction between the two strands per unit length. This partial differential equation is valid for n-strand cable problem. Although this formulation was derived independently, another derivation exists without assumption of Equation 3.21. It was found by directly neglecting the inductive coupling $M_{ij,kl}$ between elements $j \neq l$ [48].

A set of solutions can be found by separation of variables $i(x,t) = X(x)T(t)$ and defining the cable's 'current diffusivity' or 'magnetic diffusivity' α [47], which describes the ratio between local contact resistance and induction:

$$\alpha = \frac{r}{2\mathscr{M}}. \tag{3.26}$$

Since cable compositions such as the stacked tape and Roebel geometry have two fixed neighbours throughout the cable, the current redistribution in a 3 strand cable is studied. Figure 3.12 shows the equivalence between an asymmetric quench in a 2-strand cable with a symmetric and asymmetric quench in a 2 and 3 strand cable. These cases show 2 types of symmetry:

1. Longitudinal symmetry, reducing the model from 3 to 2 strands;
2. Mid-plane symmetry for symmetric quench.

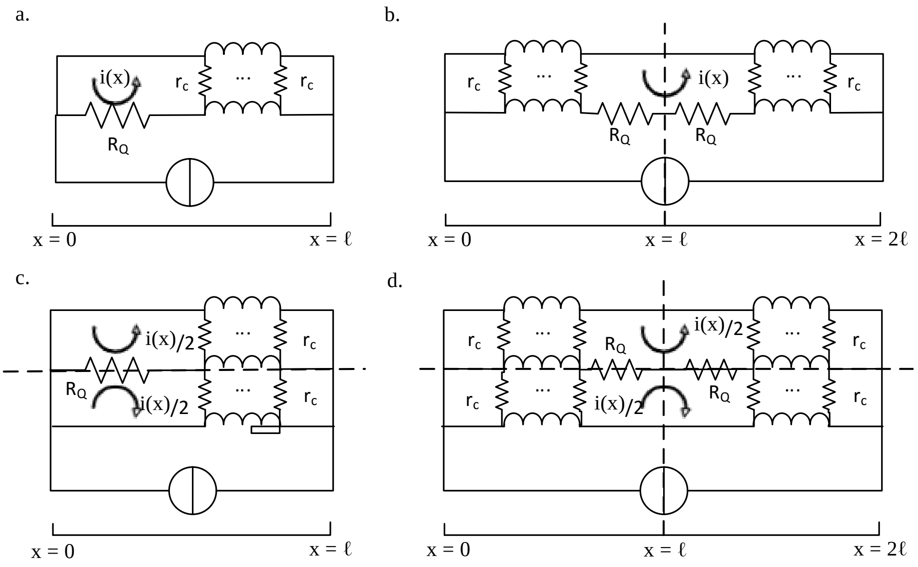

Figure 3.12: Equivalent redistribution models by symmetry, a. asymmetric quench in 2 strand model, b. symmetric quench in 2 strand model, c. asymmetric quench in 3 strand model and d. symmetric quench in 3 strand model.

The midplane symmetry allows to consider only half of the model with the symmetry plane as boundary condition $\frac{dI}{dx}(x=\ell)=0$, which corresponds to the boundary condition applied at the joint. As a consequence of the assumption of Equation 3.23, the two halves of the conductor have no mutual inductive coupling. Hence, a symmetric quench can be described by considering an asymmetric quench in half of the conductor length (Figure 3.12: case a. and c. for b. and d. respectively).

The asymmetric quench differs from the ideal symmetric case by (Figure 3.12 a versus b):

1. Modelled length of the cable, ℓ instead of 2ℓ;
2. Modelled quench resistance, R_Q instead of $2R_Q$;
3. The total voltage, V_{tot} versus $2V_{tot}$.

The analytic study will show the current redistribution following a quench in the middle of the magnet to occur slower compared to an asymmetric quench with equal resistance. Note that the current redistribution differential equations in the symmetric 3 strand cable model are written as function of current loop $i(x)$, which relates to current in the strands of a 3 strand cable by (as shown in Figure 3.13):

$$I_2(x) = i(x);$$
$$I_1(x) = I_3(x) = \frac{1}{2}(I - i(x)). \tag{3.27}$$

This analytic study starts with a semi-infinite cable to simplify the analytic equations, followed by a formulation of the joint and cable redistribution in a finite cable. Within the semi-infinite cable study, two cases are studied to get an understanding of the current redistribution dynamics: Sudden strand fracture and constant quench resistance.

Strand fracture As a first example the current dynamics following a sudden rupture of the conductor is presented. Since most superconductors are brittle materials, they are prone to crack when exposed to excessive mechanical load [18]. In case the conductor breaks, the current is instantly forced to the remaining strands, followed by inductive voltages which oppose the current redistribution.

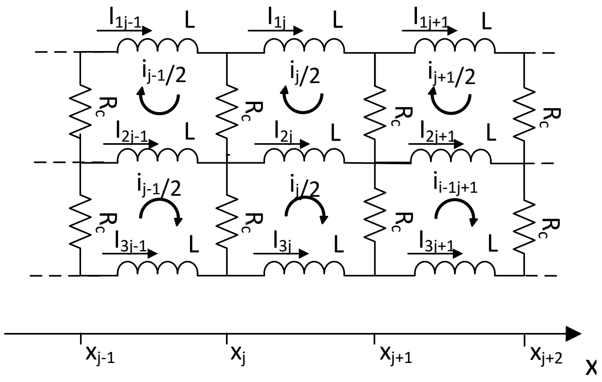

Figure 3.13: Schematic representation of current redistribution within a symmetric 3 strand cable derived from Figure 3.11.

The studied circuit is shown in Figure 3.12c, with infinite R_Q at $t > 0$ and cable length ℓ. Initially a uniform current is carried through three strands of the semi-infinite cable (Equation 3.7), hence for $t < 0$:

$$\begin{aligned} I_2(x,t) &= i(x,t) = I/3; \\ I_1(x,t) &= I_3(x,t) = I/3. \end{aligned}$$

Strand 2 fractures at $t = 0$, which forces all current in the neighbouring strands, hence for $t > 0$:

$$\begin{aligned} I_2(0,t) &= i(0,t) = 0; \\ I_1(0,t) &= I_3(0,t) = I/2. \end{aligned}$$

The second boundary condition is given by the cable at $x = \infty$, where no current will redistribute within the cable due to the high induction effects, therefore:

$$\left.\frac{dI_i}{dx}\right|_{x=\infty} = 0. \tag{3.28}$$

In an effort to generalize the results the current is made dimensionless:

$$\tilde{I}_i = \frac{nI_i}{I}. \tag{3.29}$$

Applying the boundary conditions while solving Equation 3.25, the following current redistribution results:

$$\tilde{I}_2(x,t) = \operatorname{erf}\left(\frac{x}{\sqrt{2\alpha t}}\right); \tag{3.30}$$

$$\tilde{I}_1(x,t) = \tilde{I}_3(x,t) = \frac{1}{2}\left[3 - \operatorname{erf}\left(\frac{x}{\sqrt{2\alpha t}}\right)\right]. \tag{3.31}$$

Note that time and space are directly coupled by the parameter α. The voltage over the strands are given by:

$$V_i(x) = \int_{\zeta=0}^{x} (l - m)\frac{dI_i}{dt}\,d\zeta. \tag{3.32}$$

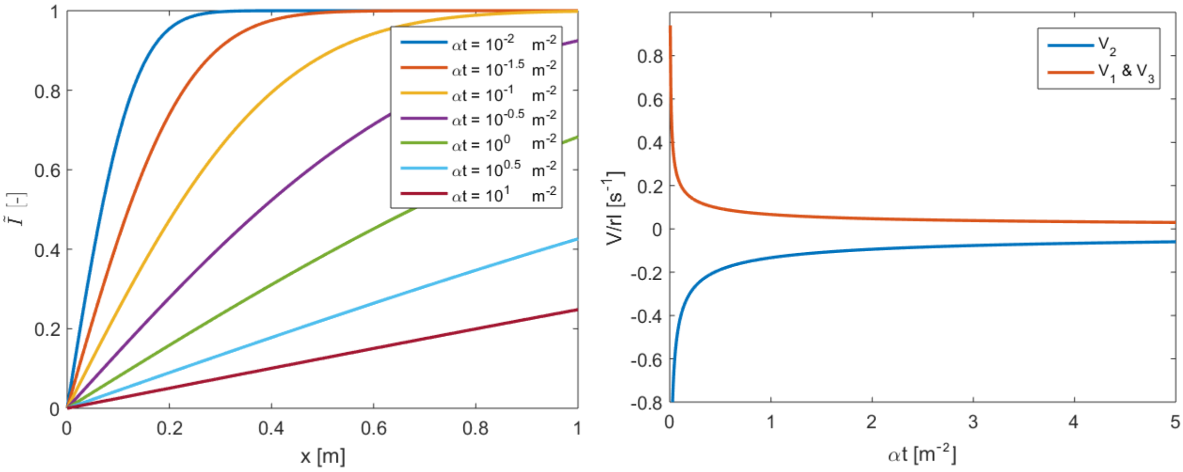

a. Current carried over the length of the broken strand;

b. Inductive voltage of the strands as function of time.

Figure 3.14: Analytic result of the current redistribution due to a 'conductor break' at $x = 0$ inside a semi-infinite cable. Dimensionless current versus location along the length of the broken strand (# 2) for various time instants (left) and inductive voltage over the broken strand (V_2) and the remaining strand (V_1 and V_3) versus time (right). The time is multiplied by the current diffusivity α and the voltage is divided by the inter-strand resistance and initial current for generality.

By substituting Equation 3.25 in Equation 3.32 and using Equation 3.27 and Equation 3.28, the voltages over the strands ($x = \infty$) are found:

$$V_2 = -\frac{r}{2}\frac{di}{dx}\bigg|_{x=0} = -\frac{rI}{3\sqrt{2\pi\alpha t}};$$

$$V_1 = V_3 = \frac{r}{4}\frac{di}{dx}\bigg|_{x=0} = \frac{rI}{6\sqrt{2\pi\alpha t}}.$$

The spatial distribution of the current for several time instances is shown in Figure 3.14a, while the resulting voltages over the three strands as function of time are displayed in Figure 3.14b. At $t = 0$ and $x = 0$, the current is forced instantly from Strand 2 to Strand 1 and 3, which results in an infinite voltage over the various strands. Since the current is redistributed from the quenched to the neighbouring strands, their inductive voltages have opposite signs. The length over which the current distributes expands over time and the voltages approach asymptotically to zero. A direct relation between the duration of the redistribution and electrical diffusion α is found, which is visible from the parametrization of Figure 3.14.

Quench resistance A conductor fracture without any preliminary signs of failure is a very rare event. An infinite resistance is therefore unlikely to emerge instantly. Instead, a quench with constant resistance R_Q is modelled, which appears at $[t = 0, x = 0]$ in Strand 2, as shown in Figure 3.12c.

By assuming again a semi-infinte cable ($\ell = \infty$), the first boundary condition is given by Equation 3.28. Additionally, since the three strands are placed directly in parallel, the voltage over all the strands should be equal [47], hence:

$$V_i(\infty, t) = V_j(\infty, t)\,. \tag{3.33}$$

By evaluating this relation for Strand 2 and 3 it results in:

$$\int_{x=0}^{\infty}(l-m)\frac{di}{dt}dx + R_Q i(0,t) = -\frac{1}{2}\int_{x=0}^{\infty}(l-m)\frac{di}{dt}dx\,. \tag{3.34}$$

By substituting Equation 3.25 in Equation 3.34 and using Equation 3.28, the second boundary condition is as follows:

$$r\frac{di}{dx}\bigg|_{x=0} = \frac{4}{3}R_Q i(x=0)\,. \tag{3.35}$$

The derivation of this boundary condition is presented in more detail for the analogous case of Equation A.7. Since the resistance is finite, the voltage can be made dimensionless:

$$\tilde{V}_i = \frac{nV_i}{R_Q I}. \tag{3.36}$$

Using the initial condition of Equation 3.7 and applying the boundary conditions of Equation 3.28 and Equation 3.34, the the following solution to Equation 3.25 is found:

$$\tilde{I}_2(x,t) = \frac{1}{3}\left[\operatorname{erf}\left(\frac{x}{\sqrt{2\alpha t}}\right) + U(x,t)\right]; \tag{3.37}$$

$$\tilde{I}_1(x,t) = \tilde{I}_3(x,t) = \frac{1}{6}\left[3 - \operatorname{erf}\left(\frac{\tilde{x}}{\sqrt{2\alpha t}}\right) - U(x,t)\right], \tag{3.38}$$

with:

$$U(x,t) = \exp\left[\sqrt{2}\frac{4R_Q}{3r}x + \left(\frac{4R_Q}{3r}\right)^2 \alpha t\right] \operatorname{erfc}\left(\frac{x}{\sqrt{2\alpha t}} + \frac{4R_Q}{3r}\sqrt{\alpha t}\right). \tag{3.39}$$

An analogous expression is found in [47] for a 2 strand cable with a voltage source.

The spatial distribution of the current in the quenched strand for $R_Q/r = 1$ at several time instances is shown in Figure 3.15a with the corresponding voltage over the three strands as function of time displayed in Figure 3.15b. The results show the initial current redistribution to occur gradually after $t = 0$ only near the normal zone at $x = 0$. While the time passes, the current redistributes over longer cable lengths and the current at the normal zone $x = 0$ decreases, which is accompanied by a steady voltage decay. Note that the resistive voltage is again initially compensated by the inductive voltages caused by the internal current redistribution (Equation 3.18). After $\alpha t > 1$, the inductive voltages have approached zero volt, while a resistive voltage caused by the slow redistribution remains.

The intensity of the redistribution is governed by the disturbance ratio of the quench resistance R_Q and the the contact resistance r. For high disturbances the redistribution in the cable will occur locally and a swift drop in voltage is observed. When R_Q/r approaches ∞, the contribution of function $U(x,t)$ is small and the solution can be approximated by Equation 3.30. The following section will study the effect of the disturbance amplitude in more detail.

The current at the normal zone location is found by Equation 3.37 at $x = 0$:

$$\tilde{I}(0,t) = \frac{1}{3}\exp\left[\left(\frac{4R_Q}{3r}\right)^2 \alpha t\right] \operatorname{erfc}\left(\frac{4R_Q}{3r}\sqrt{\alpha t}\right). \tag{3.40}$$

which reveals a time constant t_c of current redistribution within the cable:

$$\tau_c = \frac{1}{\alpha}\left(\frac{3r}{4R_Q}\right)^2 = \frac{9}{8}\frac{r\mathscr{M}}{R_Q^2} \tag{3.41}$$

Analogous to the time constant of the joint τ_j (Equation 3.12), a smaller time constant causes faster redistribution and enhances the stability.

3.2.4. COMBINED REDISTRIBUTION DYNAMICS

Both mechanisms are acting on the magnet simultaneously during quench, therefore their coupling is inevitable. Combining both mechanisms requires modelling a more complex cable of finite length, resulting in an indirect solution with eigenvalue problem. Its full derivation can be found in Appendix A.

To simplify equations, the dimensionless spatial, temporal and disturbance variables are introduced:

$$\tilde{x} = \frac{x}{\ell}; \qquad \tilde{t} = \frac{\alpha t}{\ell^2}; \qquad \mathscr{R} = \frac{4R_Q\ell}{3r}, \tag{3.42}$$

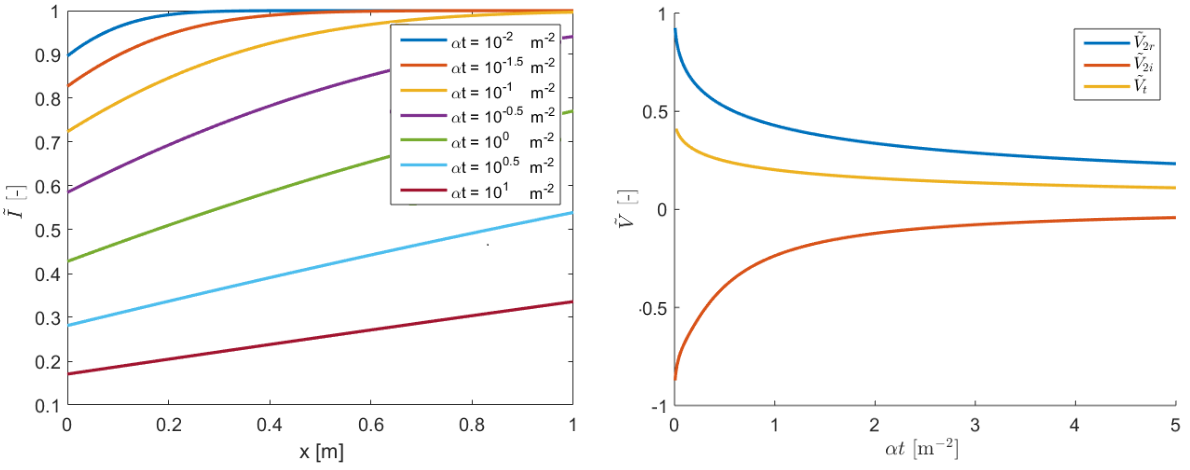

a. Current carried over the length of the quenched strand; **b.** Voltage of the strands as function of time.

Figure 3.15: Analytic result of the current redistribution due to a constant quench resistance inside a semi-infinite cable. Dimensionless current distribution of the quenched strand (# 2) versus location for various time instants (left) and dimensionless resistive and inductive voltage of Strand # 2 and the inductive voltage of the neighbouring strands versus time (right) resulting from a jump in resistance. The time is multiplied by the current diffusivity α for generality.

with dimensionless position $\tilde{x}$ and time $\tilde{t}$. The dimensionless disturbance, $\mathscr{R}$, defines the ratio of the quench resistance to the contact resistance between the strands over the full magnet. The time constant of the combined redistribution is defined as:

$$\tau_{cr} = \frac{\ell^2}{\alpha}. \tag{3.43}$$

Following the derivation of Appendix A, the current in the quenched strand (2) is described by:

$$\tilde{I}_2(\tilde{x},\tilde{t}) = \sum_{m=1}^{\infty} \frac{4\sin\lambda_m}{2\lambda_m + \sin 2\lambda_m} \cos\left(\lambda_m[1-\tilde{x}]\right) e^{-\lambda_m^2 \tilde{t}}, \tag{3.44}$$

with eigenvalue condition:

$$\frac{\mathscr{R}}{\lambda_m} = \tan\lambda_m \quad \text{with} \quad m = 1..\infty. \tag{3.45}$$

To compare the joint model, the cable model and the combined model, all three models need to be normalized. For the semi-infinite cable model a quasi length $\ell = 1$ is used for normalization, while the time constant τ_j of the insulated strand cable model can be written as:

$$\tau_j = \frac{\ell^2}{\alpha\mathscr{R}} = \mathscr{R}\tau_c. \tag{3.46}$$

which shows a direct coupling between the redistribution over the joint and the cable. Note for $\mathscr{R} > 1$, the $\tau_j > \tau_c$, therefore the redistribution is expected to occur dominantly within the cable, while for low values of $\mathscr{R}$ the current passes mainly over the joints.

The quantitative comparison of the three models for $\mathscr{R} = 1$ is shown in Figure 3.16. The current in the quenched strand as function of time is shown in Figure 3.16a for all three models. The current at both $\tilde{x} = 0$ and $\tilde{x} = 1$ are shown for the combined and cable model to indicate the current redistribution along the length of the quenched strand. In the following description the behaviour of the combined model is used as reference in the comparison with the joint and cable model.

The current redistribution initially passes within the cable, following the semi infinite cable approximation I_{cable} at $\tilde{x} = 0$, while virtually no redistribution occurs at $x = \ell$ due to inductive effects. After sufficient time

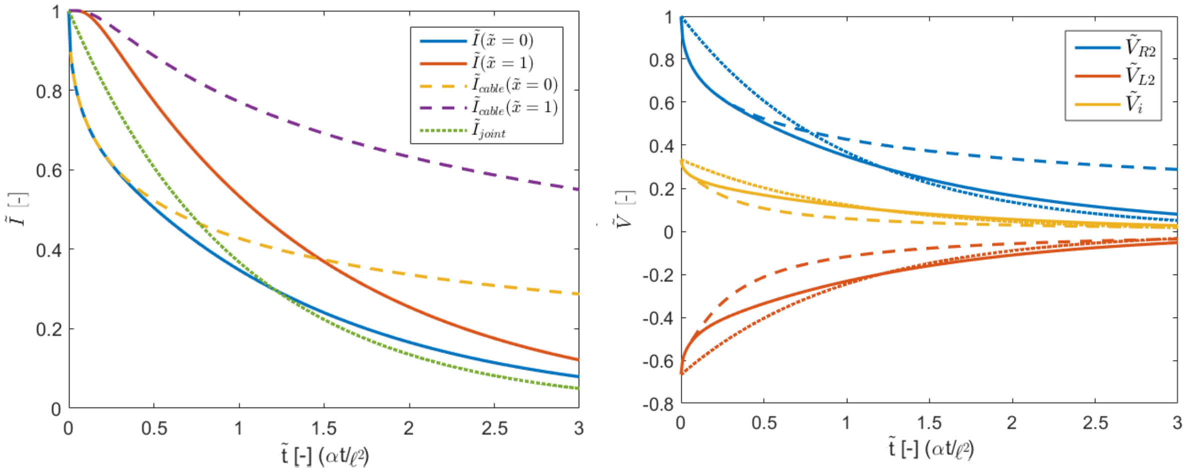

a. Current carried over the length of the quenched strand;

b. Voltage of the strands as function of time.

Figure 3.16: Comparison of the three analytical redistribution models: Dimensionless current distribution versus location for various time instants at $\tilde{x} = 0$ and $\tilde{I} = 0$ (left) and the dimensionless resistive $\tilde{V}_{r2}$ and inductive voltage $\tilde{V}_{i2}$ of the quench strand # 2 and the total voltage over the magnet V_i versus time (right). The joint (short striped), cable (long striped) and combined model (continuous) are compared for $\mathscr{R} = 1$.

	Feather M2	Feather M0
α	$138\,\mathrm{m\,s^{-2}}$	$110\,\mathrm{m\,s^{-2}}$
τ_{cr}	4.5 s	0.18 s

Table 3.6: Current diffusivity parameters and time constant τ_{cr} for Feather M0 and Feather M2.

has passed the current redistribution within the cable reaches $\tilde{x} = 1$. Since the current can redistribute without resistance over the joint, the combined model and the semi-infinite cable model start to deviate due to their difference in boundary conditions. For the period $\tilde{t} > 2$, the redistribution over the joint is dominant and the solution nears the joint model while both the current in the quenched strand and the voltage over the magnet are approaching zero.

The corresponding voltages, consisting of the resistive $\tilde{V}_{R2}$ and inductive voltage $\tilde{V}_{L2}$ of the quenched strand (2) and the total voltage V_i over the magnet, are shown in Figure 3.16b. The initial total voltage at $t = 0$ confirms Equation 3.18. Analogous to the current, the voltage of the combined model follows initially the cable model, until the redistribution has reached $\tilde{x} = 1$. The redistribution over the joints causes a further decrease of the voltage, approaching the joint model.

Similar to the semi infinite cable model of Equation 3.37, the contribution of cable redistribution is governed by dimensionless disturbance $\mathscr{R}$. The current redistribution for $\mathscr{R} = 5$ is shown in appendix, Figure A.1. An increased dimensionless disturbance $\mathscr{R}$ results in a faster response with more current redistribution initially throughout the cable, complying with Equation 3.46. For $\mathscr{R} \to \infty$, keeping all other parameters constant, the redistribution is dominated by the redistribution within the cable and the current behaviour approaches Equation 3.30.

The estimated current diffusivity parameter α for magnets Feather M0 and Feather M2 are shown in Table 3.6 using the parameters of Table 3.1. A typical quench resistance of $10\,\mu\Omega$ will lead to a dimensionless disturbance $\mathscr{R}$ for Feather M0 and M2 of 0.95 and 4.8 respectively, which practically corresponds to the behaviour shown in respectively Figure 3.16 and Figure A.1. Although the current diffusivity α differs only slightly for both magnets, the smaller cable length of Feather M0 enables faster current redistributions over the joint. Therefore the time constant governing the combined model τ_{cr} of Feather M0 is an order of magnitude lower than Feather M2, resulting in faster redistributions and a higher stability.

The solution for the current redistribution problem was found by making use of the analogy with the thermal model. An extensive number of analytical solutions for a variety of thermal problems can be found in [49] [50].

3.2.5. CONCLUSIONS

Current redistributions are likely to occur in the run-up to a quench. The individual analytic models have shown both joint and inter-strand redistribution with their characteristic time τ_j and τ_c. Based on the result, the following observations can be made:

1. Dimensionless disturbance $\mathscr{R}$, defined as the quench resistance R_Q multiplied by conductor length ℓ and divided by the inter-strand resistance r, describes the coupling between the two current redistribution mechanisms during the transient:
    - $\mathscr{R} \ll 1$: Transient dominated by joint redistribution (Figure 3.7b, Equation 3.9);
    - $\mathscr{R} \gg 1$: Transient dominated by redistribution within the cable (Figure 3.7c, Equation 3.19);
    - $\mathscr{R} \sim 1$: Transient consists of a combination of both mechanisms (Figure 3.7 b+c, Equation 3.44).
2. The current diffusivity α defines the spread of redistributed current over the length of the cable. Low values for α result in local current redistributions.
3. The current distributes over the joints in steady state, caused by the inter strand resistance ($\mathscr{R} = 0$);
4. The measured voltage over the magnet is $1/n$th of the resistive voltage over the strand's normal zone, independent of the redistribution mechanism.

For non-insulated multi-strand cables in small to medium size magnets, the dimensionless disturbance $\mathscr{R}$ during a quench is expected to be close to 1, therefore both mechanisms are likely to affect the redistribution of current during a quench. Hence both mechanisms have to be included to describe the current redistribution in the numerical quench model presented below.

3.2.6. DISCUSSION

The complex electric and thermal behaviour needed to be drastically simplified in order to find an analytic solution. The thermo-electric coupling effects between thermal and electric behaviour complicate the problem, requiring numerical solutions. Nevertheless analytic models offer insight in the essence of the various mechanisms, which will help to understand the numerical results in the following section. Within the analytic study the quench was simplified to a suddenly emerging constant quench resistance. In reality the resistance grows with the developing normal zone, therefore a less abrupt response is expected, analogous to the case presented in Table 3.5.

The found time constants τ_c and τ_j are of special interest, since they define the contribution of both current redistribution mechanisms during a quench with constant resistance. Apart from offering insight in the electrodynamics, it is a measure of the cable's stability. However, the time constants originate from distinct mathematical expressions, therefore direct quantitative comparison is not possible. Additionally, the affiliated thermomechanics of a quench, which is not considered in this analytical study, is likely lead to more complex stability effects. The stability of the magnet will be studied in further detail in Section 3.3.7 and Section 3.3.8.

In the derivation of the partial differential equation, higher order effects from the gradient were neglected in the assumption of Equation 3.21. Since the gradients increase for higher $\mathscr{R}$, the accuracy of the results is expected to depreciate. Therefore the study of the conductor break of Equation 3.30, which was accompanied by high gradients at low αt, is an oversimplified representation.

To find an analytic solution the mutual induction has been simplified by the assumption of Equation 3.23. In a coil winding, the subsequent winding turns have considerable mutual coupling, impairing the validity of the assumption. Additionally, the definition of the (mutual) inductance per conductor length $\mathbf{M}$ is complex, since it attempts to capture a complex system within a single parameter [48].

The quench was assumed to occur at the ends of the magnet for simplicity of the analysis. However, the ability to redistribute depends on the location of the quench in the coil. By comparing the equivalent symmetric and an asymmetric electric models (Figure 3.12) with identical quench resistance R_Q, the dimensionless disturbance $\mathscr{R}$ for symmetric case is a fourth of the value of the asymmetric case. Despite the time constant τ_{cr} is reduced by half, the current will redistribute slower in the symmetric case as shown in Figure 3.17. The

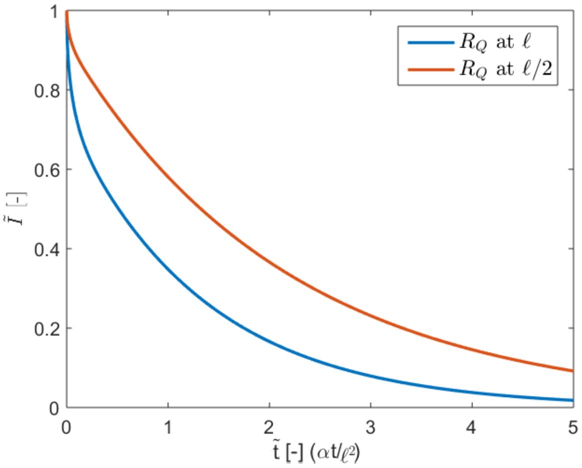

Figure 3.17: Analytically comparing the current flowing through the normal zone during symmetric (R_Q at $\ell/2$) and asymmetric quench (R_Q at ℓ) with equal quench resistance, which suggests stability dependence on the quench location.

higher current flowing through the normal zone results in higher ohmic heating. The magnet is therefore more sensitive to quench close to the center of the magnet resulting in a lower stability. The analytic model is only able to capture a quench occurring either in the center or at magnet's leads. Numerical modelling is required for studying the effect of redistribution for quench occurring at other locations. The dependence is studied in more detail within the stability study of the numerical model, presented in Section 3.3.7.

3.3. NUMERICAL MODEL

Although the analytic models give a valuable insight in the quench behaviour, their application remains limited. Analytical solutions only exist for a limited number of cases, since essential mechanics such as the electro-thermal coupling and material temperature dependencies are practically impossible to describe analytically. In order to describe the quench behaviour more accurately, one needs to turn to numerical models.

Although various LTS Quench modelling programs exist, their use in HTS is fairly limited. LTS quench modelling can be performed either on general purpose multi-physics platforms (OperaFEA, Comsol and Ansys) or with specialized software, such as QUENCH [18], ROXIE, ForQuench and QuenchPro. The LTS normal zone stretches over long lengths of conductor due to the high propagation velocities, which makes including the 3D geometry essential. HTS quench is due to its low propagation speed (Figure 3.5) a very local phenomenon which requires fine meshing for acquiring accurate results, while the 3D geometry only has limited influence. Simulation of HTS quench with LTS Quench packages is thus cumbersome and inefficient.

A HTS tape model is introduced in [21], which describes the thermal propegation of the normal zone within a single tape. It includes an one dimensional thermal finite difference model (Analogous to the model discussed in Section 3.3.1) and a superconductor material model presented in [36]. The model was validated using experimental data of the normal zone propagation velocity and the minimal quench energy in a single SCS4050 tape supplied by SuperPower. Based on this tape model, a full 3 dimensional multi-physics quench model is presented in [9] which includes the 3D magnet geometry. This program describes the electro-magnetic and thermal behaviour by solving Kirchoff's Voltage and Current Laws fully coupled to the discrete heat equation from a network model. To reduce the computation complexity, it introduces sparsity in the induction matrix by using the multi-level fast multipole method (MLFMM) [51], which reduces the complexity of the mutual inductance calculation by grouping elements with sufficient separation distance into a spherical harmonic expansion. Nevertheless this extensive 3D simulation result in individual quench case computation duration of the FM2 model in the order of 24 hours, due the high number of equations (approximately 25000 DOF).

To explore the behaviour of HTS cable quench within its broad operating domain, efficient and versatile modelling is required. The model should encompass sufficient detail to capture the behaviour while offering

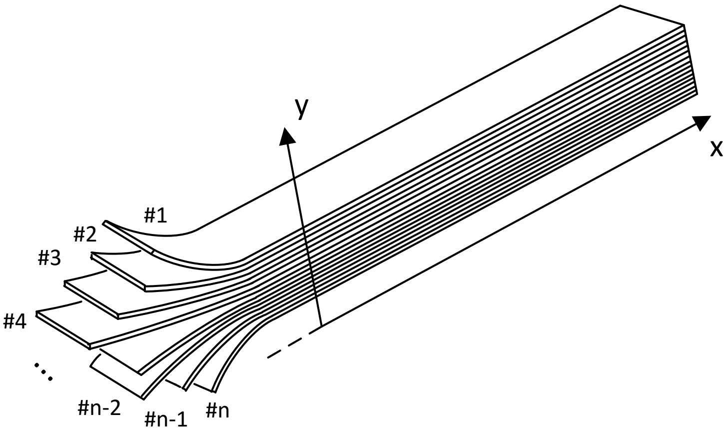

Figure 3.18: Schematic overview of the modelled tape stack cable geometry with n strands and the coordinate axis used throughout this analysis.

the versatility and efficiency to cope with the unknowns, such as the quench cause. The presented model aims to explore the behaviour of quench and cope with modelling uncertainties and variations in the magnet geometry and quench disturbance parameters. Hence the model's iteration speed and versatility are key for performing sensitivity analysis and parameter sweeps. Apart from the quench behaviour itself, this model offers insight in the quench behaviour for the detection design, discussed in the next chapter.

The model simplifies the HTS cable quench to a 2 dimensional thermal-electric model, while the magnetic coupling in the cable is captured in the induction matrix **M** (Table G.2) [9]. The thermal and electric models are both discretized and have distinctive spatial distributions, since the thermal quench behaviour is local while current redistributions stretch over the entire length of the magnet, which is discussed in Section 3.3.3.

The stacked tape cable geometry as shown in Figure 3.18 was chosen for simplicity and generality of the model. The cable consists of n strands with electric and thermal interface with their neighbouring strand(s) over the entire width of the tape. Although the modelled geometry is simplified with respect to a Roebel cable, since HTS quench is a very local phenomena the 3D geometry from the cable and magnet is expected to have only limited effect on the quench itself. Apart from simplifying the equations, it will prove the generality of cable quench behaviour.

An overview of the coupling between the thermal, electric and superconductor model is shown in Figure 3.19. Since quench is the thermal electric behaviour of a superconductor, the current sharing model (i.e. superconductor model) forms the connection between the thermal and electric domain. The calculated normal zone ohmic heating and resistance are used as input of respectively the thermal and electric model, while the resulting local temperatures and current define the state of the superconducting strand. Both electric and thermal aspects of HTS cable quench modelling will be regarded subsequently in more detail. This study leads to the formulation of the heat equation, current redistribution and superconductor model, followed by a quantitative description of their mutual coupling. The models of [21] and [9] are referred to as 1D model and 3D model respectively in the remainder of this report.

3.3.1. THERMAL MODEL

The thermal model is based on the one dimmensional finite difference model presented in [21]. This model describes the 1D propegation of a normal zone in a single strand and was validated with experiments. It aimed for better understanding of the quench phenomena and gave valuable insight in the physical behaviour, such as temperature distributions and normal zone velocity dependencies.

In order to describe the thermal quench development in a cable the model should be extended to include the thermal diffusion between strands. In an effort to simplify the model and to enhance calculation efficiency,

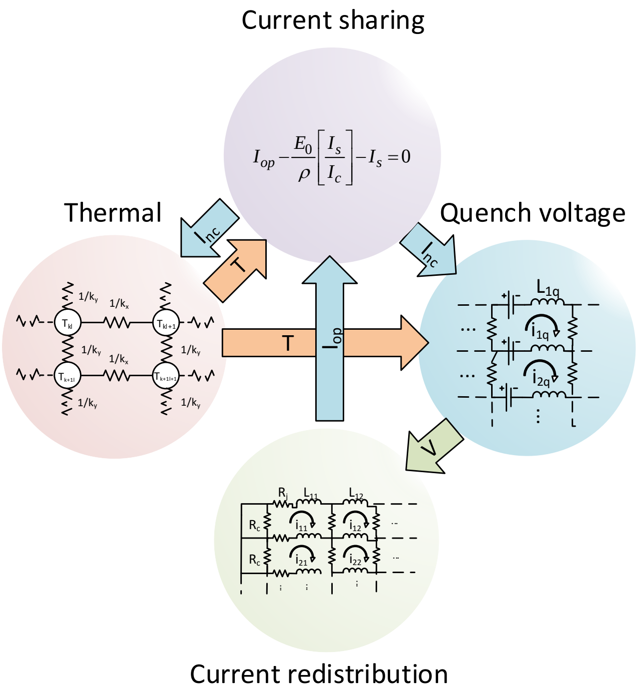

Figure 3.19: Coupling between the superconductor, thermal and current redistribution model. Based on the temperature of each thermal element T_{il} and the carried current I_{iq}, the normal current $I_{nc,il}$ of the element is calculated. This parameter serves as input for the thermal and electric model to calculate respectively the the ohmic resistance and ohmic heat.

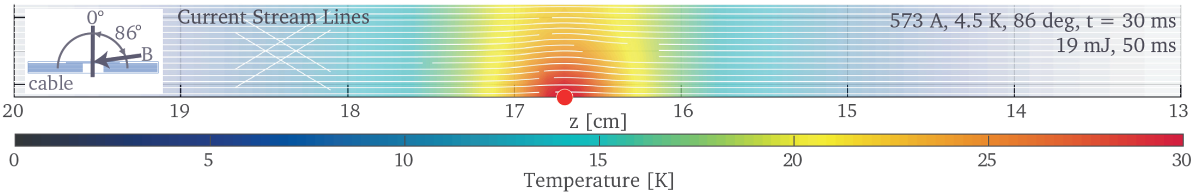

Figure 3.20: Quench propagation over the width of the tape by a 50 ms pulse applied at the tape's edge. At t =30 ms, the gradient over the witdh of the cable is less than 5 K [9].

the number of elements should be kept minimal. Although tape quench is in principle a 3 dimensional electromagnetic thermal phenomena, earlier studies have shown the propagation over the width and thickness to be practically instantaneous (ms). After this brief transient, the quench propagates as a front along the length of the conductor [9], as shown in Figure 3.20. A simple example can show this fact using an one dimensional heat problem with constant hotspot temperature, given the thermal time constant τ_h [50]:

$$\tau_h = \frac{\ell^2 C}{\pi^2 k}, \tag{3.47}$$

with the material and cable properties found in Section 3.2.1, a time constant for the tape's width and thickness of respectively 36 ms and 11 µs are found. Additionally, if part of the tape has reached T_{cs}, all current is forced in the remaining superconducting part of the conductor, therefore reducing locally the current sharing temperature T_{cs}. Propagation over the width is therefore expected to be virtually instantaneous, especially at higher current density J. Hence, the thermal behaviour of the model is governed by the heat balance of Equation 3.1 in 2 dimensions:

$$C(T)\frac{\partial T}{\partial t} = \frac{d}{dx}\left[k_x(T)\frac{\partial T}{\partial x}\right] + \left[k_y(T)\frac{\partial T}{\partial y}\right] + \rho J^2 + P_e. \tag{3.48}$$

The individual strands are discretized into pxn elements as shown in Figure 3.21. The discretized cable elements are linked by thermal resistances to adjacent elements of its own and neighbouring strands. The

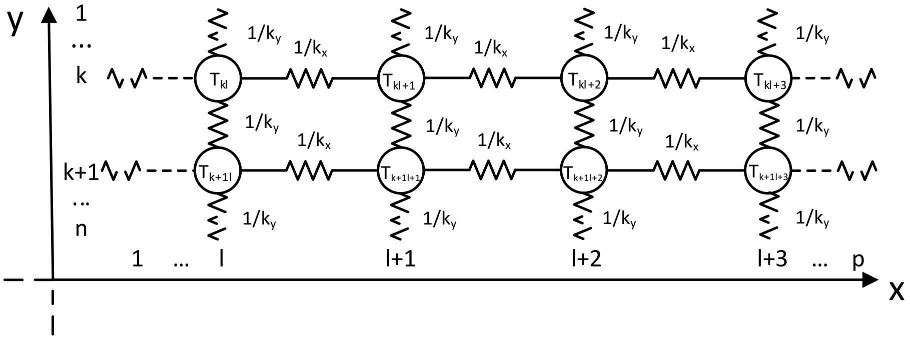

Figure 3.21: Schematic representation of the discretized 2D thermal network model of a n-strand cable. The cable is discretized in $n \times p$ elements, while their state described by temperature T_{ik}. The longitudinal and transverse thermal resistances $1/k_x$ and $1/k_y$ define the conduction of heat between the elements.

discretized heat balance for Element l of Strand i is given by:

$$C(T_{il})\frac{dT_{il}}{dt} = k_x(T_{il})\frac{2T_{kl}-T_{kl-1}-T_{kl+1}}{dx_t^2} + k_y(T_{il})\frac{2T_{il}-T_{i-1l}-T_{i+1l}}{h^2} + \rho_{il}(T_{kl})I_{nc,il}^2 + P_{d,il}\,. \tag{3.49}$$

with strand and element indices i and l, tape thickness h, element temperature T_{il}, thermal capacity of the element C, thermal conductivity along the conductor k_x and transverse thermal conductivity k_y. The initial disturbance $P_{d,kl}$, normal zone resistance $R_{nz,kl}$ and normal current $I_{nc,kl}$ are discussed later on in this chapter, while the (thermal) properties k_x, k_y and C are given by [21]:

$$C(T_{il}) = dx_t w \sum_{q=1}^{2} \rho_{d,q} h_q C_q(T_{il}); \quad k_x(T_{il}) = w \sum_{q=1}^{2} h_q k_q(T_{il}); \quad k_y(T_{il}) = w dx_t \left[k_c^{-1} + \sum_{q=1}^{2} \frac{h_q}{k_q(T_{il})}\right]^{-1}, \tag{3.50}$$

with the indices q indicating the layers of the tape (copper, hasteloy), tape width w, layer thickness h_q and the thermal contact conductivity between the strands k_c. The material and cable properties applied in the model are found in Section 3.2.1 and [21]. The element normal zone resistance ρ_{il} is given by:

$$\rho_{il} = \frac{dx_t}{w}\left[\sum_{q=1}^{2} \frac{h_q}{\rho_q(T_{il})}\right]^{-1}. \tag{3.51}$$

with electrical resistivity ρ_q of the various tape layers q. The normal zone resistance ρ_{il} and normal current I_{nc} form the link between the current and thermal model, as will be shown in Section 3.3.3.

Since the heat equation is a ’stiff’ problem standard solvers become unstable unless forcing very small time steps at the cost of computation time. At area’s of stiffness standard variable step solvers struggle to meet tolerances. Stiff solvers, such as MATLAB’s ode15s, are specialized for these kind of problems.

INITIAL DISTURBANCE

The spatial distribution and duration of the initial disturbance is largely dependent on the type of event. Since the causes of HTS quench remain ill defined, analysing the sensitivity to the unknown is of great importance. To normalize this quench behaviour study, a disturbance is modelled as a square heater pulse with amplitude p_h:

$$P_d(x,t) = p_h(u(x-x_q+\ell_h/2) - u(x-x_q-\ell_h/2))(u(t)-u(t_h-t))\,. \tag{3.52}$$

with step function $u(\xi)$, position of the applied disturbance x_q, the amplitude of the disturbance p_h, the disturbance length ℓ_h and duration t_h. A disturbance duration t_h of 50 ms and length ℓ_h of 1 mm was chosen to comply with the analogous 3D quench model study of [9]. The disturbance energy is spread homogeneously over the elements which lie within ℓ_h. The total disturbance energy is now found by:

$$E_d = p_d t_h\,. \tag{3.53}$$

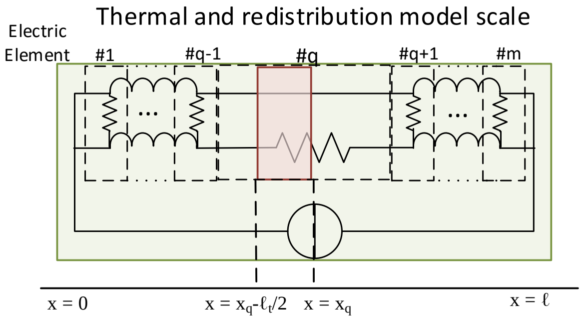

Figure 3.22: Length scale of electric (green) and thermal model (red). The thermal model only includes half of the conductor affected by the normal zone $x = x_q + [-\ell_t, 0]$, using the assumed symmetry. The thermal model is assumed to lie entirely in electric model Element q. Hence, the current flowing through strand i of the thermal model is I_{iq}.

The total disturbance energy E_d is used to measure the thermal instability of the cable. The minimum disturbance energy needed to cause a thermal runaway is called the Minimum Quench Energy or MQE, which is discussed in further detail in Section 3.3.7.

BOUNDARY CONDITIONS

To limit the number of elements p and making use of the locality of the quench, the thermal model only spans the region close to the normal zone $x = x_q + [-\ell_t/2, \ell_t/2]$. Hence, the modelled conductor length in the thermal model ℓ_t $(= p dx_t)$ is significantly smaller than the total conductor length ℓ of the magnet, as shown in Figure 3.22. Thereby reducing the number of elements, while dx_t can be kept small to increase the resolution for describing the high temperature gradients in the normal zone. Based on the presented thermal model, the following observations can be made:

1. The geometry of a stacked tape cable is constant along conductor's length;
2. The thermal model length ℓ_h is small compared to ℓ, hence only limited current redistribution occurs within cable modelled by the thermal model;
3. The disturbance is symmetric at $x = x_q$. (Equation 3.52).

Hence, the normal zone is practically symmetric around $x = x_q$, resulting in:

$$\frac{dT}{dx} \approx 0 \quad \text{at} \quad x = x_q. \tag{3.54}$$

A symmetric normal zone only requires modelling half of the conductor $x = x_q + [-\ell_t/2, 0]$ by using the boundary condition of Equation 3.54. Since the model only captures a small section of the coil as shown in Figure 3.22, the heat diffusion to the rest of the conductor is approximated by:

$$\frac{dT^3}{dx^3} = 0 \quad \text{at} \quad x = x_q - \frac{\ell_t}{2}, \tag{3.55}$$

which causes the gradient of the heat conduction to be zero at the model's boundary. This second boundary condition is an approximation which applicable if the temperature increase near the model's boundary remains limited ($T(x = -\ell_t/2) - T_{op} < 1$ K). Hence slower quenches require longer ℓ_t due to higher conductivity but less spatial granularity due to smaller gradients. The element size is therefore determined iteratively to comply with the observed quench behaviour.

3.3.2. ELECTRICAL MODEL

The analytic model presented the current redistribution mechanisms which allow the current to bypass the quench. The current can both redistribute throughout the cable and over the joints. A numerical model is required in order to model the full inductive coupling governing the current redistribution during quench.

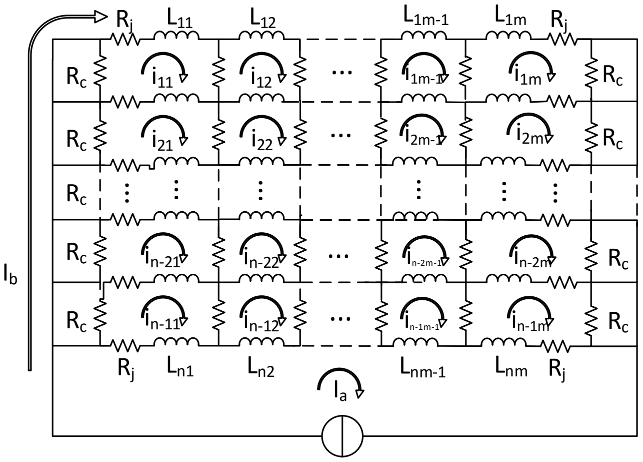

Figure 3.23: Schematic of a discretized cable redistribution model consisting of n-strand and m elements. Loop currents I_a and I_b describe the transport currents, while current redistribution loops i_{ij} describe the current within the cable. Contact resistance between the strand elements R_c and joint resistance R_j are homogeneous throughout the cable, while L_{ij} follows from the induction matrix $\mathbf{M}$.

To describe the current redistribution, a cable consisting of n strands is discretized along its length into m elements. The electrical circuit is shown in Figure 3.23. The current can redistribute both between the elements of the cable and over the joints. Analogous to Equation 3.19, the redistribution current loop i_{ij} is governed by:

$$\begin{aligned}\sum_{l=1}^{m}\left[\sum_{k=1}^{n-1}(M_{ij,kl}-M_{ij,k+1l}-M_{i+1j,kl}+M_{u+1j,k+1l})\frac{di_{kl}}{dt}+(M_{ij,1l}-M_{i+1j,1l})\frac{dI_a}{dt}+(M_{ij,nl}-M_{i+1j,nl})\frac{dI_b}{dt}\right]&\\ =-2R_c i_{ij}-\begin{cases}R_j(2i_{1j}-i_{2j}+I_a) & \text{for } i=1\\ R_j(2i_{ij}-i_{i-1j}-i_{i+1j}) & \text{for } 1<i<n-1\\ R_j(2i_{n-1j}-i_{n-2j}-I_b) & \text{for } i=n-1\end{cases}&\\ +V_{ij}-V_{ij+1}+\begin{cases}R_c i_{i+1j} & \text{for } j=1\\ R_c(i_{ij-1}+i_{ij+1}) & \text{for } 1<j<m\\ R_c i_{ij-1} & \text{for } j=m\end{cases}&\end{aligned} \tag{3.56}$$

with indices i and k referring to the tape ranging from 1 to $n-1$, while j and l indicate the cable element, which spans from 1 to m. Moreover, the mutual induction $M_{ij,kl}$ between the elements, joint resistance R_j and contact resistance R_c. Since a current supply cannot be captured with Kirchoff's second law, variables I_a and I_b are introduced, as shown in Figure 3.23:

$$I_b - I_a = I\,. \tag{3.57}$$

The potential of the two loops should be equal to each other, i.e. the voltage over the current source:

$$\begin{aligned}&\sum_{j=1}^{m}\left[\sum_{l=1}^{m}\left[\sum_{k=1}^{n-1}(M_{1j,kl}-M_{1j,k+1l})\frac{dI_{kl}}{dt}+M_{1j,1l}\frac{dI_a}{dt}+M_{1j,nl}\frac{dI_b}{dt}\right]-V_{1j}\right]+R_j(2I_a+i_{11}+i_{1m})\\ &\quad=\sum_{j=1}^{m}\left[\sum_{l=1}^{m}\left[\sum_{k=1}^{n-1}(M_{nj,kl}-M_{nj,k+1l})\frac{dI_{kl}}{dt}+M_{nj,nl}\frac{dI_b}{dt}+M_{nj,1l}\frac{dI_a}{dt}\right]+V_{nj}\right]+R_j(i_{n1}+i_{nm}-2I_b)\,.\end{aligned} \tag{3.58}$$

Note that Equation 3.56, Equation 3.57 and Equation 3.58 over-define the system of equations. Hence current loop i_{n-1m} was left redundant. It served as validation of the system's equation within the MATLAB implementation. The remaining equations are written in a state space equation:

$$\mathbf{A}\dot{\vec{\imath}}+\mathbf{B}\vec{\imath}=\mathbf{v}\,, \tag{3.59}$$

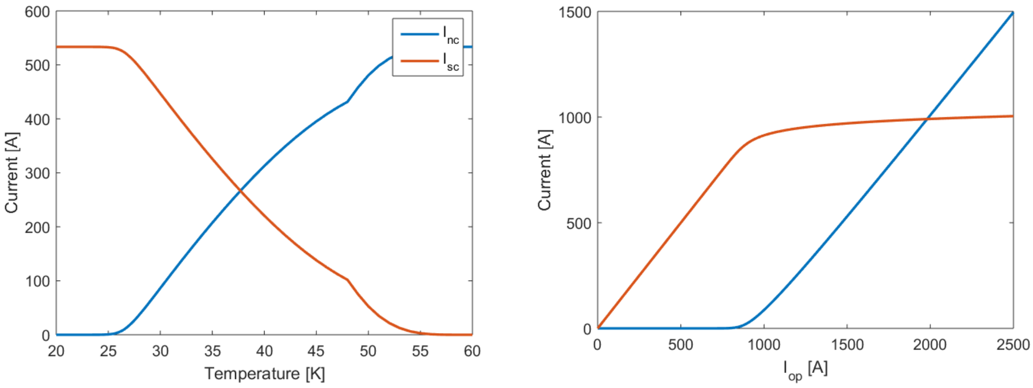

a. Temperature dependence at 970 A mm^{-1}, 17 T; **b.** Current dependence at 20 K, 17 T.

Figure 3.24: Example of normal and superconducting current I_{nc} and I_{sc} following from the current sharing model [52] at a background field of 17 T.

with loop currents $\vec{\imath}$, loop induction matrix **A**, resistance matrix **B** and voltage vector $\vec{v}$. The electrical model consists of a total of $(m \times n) + 1$ equations.

Since the loop currents $\vec{\imath}$ are not practical to apply in the superconductor model, the equations were transformed to current I carried per strand element using transformation matrix **T**, analogous to Equation 3.27:

$$\vec{I} = \mathbf{T}\vec{\imath}\,, \tag{3.60}$$

with transformation matrix **T**. The currents $\vec{I}$ are used in the superconductor model, described below. The matrices **A**, **B** and **T** can be found in Appendix C.

PARALLEL PATH METHOD

In the analytical model a sharp transition between normal and superconduction at T_t was assumed. As already mentioned, this is an oversimplified representation. A superconductor can be modelled as a normal and superconducting element in parallel, carrying respectively I_{sc} and I_{nc} [21]:

$$I_{op} = I_{sc} + I_{nc}\,, \tag{3.61}$$

with superconducting current I_{sc} and normal current I_{nc}. Hence, when current is applied to a supercoductor, the superconducting element will carry all current up to I_c, since it experiences no resistance. After the superconductor is saturated, the remaining current is forced into the normal conductor. An implicit approximation can be given as [21]:

$$I_{op} - \frac{E_0}{\rho}\left[\frac{I_{sc}}{I_c}\right]^N - I_{sc} = 0\,, \tag{3.62}$$

where E_0 is the voltage threshold at which I_c is determined (common $E_0 = 10\,\mu\text{V}$) and N the n-value which is a characteristic of the superconductor. Higher n-values lead to sharp transitions from super to normal conduction. Although no exact solution of this implicit expression exist, it can be solved using a Newton Raphson method.

The critical current I_c is found using the model presented in [52]. The I_c model is based on critical current measurements of tape supplied by Fujikura and fitted as function of the prevailing temperature T, field strength B and field angle α. The critical current I_c is scaled to the EUCARD2 standard of 600 A m^{-1} at 4.2 K, 20 T field strength at 90° field angle [53].

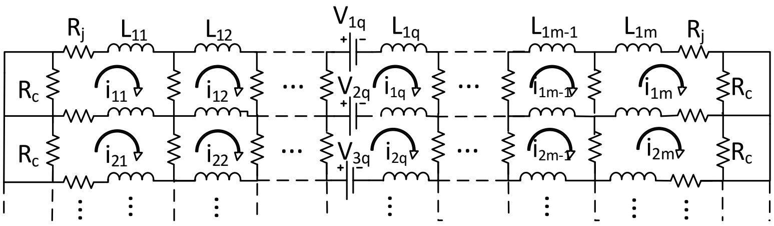

Figure 3.25: Resistive voltage from normal zone ($V_i q = \sum \rho J_{nc}$) implementation in the current redistribution model.

3.3.3. COUPLING

The interface between the superconductor, thermal and current redistribution model was schematically shown in Figure 3.19. The full length of the conductor is modelled by the electrical model, while the thermal model spans only a fraction of one of the current redistribution elements, saving valuable computation time. The redistribution element which includes the heat model is denoted by Element q and is located at $x = x_q$ as shown in Figure 3.22. Based on the current carried by current model Element q, I_{iq}, the normal current I_{nc} in heat model Element il is calculated by a discretization of Equation 3.62:

$$I_{iq} - \frac{E_0}{\rho_n(T_{il})}\left[\frac{I_{sc,il}}{I_c(T_{il})}\right]^N - I_{sc,il} = 0. \tag{3.63}$$

The normal current of thermal model Element il, $I_{nc,il}$ found by Equation 3.61, is addressed in the heat model of Equation 3.49 as input for the ohmic heating.

To include the quench resistance in the current redistribution model of Equation 3.59, the resistive normal zone voltage per strand needs to be calculated. Since the thermal model lies completely within redistribution element q as shown in Figure 3.25, it is found:

$$V_{ij} = \begin{cases} \sum_{l=1}^{p} \rho_{nz,il} I_{nc,il} & \text{if } j = q, \\ 0 & \text{else.} \end{cases} \tag{3.64}$$

The element normal zone resistance $\rho_{nz,il}$ and normal current $I_{nc,qj}$ are respectively found by Equation 3.51 and Equation 3.63. The quench voltage experienced by the redistribution loop currents i_{ij} is found by:

$$\vec{v} = \mathbf{T}^{-1}\vec{V}, \tag{3.65}$$

which is used directly as input for Equation 3.59. The mutual coupling between the electric and thermal model makes simultaneous solving necessary. Due to non-linearity introduced by the temperature dependent thermal properties, it is not possible to write the thermal model in a linear state space equation. Both models are therefore solved simultaneous by the solver:

$$\begin{bmatrix} \mathbf{A} & 0 \\ 0 & \mathbf{C}(T) \end{bmatrix} \begin{bmatrix} \dot{\vec{i}} \\ \dot{\vec{T}} \end{bmatrix} + \begin{bmatrix} \mathbf{B} & 0 \\ 0 & \mathbf{K}(T) \end{bmatrix} \begin{bmatrix} \vec{i} \\ \vec{T} \end{bmatrix} = \begin{bmatrix} \vec{v} \\ \rho \vec{I}_{nc}^2 \end{bmatrix} + \begin{bmatrix} 0 \\ \vec{P}_h \end{bmatrix}, \tag{3.66}$$

with thermal capacity matrix $\mathbf{C}(T)$, thermal conductivity matrix $\mathbf{K}(T)$, current induction loop matrix $\mathbf{A}$, resistance loop matrix $\mathbf{B}$, coordinate transformation $\mathbf{T}$, heater power P_h, quench voltage $\vec{v}$ and ohmic heating $\rho \vec{I}_{nc}^2$. For the simulations the values of Table 3.7 are used as baseline, unless stated differently.

3.3.4. QUENCH BEHAVIOUR

The model offers insight in the thermal and electric quench behaviour of a HTS cable. To study the modelled quench behaviour in various cases, the quench event is divided into three subsequent phases:

1. Drift: All strands are superconducting, i.e. below T_{cs};
2. Prequench: Individual strands reached the current sharing or normal conducting domain, while others are still superconducting;

		Value	Unit	Description
Heater	t_h	50	[ms]	Heater pulse time
	ℓ_h	1	[mm]	Heater length
Thermal	p	201	[-]	Elements thermal model
	dx_t	1	[mm]	Thermal element length
Electric	m	168	[-]	Elements electrical model (21 for MQE)
	M_{ij}	Table G.1	[µH]	Mutual induction matrix FM2 [9]

Table 3.7: Simulation parameters during numerical studies of Feather M2.

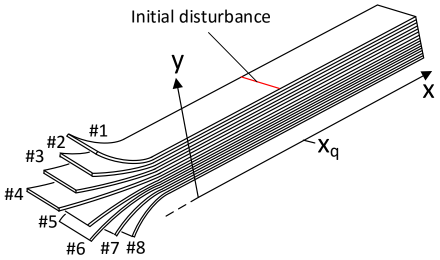

Figure 3.26: Schematic overview of the modelled tape stack cable geometry with 8 strands and the initial disturbance applied at the top tape at $x = x_q$.

3. Full quench: All strands have crossed T_c and entered the normal conducting state.

These phases characterize the quench behaviour [9] and are discussed individually based on two cases. The simulations for Case 1 and Case 2 are performed using an 8 strand model at a current density J of 650 A mm^{-2} and 1250 A mm^{-2} respectively. The conductor is initially at nominal operation (Equation 3.7). At $t = 0$ the top strand is perturbed by the energy E_h as shown in Figure 3.26, followed by the response of Case 1 and 2 shown in respectively Figure 3.27a and Figure 3.27b.

DRIFT

The period running up to a quench until one strand passes T_{cs} is called as drift. In Case 2 (Figure 3.27b) a long drift is shown (period between $t = 0$ and the left arrow). Since all strands are fully superconducting, no normal zone, joule heating or current redistribution are present. Apart from the quench cause which could be an electromagnetic phenomena (e.g. flux jumps), this region is a pure thermal balance between the disturbance, thermal conduction and cooling. The behaviour in this region is out of this study's scope since the cause of a quench in a HTS cable is presently unknown and a simplified initial disturbance is assumed in the model. The heater pulse is kept small (t_h=50 ms), since the computation of the drift behaviour requires additional computation steps.

The following remarks can be made:

1. The disturbance is the sole driving force behind the development of a potential quench;
2. Low power disturbance causes slow temperature rise and long drift;
3. During the drift the heat can diffuse over the cable, causing homogeneous temperature rise of the entire cable, which increases the MQE.

Whether the drift is causing the top strand to reach the current sharing temperature T_{cs} is purely dependent on the heat balance, since no Joule heating from normal conduction is present. Even if the T_{cs} is locally reached the superconductor can stabilize depending on the quench case. As will be shown in the upcoming section, the MQE is defined as the minimum energy required to cause a thermal runaway, which depends on the size and shape of the disturbance, magnet/cable geometry and operation conditions. These parameters are studied in further detail in Section 3.3.8.

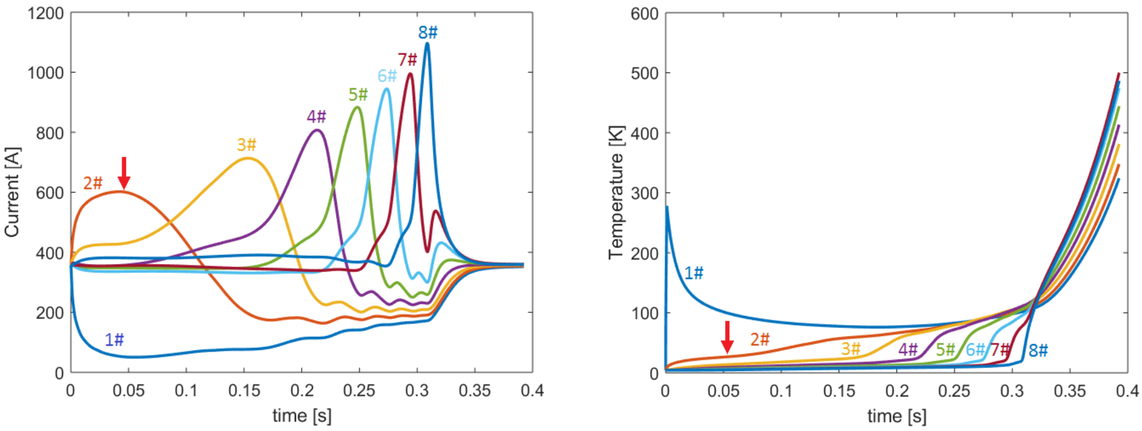

a. Case 1: 8 strand model at 650 A mm^{-2}, 1 ms 350 mJ pulse.

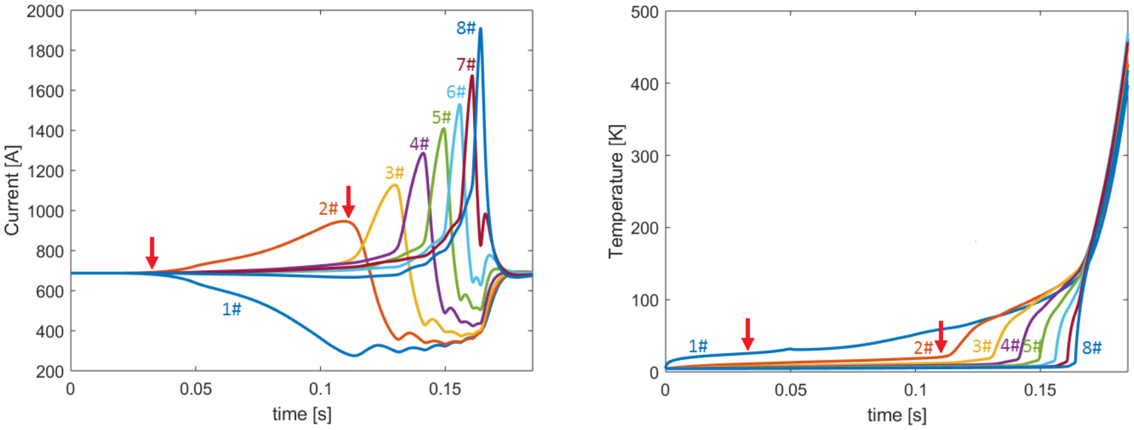

b. Case 2: 8 strand model at 1250 A mm^{-2}, 50 ms 185 mJ pulse.

Figure 3.27: Numerically found current distribution over the various strands in the cable (left) and the hotspot temperature of each strand (right) as function of time during two quench events. Case 1 (Figure 3.27a) shows an event with an high power disturbance at $t = 0$, followed by diffusion of this thermal load, which causes the strands to quench one by one, eventually resulting in a full quench. Case 2 (Figure 3.27b) shows a quench event at high current with slower disturbance, which causes perturbed the strand to barely reach T_{cs}. When the strand gets resistive, the emerged ohmic heating causes a thermal runaway of the cable.

PREQUENCH

When the temperature of one of the strands reaches T_{cs}, local resistance in the cable arises. Its ohmic heating contributes as additional heat input while the emerging resistance initiates current redistribution. Both current redistribution and ohmic heating are therefore dependent of the spread of the normal zone, which was found to be proportional to the current density for single tape quench (Section 3.2.2). Since the current in the quenched tape is not constant due to current redistributions, more complex behaviour is expected. The prequench of the two cable quench cases are considered in more detail to demonstrate the various mechanisms.

Case 1 (Figure 3.27a) shows rapid heating of Strand # 1 due to the disturbance at $t = 0$, causing the current to redistribute primarily to the neighbouring Strand # 2. Since this strand has sufficient load margin, the new current redistribution is well below I_c, hence remaining superconducting. Meanwhile the heat diffuses longitudinal over the length of Strand # 1 and gradually transverse to Strand # 2. Since Strand # 2 carries momentarily a higher current, its current sharing temperature T_{cs} is lowered. When Strand # 2 reaches T_{cs} a resistance emerges and its current redistributes again (denoted by the red arrow). As the number of remaining superconducting strands reduces, the current density in these strands rises and hence the T_{cs} is lowered. Therefore the amount of heat required to quench subsequent strands reduces, causing a cascade of individual strand quenches with increasing frequency accompanied by higher current densities. When 7 tapes have quenched, the current density in Strand # 8 has approached J_c at T_{op}, therefore only little heat is needed to quench the last strand.

Since the current density is relatively low, the ohmic heating remains small and the thermal heat of the initial disturbance is the main quench incentive. Hence a high disturbance is needed to cause a thermal runaway. The stability of the superconductor at these low currents is primarily governed by the transverse thermal diffusion, which causes the other strands to quench, versus the cooling and longitudinal thermal diffusion, which mitigates the effect of the initial disturbance. For higher current densities the T_{cs} is reduced, therefore a lower stability is expected, as is shown in Case 2.

Case 2 (Figure 3.27b) shows a quench at high current, with a more gradual initial disturbance. Although its disturbance causes Strand # 1 to merely exceed T_{cs} (left arrow), it results in a swift chain of successive individual strand quenches. Contrary to Case 1, due to the reduced ability to adopt the current by the other strands, the quench of the first strand already issues the runaway with the ohmic heating as main driving force. The high current density causes a rapidly growing normal zone, while the induction limits the current redistribution. As a consequence, the high ohmic heating causes a steep temperature rise of the conductor. The low T_{cs} caused by the higher current density J results in a very unstable behaviour. After Strand # 1 gets barely resistive, the stability of the entire cable is lost. Therefore the cable's stability relies on the stability of the individual strands.

Based on the two analysed cases, the following current density dependence is observed [34]:

1. Low current density: High stability because of limited ohmic heating and sufficient time for redistributions, with disturbance energy as main driving force.
2. High current density: Low stability governed by stability of individual strands. Locally reaching T_{cs} due to the disturbance causes a thermal runaway of the entire cable.

The difference in stability of both cases is observed from the quench duration and the applied energy, which are both approximately a factor 3 higher for Case 1. These two cases show the extremities of current dependence of cable's stability. At intermediate current densities a balance between disturbance energy diffusion and ohmic heating is expected to drive the cable quench. The stability as function of current is studied in Section 3.3.7, while the sensitivity to other parameters are considered in Section 3.3.8.

FULL QUENCH

The quench of the last strand is followed by a thermal runaway, referred to as the full quench phase. Since all strands have exceeded T_c, no superconducting current remains. During full quench all strands have similar resistance, therefore the current will redistribute evenly again over all strands and the temperature of the entire cable will rise rapidly due to its ohmic heating. Since Strand # 8 carried the highest current at the end of the prequench in both Case 1 and 2, it shows the highest increase of temperature during full quench.

Although the speed of thermal runaway is of interest for defining the requirements of the quench detection, its dynamics are simple and do not require extensive modelling. The slope of the thermal runaway agrees roughly with the approximation found by Equation 3.2 and scales with the square of the operation current. The full quench is regarded in further detail in Chapter 4 concerning detection design.

3.3.5. CURRENT REDISTRIBUTION

The current redistribution due to a constant quench resistance was studied using the analytic models in Section 3.2.3. In order to validate the result, it is compared to the results of the numerical quench model. To produce a quench with constant resistance using the numerical model, the normal zone propagation and therefore the ohmic heating should remain small. A low current density J case was found to be most suitable. To allow the resistance to appear nearly instantly, a very small pulse time is chosen (1 ms). The quench behaviour of this particular case was already studied in the analysis above within its time domain in Section 3.3.4 (Case 1, Figure 3.27a). The normal zone resistance of Strand # 1 over time is shown in Figure 3.28a, which shows a plateau at 18 μΩ after 1 ms. The resulting spatial distribution of the current over the length of Strand # 1 is shown for various time intervals in Figure 3.28b with solid lines.

The initial disturbance in the numerical model is applied in the centre of the magnet. A symmetric quench can be approximated by the analytic description of Equation 3.44 by applying the symmetry shown in Section 3.2.3 and Figure 3.12c. By using the observed quench resistance of 18 μΩ together with the parameters

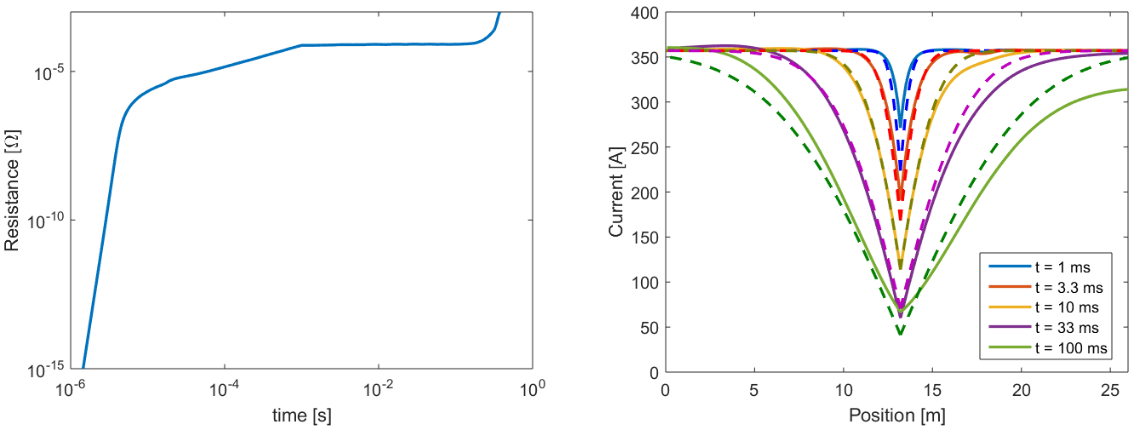

a. Quench resistance Strand # 1 **b.** Spatial current distribution Strand # 1

Figure 3.28: Numerically found resistance of Strand # 1 as function of time (left) and the resulting current distribution in Strand # 1 along its length during the quench of Case 1 (Figure 3.27a). The resistance (left) during the quench shows a plateau at 18 µΩ. The current over Strand # 1 (right) is compared between the numerical model (solid) versus the analytic equation (dotted) during the beginning of the prequench.

from Table 3.1 and Section 3.2.1, a dimensionless disturbance $\mathscr{R} = 10$ is found. The spatial distribution of the current found by the analytic model is shown in Figure 3.28b for corresponding time intervals by a dashed line.

The analytic model shows a good representation of the initial current redistribution (up to 10 ms), although small variations are visible. The amplitude at 1 ms varies, presumably due to the non-constant quench resistance of the normal zone for t<1 ms caused by the disturbance (Figure 3.28a). When the current redistribution spreads over the entire magnet length, the redistribution experiences inhomogeneous mutual coupling effects, causing asymmetric response. Since the neighbouring strand has reached T_{cs} at t =100 ms (Figure 3.27a), more complex effects due to the cable current redistributions arise and the analytic model starts to deviate.

Apart from the direct response to a strand quench, very limited gradients are visible in the current of over the strand's length, which indicates the absence of cable current redistribution. Complying to the conclusion of Section 3.2.4, the cable redistributions only contribute when sudden resistance unbalance between the strands arise. (i.e. $R_Q \gtrsim 1$)

3.3.6. VALIDATION

Due to the absence of empirical data, the model is validated by comparison with the existing HTS 3D quench model [9]. Both models are based on the single tape quench model, which was empirically validated in [21]. The single strand MQE of the 2 and 3D model are shown respectively in Figure 3.34a and Figure D.4. Validation of the cable model is performed by comparing two individual cases. These simulations for verification of the model included:

1. The mutual induction matrix derived from the 3D model [9] (Condensed matrix shown in Table G.2);
2. Identical superconductor model [52].

In the 3D model [9] a disturbance is applied on a corner node of the crossover, shown in Figure 3.29a. In the 2D model the crossover is approximated by applying the disturbance on the center tape of the stack, as shown in Figure 3.29b, while the disturbance acting on a single node in the 3D model is resembled by applying the energy on a single element in the 2D model.

The heat and current equations of a multi-strand cable form a coupled set of equations. In order to validate the two processes separately, two cases are studied. Case A only includes redistribution over the joint (Figure 3.7b), while Case B includes the current redistribution within the cable (Figure 3.7c).

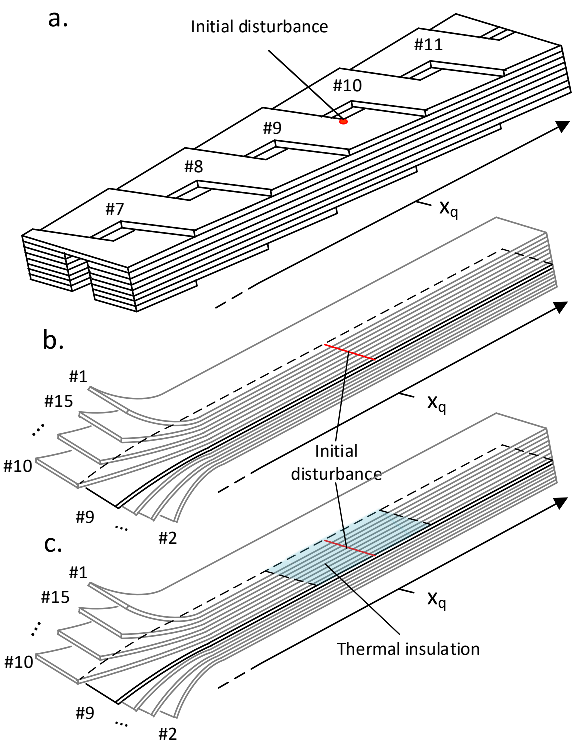

Figure 3.29: Schematic overview of cable modelling; a. 3D Roebel geometry with the initial disturbance of the 3D model located at the corner of the crossover, b. modelling approach in 2D model with disturbance at center strand, c. modified modelling approach to explain the asymmetry by implementing a thermal insulation of 2 cm at x_q (blue).

THERMAL MODEL WITH JOINT REDISTRIBUTION

The results of the simulation of Case A by the two models of the 15 strand quench model without current redistribution along the length of the cable are shown in Figure 3.31. The cable's current density J is 970 A mm^{-2} while it is perturbed by a disturbance energy E_h of 100 mJ during 100 ms. By comparing the behaviour, the following differences are noticed:

1. Difference in length of drift;
2. Time interval between quench of first two strands;
3. Asymmetric vs symmetric quench behaviour.

The agreement between both models is satisfactory, by taking the difference of modelling and complexity into account. The location of the initial quench disturbance and the geometry of the Roebel versus tape stack are expected to contribute to the discrepancy. Since the 3D model simulation applies the initial disturbance at the corner of the crossover, an asymmetric quench results. The opposite tape stack is not directly in contact with the hotspot (Figure 3.30), therefore Strand # 10 quenches significantly later than Strand # 8. In [9] more quench examples are found with disturbances inside the tape stack of the Roebel cable, approaching the symmetric quench behaviour represented by the 2D model.

The difference in drift length and the quench interval of the first strands are expected to be mainly caused by the implementation of the initial disturbance. The 3D model shows a steeper temperature rise following the disturbance of the first strand, causing the first strand to reach T_{cs} approximately 30 ms earlier. Since the disturbance power and energy are identical, the difference in temperature rise is expected to be caused by a difference in spatial distribution or implementation of the disturbance.

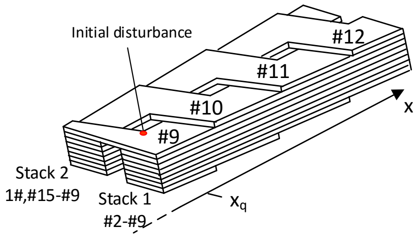

Figure 3.30: Roebel cable geometry and initial disturbance location causing asymmetric quench behaviour between the two tape stacks of the Roebel cable.

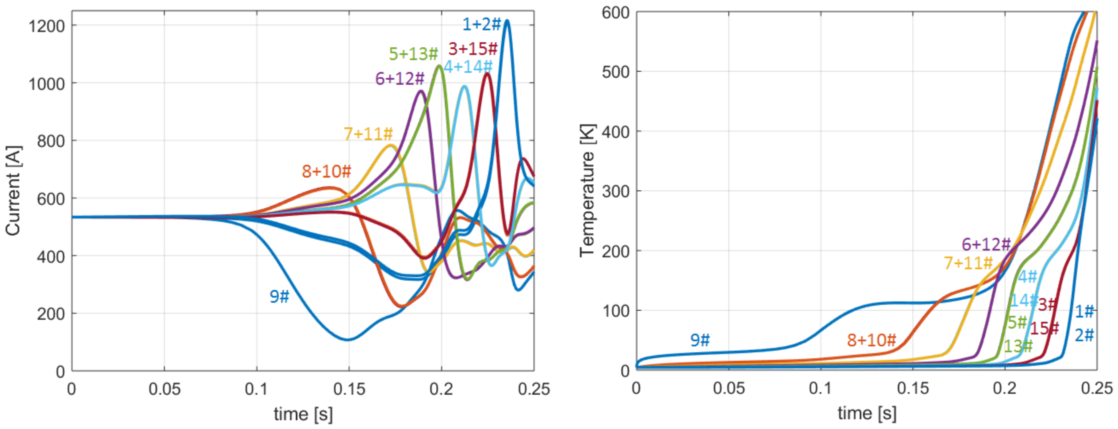

a. 2D Model without cable redistribution

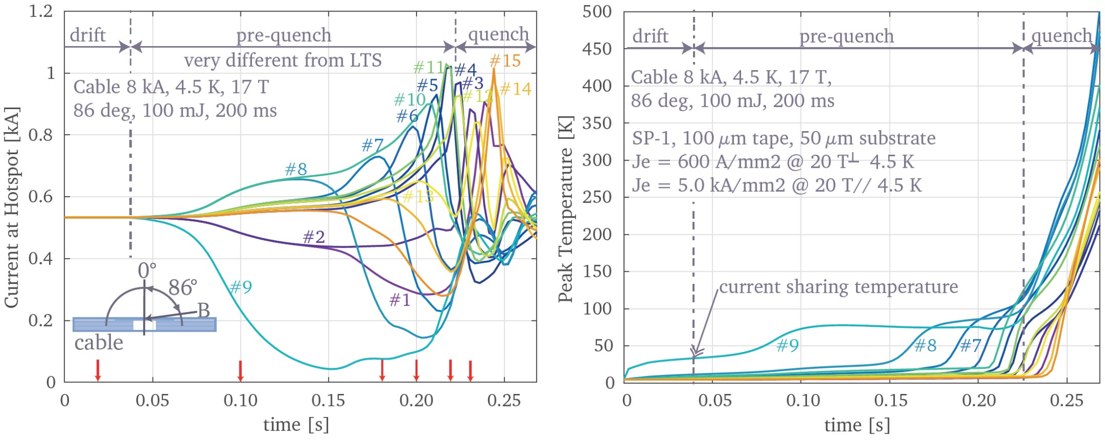

b. 3D cable model without cable redistribution [9]

Figure 3.31: Numerically found current distribution over the various strands in the cable (left) and the hotspot temperature of each strand (right) as function of time during Quench Case A. Comparison between numerical (a) 2D model and (b) 3D model [9] quench results *without* cable current redistribution at 8 kA, 4.5 K, $\alpha = 86^\circ$ 17 T, 100 mJ and 200 ms.

CABLE CURRENT REDISTRIBUTION

Following the validation of the thermal model in Case A, Case B includes the cable current redistribution in the simulations of both models. In the 3D model the local magnetic field within the quench region is calculated using MLFMM based on the current distribution throughout the whole magnet. In contrast to Case A, the magnetic field B and angle α of the 3D model are time dependent. Since the 2D model relies on a fixed background magnetic field, which is not quantified in [9], a 17 T field with 86° field angle was chosen to comply with Case A.

The models including the current redistribution within the cable are compared in Figure 3.32. Apart from the discrepancies seen in the previous comparison, a significant difference in time scale is observed. The discrepancy between both models is again presumably caused by the asymmetry of the cable geometry. In the 3D model, the affected strand (# 9) is situated at $x = x_q$ at the top of the cable, hence Strand # 10 is not instantly thermally affected by the hotspot since it is located at the other tape stack at the initial quench position $x = x_q$ (shown in Figure 3.30). The current can redistribute throughout the cable to this tape, while its temperature remains low and therefore maintains significant load margin. Strand # 10 acts as a temporary current buffer, which mitigates the development of the quench.

The asymmetry of the cable's geometry is expected to affect the outcome more significant compared to Case A, caused by:

1. Current redistribution within the cable to neighbouring strands, which was not included in the other simulation;
2. Faster current redistribution due to shorter disturbance pulse t_h causing more prominent inductive effects. Directly neighbouring strands have lower induction $L - M$, favouring redistribution.

The length x over which the Strand # 9 and # 10 are not in contact is found by (Figure 2.8):

$$dx_{\text{ins}} = \frac{\ell_{tp}}{n}, \tag{3.67}$$

with a twist pitch ℓ_{tp} of 300 mm and a cable consisting of 15 strands, a dx_{ins} of 20 mm is found. After applying this insulation boundary in the model between Strand # 9 and # 10 (Shown in Figure 3.29c) to approximate the cable geometry, the response in Figure 3.33 is found. An asymmetric response comparable to the 3D model is observed. The thermal insulation causes Strand # 10 to remain superconducting for a longer period and up to a higher current density. The asymmetry introduces extra stability, thereby extending the quench by approximately 80 ms.

The discrepancy between the models is not fully clarified by the cable geometry approximation efforts and the disturbance implementation, since a discrepancy in the quench duration and the peak current amplitudes remains. The tape geometry of the 2D model does not include thermal and electric contact between Strand 1 and 2, as shown in Figure 3.29c, hence an artificial boundary exists which contributes to the observed high current densities preceding full quench. Hence the 2D model is not capable capturing these asymmetries accurately. In addition, the higher currents and longer quench duration suggest a difference in stability between both models, which could be caused by the I_c and T_{cs} dependence of the unknown field strength and angle. Specifically a high sensitivity of I_c at high fields B to field angles α approaching 90 deg was observed in Figure 2.6b. An increased I_c results in an higher thermal stability of the cable, thereby increasing the quench duration.

The model attempts to capture the behaviour of the thermal instability near an equilibrium including the superconducting transition, hence small difference either in input or in modelling approach have large effects on the results. Since the cause of a quench is not known and is simplified for both models, the quantitative behaviour remains arbitrary, while the comparison of both models has provided evidence of the agreement of the qualitative behaviour. In the remaining of this chapter, the behaviour of the 2D model is therefore studied in more detail.

3.3.7. MQE

The stability of a superconductor can be quantified by the Minimum Quench Energy (or MQE), the minimum applied disturbance energy to cause a thermal runaway. By studying the MQE in different conditions, insight is gained in the complex quench mechanics of multi-strand cables. The MQE is found by iteratively simulating the model with varying disturbance energy amplitudes E_h. The cable is assumed to be quenched if:

1. all strands are fully normal conducting;
2. the hotspot reaches 500 K.

The MQE as function of the current density J is shown in Figure 3.34a for cables with a varying number of strands with a constant strand cross section. As been discussed in Section 3.3.4, the ability of the current to

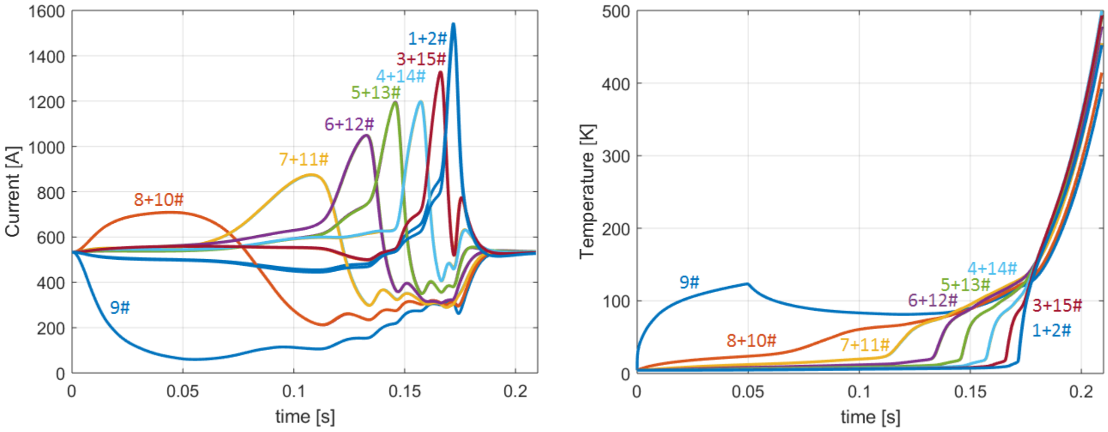

a. 2D Model with cable redistribution at $\alpha = 86°$ and 17 T

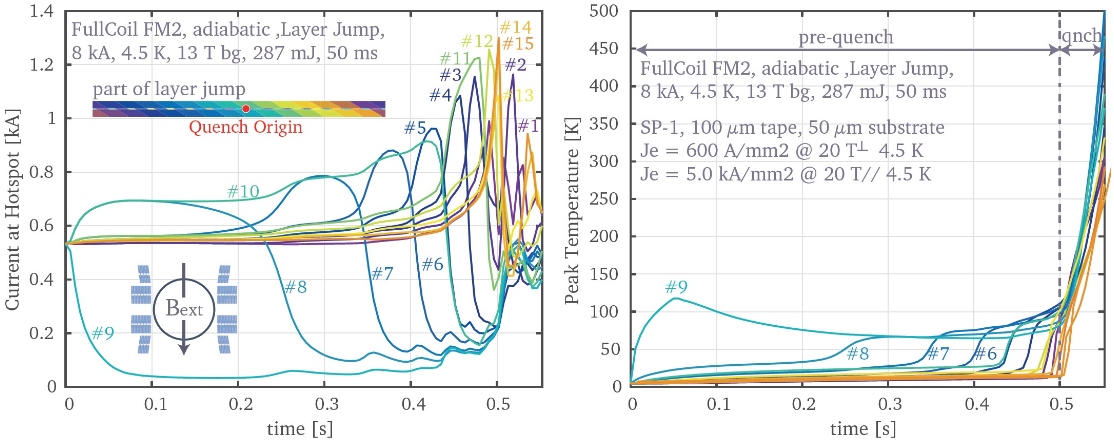

b. Full magnet 3D Model [9] with cable redistribution

Figure 3.32: Numerically found current distribution over the various strands in the cable (left) and the hotspot temperature of each strand (right) as function of time during Quench Case B. Comparison between numerical (a) 2D model and (b) 3D model quench results *with* cable redistribution [9] at 8 kA, 4.5 K, 287 mJ and 50 ms.

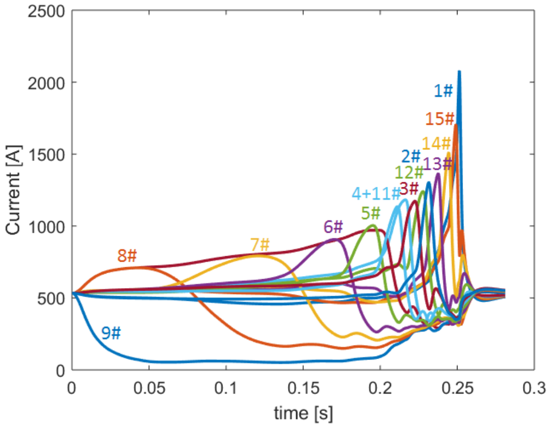

Figure 3.33: Numerically found current distribution over the strands with identical conditions as Case B (Figure 3.32), including a simplified cable geometry by introducing a 2 cm thermal boundary between Strand # 9 and # 10, as shown in Figure 3.29c.

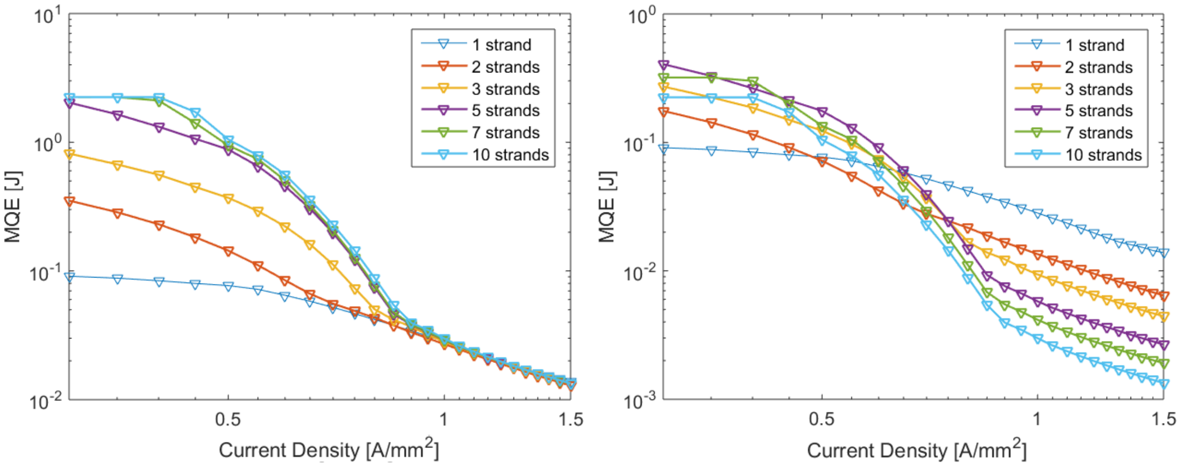

a. Constant strand cross-section; **b.** Constant cable cross-section.

Figure 3.34: Numerically found MQE as function of current density for cables with varying n strands at 4.5K, 17T. a. A tape with constant cross-section is added to the cable, hence the total cross sectional area increases proportional with the number of strands. b. The total cable cross is kept constant, while multiple geometries are assessed. Increasing the number of strands results in decreasing strand cross sectional area's.

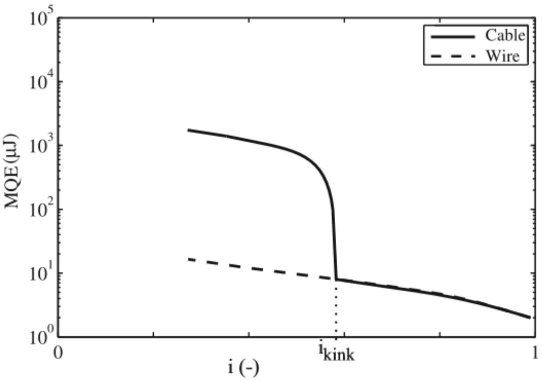

Figure 3.35: Illustration of the MQE as function of a dimensionless $i = J/J_c$ observed in LTS [34], showing the current dependence of superconducting cables . At low current densities ($J < J_{kink}$) the ability for current redistribution increases the MQE with respect to a single tape, while this higher stability vanishes for current densities $J > J_{kink}$.

redistribute results in a significantly higher stability of a multi-strand cable compared to a single strand at low current density J. The cable can stabilize after an individual strand has quenched by current redistribution to the other strands. Therefore this operating domain is called the current redistribution domain in which the MQE increases with the number of strands.

At high current densities, a strand reaching T_{cs} causes the quench of the entire cable, as been shown in Case 2 (Figure 3.27b). The MQE in this operating domain is governed by the stability of individual strands, therefore called the single strand regime [34]. The MQE performance of multi strand cables is thereby drastically reduced for higher current densities J. The transition between both regions is defined as J_{kink}, which divides the MQE in a redistribution and single strand regime, as shown in Figure 3.35. Note the J_{kink} is only a fraction of the critical current J_c found in Table 3.3.

For cable's with more than 5 strands and low current densities (<500 A mm^{-2}), the MQE is limited due to the thermal contact resistance between strands and the nature of the applied disturbance. Strand # 1 is heated above 500 K dominantly by the disturbance itself, therefore virtually no current dependence is visible. Hence this region is therefore governed by the heat balance and not of interest for this study.

In the redistribution regime of 5 to 10 strand cables a stepwise behaviour at $J = 500\,\mathrm{A\,mm^{-2}}$ is observed. This behaviour was also observed in Rutherfort LTS cables by [34]. It is caused by the different redistribution mechanisms, which have varying inductive loads:

1. At low current density, the current can redistribute to the outer strands which are not affected by heat diffusing from the hotspot, resulting in higher MQE
2. At higher current densities, the redistribution is limited to the direct neighbouring strands by induction. These strands are directly affected by the heat diffusion from the hotspot, hence the MQE is smaller.

The different regimes were experimentally validated in Nb-Ti Rutherford cables. Although the qualitative MQE behaviour is similar for LTS and HTS, the found stability values differ 2 to 3 orders of magnitude compared to [34] (shown in Figure 3.35).

The stability of a cable with constant cross section and a varying number of strands is shown Figure 3.34b. At lower current, the MQE increases with the number of strands, since the quench is driven by the diffusion of the initial disturbance. The strands are only thermally in contact with 2 fixed neighbours, while the current can redistribute over the joint to all strands. Each strand forms a thermal barrier, preventing the heat to reach the outer strand(s). Therefore limiting their temperature increase, resulting in a locally higher critical current density J_c, which facilitates the ability for current redistribution. More strands therefore result in an higher thermal diffusion barrier with a higher MQE as result.

The strand's cross section decreases in this case with the number of strands. Since cable's stability in the single strand regime is determined by the performance of a single strand, the MQE scales inversely with the number of strands at high current densities ($J > J_{kink}$). Although a cable with many strands maybe electrically favourable with respect to screening currents, it decreases thermal stability in the single strand regime.

3.3.8. SENSITIVITY

Apart from current density and number of strands, other parameters such as cable, magnet and disturbance properties are of interest within the study of HTS cable quench stability. Uncertainty in the model can not be fully resolved, since model inputs such as the disturbance and contact interface properties are practically challenging to quantify. The input parameters used during the simulation are based on values found in literature. However, the inputs can show significant variations, caused by external factors which can be only marginally controlled, such as the cable manufacturing and winding conditions. These variables have unavoidable uncertainties which could exceed an order of magnitude [37], therefore qualitative understanding of the system's response to these parameters is required. Furthermore, the sensitivity offers understanding of the stability of existing magnets or in decision making for future magnet designs. The macro geometry of the magnet captured in matrix **M** and contact interface parameters are of special interest.

Although this model is only validated to single tape empirical data, it can offer valuable insight in the qualitative behaviour of superconducting cables. Emperical validation of MQE has proven to be challenging in single tape, since disturbance and cooling conditions during experiments are ill-defined [21]. Experimental quantitative determination of MQE in HTS cables will be even more challenging, due to the increase in degrees of freedom and the number of contact interfaces.

The model aims for qualitative understanding of HTS quench by gaining insight in the model's response to these uncertainties. The behaviour of J_{kink} is of special interest, as a key parameter in the cable's stability. Since the computation of MQE is a very expensive procedure, instead of modelling 15 strands with symmetric quench (Figure 3.29b), the model is reduced to asymmetric 8 strands (Figure 3.26). In Figure 3.36 the MQE of the two models are compared. Although the MQE quantitatively differ by more than a factor 2, the behaviour is believed to be analogous, due to the electric and thermal network symmetry (Figure 3.12). The influence on the stability of several cable and coil properties are discussed below. The variation of the the joint resistance and the quench location are left to Appendix D.

INITIAL DISTURBANCE

Quench causes have already been discussed in the first section of this chapter. Since the causes remain unknown, it is impossible to quantify the initial perturbation to the system. Therefore their spatial and temporal

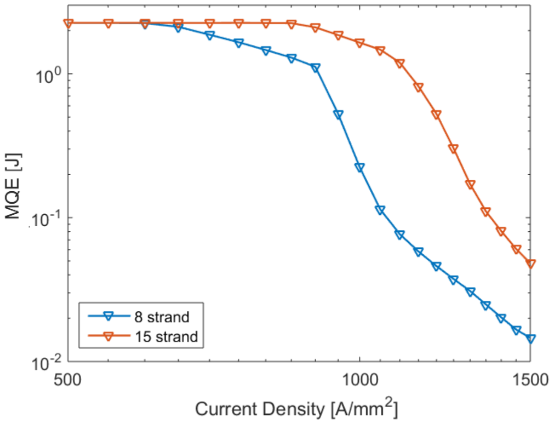

Figure 3.36: Numerically found MQE versus current density J for an asymmetric 8 and a symmetric 15 strand quench at 17 T, 4.2 K.

distributions are ill-defined. In order to study the system's stability under influence of varying disturbances, the sensitivity with respect to disturbance pulse length and duration are studied.

The MQE as function of the current density J for various pulse lengths ℓ_h is shown in Figure 3.37a. For small length's at low current densities the sensitivity is small up to 2 cm, since the quench develops slowly and allows the heat to diffuse. The initial disturbance length is therefore only of minor influence when considering local disturbances (i.e. <2 cm). At high currents, longer disturbance lengths cause less concentrated hot spots, therefore requiring more energy to locally reach T_{cs} to initiate the quench. The found MQE is therefore larger for higher ℓ_h.

The MQE as function of current density J for various disturbance durations is shown in Figure 3.37b. Analogous to the disturbance length, at low currents the longer quench duration allows the disturbance energy to diffuse over the length. The MQE is therefore nearly invariant of the disturbance duration. At higher currents the MQE increases for longer t_h. The energy required for the hotspot to reach T_{cs} increases with the duration of the disturbance, since a longer disturbance duration causes longitudinal heat diffusion over the conductor's length. Analogous to ℓ_h, the decreased locality of the hotspot results in longer lengths of the strand heated by the disturbance, resulting in a higher MQE. At disturbance lengths 5 cm and 10 cm, no clear J_{kink} is visible any more. Hence, the single strand regime is only existing for local disturbances.

Both disturbance length and time are related by the diffusion of heat. The ability of the heat to diffuse and the current to redistribute increases the overall stability. The transition between the single strand and redistribution regime gets less pronounced while the overall MQE increases with a more gradual and evenly spread disturbance, since larger area's of the cable are affected. Hence, especially at high current density, the cable is significantly more sensitive to local high power disturbances with constant E_h.

ELECTRICAL CONTACT RESISTANCE

The interstrand resistivity r defines the ability of the current to redistribute within the cable. A high contact resistance restrains this ability and forces the current to redistribute over the joints. As has been discussed in Section 3.2.3, restraining the current redistribution causes increased ohmic heating in the normal zone, reducing the stability. The MQE for various contact resistivity values is shown in Figure 3.38a.

The numerical model shows an overall increase in the MQE for lower interstrand resistances over the full current density range. The enhanced ability to redistribute within the cable increases the MQE significantly. The lower contact resistance causes the redistribution to contribute up to higher current densities, thereby increasing J_{kink}. At very low interstrand resistances ($2.88 \cdot 10^{-8} \Omega\text{m}^2$), the ability to redistribute increases the stability even in the single strand regime.

Interstrand contact resistance shows a clear influence on the stability of the cable. Lower contact resistances stimulate current redistributions within the cable. Hence, the current in the quenched strand can decay faster, resulting in less ohmic heating which enhances the cable's stability.

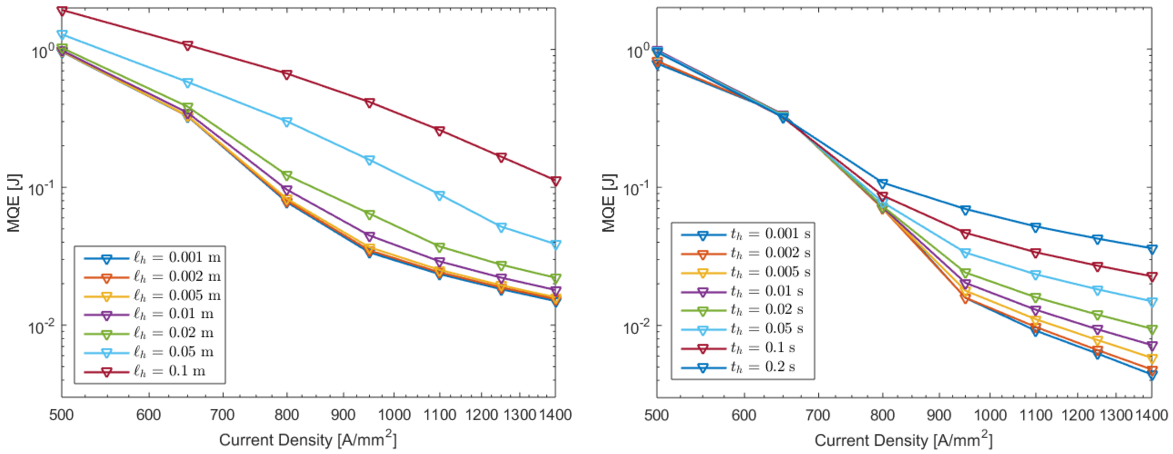

a. Pulse length sensitivity.

b. Pulse time sensitivity;

Figure 3.37: Numerically found MQE versus current density for varying pulse lengths and durations. Within this studies, t_h=50 ms and l_h =1 mm are used.

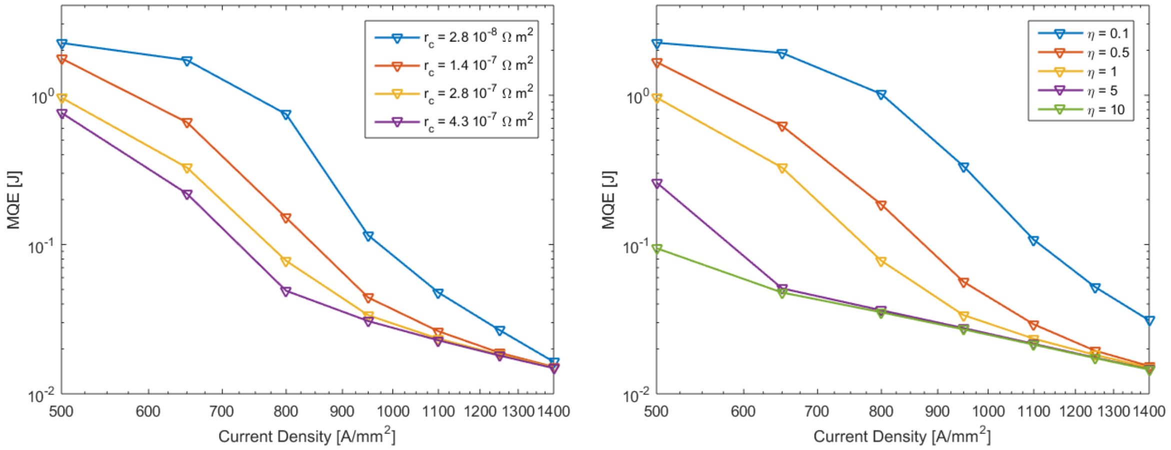

a. Electric interstrand contact resistance $r_c = r\,w$;

b. Feather M2 induction matrix scaling by η.

Figure 3.38: Numerically found MQE versus current density for several electric strand contact resistivities (left) and induction values (right). Within this studies, $r_c = 2.8810^{-7}\Omega\mathrm{m}^2$ is used [38](left), while the Feather M2 induction matrix is scaled by the the factor η shown in the legend (right).

COIL INDUCTANCE

The conductor's induction is defined by the magnet and cable geometry and governs the ability of the current to redistribute. Within this parameter study the mutual inductance matrix of Feather M2 is scaled by factor η. The MQE as function of current density for various induction scaling factors η is shown in Figure 3.38b.

For low inductive values the current redistribution regime is significantly increased. Lower inductance causes easier current redistribution, thereby reducing the ohmic heat dissipated in the normal zone. Increasing the inductance decreases the ability to redistribute and thereby the transition current J_{kink}. At high inductive values the current redistribution is restrained to a single strand. Hence the cable's stability is again determined by a single strand and a MQE similar to a single strand shown in Figure 3.34a is found.

By studying the MQE dependence of the inductance and the interstrand resistivity, it is observed that the scaling of both parameters show a similar effect. Hence, the following scaling of the MQE is observed:

$$MQE \sim f(r\eta)\,. \tag{3.68}$$

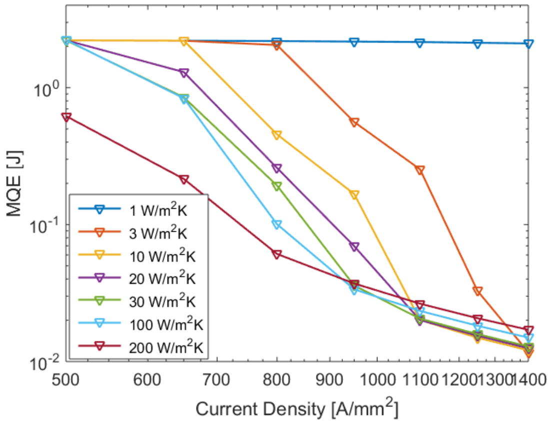

Figure 3.39: Numerically found MQE versus current density for several thermal strand contact conductivities. Within this studies, k_c =100 $\mathrm{W\,m^{-2}\,K^{-1}}$ is used [37].

which complies with the time constant found for the simplified analytical cable current redistribution of Equation 3.41. However, the relation between stability and the ability for the current to redistribute is likely to be more complex. The system's response with respect to these parameters is only qualitatively known and is likely to be more complex. For a better comparison of the MQE dependence of contact resistance and induction, the sweep of resistance and induction are shown together in Figure D.3.

THERMAL CONTACT RESISTANCE

The sensitivity of the model to thermal contact conductivity between the strands is shown in Figure 3.39. The thermal conductivity is an important parameter, since it defines the ability of the hotspot to affect the neighbouring strands.

At low thermal conductivity values ($\sim$ 1 $\mathrm{W\,m^{-2}\,K^{-1}}$), the MQE is high and barely dependent of the current density. The initial disturbance cannot diffuse to the other strands, therefore a similar behaviour as been seen in Figure 3.34a for cable with a 5 to 10 of strands at low current densities (<500 $\mathrm{A\,mm^{-2}}$) is found. The perturbed strand is driven over the limit of 500 K, while the ohmic heating barely plays a role. The behaviour is therefore governed by the heat balance and is nearly independent of the current density J.

At higher thermal conductivities the transition is visible (3-100 $\mathrm{W\,m^{-2}\,K^{-1}}$), while the transition current J_{kink} decreases with higher thermal conductivities. The current regime reduces, since the heat is spread more easily throughout the cable. The cable is therefore less resilient to a local hotspot in a single strand and the ability for the current to redistribute reduces.

At high thermal conductivities ($\sim$ 200 $\mathrm{W\,m^{-2}\,K^{-1}}$), the current sharing regime vanishes, while an increased stability at higher current densities J is found. When the disturbance heat spreads transversely over the strands, more energy is required to reach locally T_{cs} to initiate the quench.

3.3.9. CONCLUSIONS

The stability of the High Temperature Superconductor multi-strand cables is governed by the coupling between thermo- and electrodynamics. The MQE as function of current shows a clear transition between two regimes divided by a current J_{kink} (Figure 3.35):

1. Current sharing regime, wherein the stability is governed by the ability of the heat to transverse over the cross-section and affect the remaining superconducting strands;
2. Single strand regime, in which the stability is defined by the performance of a single strand.

Apart from the current density, various other magnet and cable parameters have been identified to affect this transition, which are summarized in Table 3.8. The main conclusions drawn from the parameter sweeps are as follows:

	I_{kink}	Cable regime	Strand regime	
n	$+^*$	+	-	Number of tapes (constant cable cross-section)
n	+	+	0	Number of tapes (constant strand cross-section)
t_h	+	+	+	Duration disturbance
ℓ_h	+	+	+	Spatial length disturbance
k_c	-	-	+	Thermal contact conductivity between strands
r_c	-	-	-	Electrical resistance between strands
R_j	-	-	-	Joint resistance
$\|x-\ell/2\|$	-	+	0	Distance of quench to center of the coil

Table 3.8: Summary of MQE dependencies when specified parameter increases.

1. A relation between the induction scaling η and the contact resistance r was observed, analogous to the relation of the interstrand current redistribution in Equation 3.41;
2. A cable consisting of multiple strands has a higher stability at lower currents (current redistribution regime) and a lower stability at higher currents (single strand regime) compared to a single strand with identical cable cross-section;
3. The reduced stability in single strand regime is only observed for local (ℓ_h <5 cm for t_h =50 ms) and abrupt (t_h<1 s for ℓ_h =1 mm) disturbances;
4. Increasing the ability for the current to redistribute (e.g. lower r,L,R_j) increases the MQE, while increasing the transverse thermal conductivity (i.e. k_c) lowers the stability.
5. The stability reduces when a quench occurs near the center of the coil (confirming analytic result of Figure 3.17).

Hence increasing the thermal stability of a HTS magnet design operating at high current densities requires minimizing the number of strands (assuming constant cable cross section) together with low inter-strand induction, contact resistance and thermally conductivity.

3.3.10. DISCUSSION

The qualitative stability behaviour of a HTS cable shows agreement with the 3D Model [9] and LTS modelling and experiments [34], such as the transition between the single strand and current sharing regime. Although the model is drastically simplified, it gives a reasonable representation together with high computation efficiency. Depending on the operation regime and model parameters, simulations by the 2D model of 8 strand cable quench events are performed within several minutes, which is a significant gain compared to the 3D model [9]. Nevertheless, the 2D model does not offer the full range 3D modelling capabilities, such as magnetization simulations.

Validation of the model remains challenging due to the nature of the modelled quench phenomena. Since the model describes the behaviour of an instability, small variations in input and simulation methods have significant impact on the result. By deliberately keeping the model's complexity to a minimum, apart from the gain in efficiency, also the generality of the qualitative behaviour was demonstrated.

By comparing the analytical current redistribution and the numerical model, the results of both models agreed under controlled circumstances. Analytic solutions only exist for a limited number of cases, including constant quench resistance in the centre of the coil. The spatial current distribution predicted by the analytic model has shown satisfying agreement with the initial current redistribution behaviour found during the symmetric quench case at low current and short disturbance pulse duration. Larger discrepancies are expected in other cases, nevertheless the underlying current redistribution mechanism is expected to remain unchanged.

Based on the observed scaling of the MQE behaviour with respect to the induction and interstrand resistance, a promising resemblance with respect to time constant Equation 3.41 was found. Although the results seem encouraging, the observation was solely based on the MQE behaviour for several parameter values. Understanding of the relation between stability and current redistribution requires profound study of the dependency in spatial and time domain.

Within the parameter sweeps the sensitivity of the model has been explored for several parameters. The model's response confirmed the expectations based on insights gained from the analytic models. During the sweeps no drastic change in behaviour was observed, therefore the qualitative behaviour is expected to appear in Feather M0 and Feather M2. Although a selection of parameters has been evaluated, several other parameters including the operating conditions could be of interest for future study.

Although the recommended measures for HTS magnet design favour the theoretical thermal stability of the magnet, practical implementation is not trivial. Since for example electrons facilitate both thermal and electric conduction, practical implementation of high thermal conductivity and low electrical resistivity will result in a compromise between both parameters. Apart from the stability itself, another compromise is required between the magnet's stability and the ability to detect, which is the subject of the next chapter.

4

DETECTION AND PROTECTION

In the previous chapter a valuable insight on the thermal and electric behaviour of a superconducting cable was gained with both analytical and numerical models. In this chapter this insight will be applied for assessing different kinds of quench detection. The main challenge in finding a suitable quench detection system is the required reliability, as a system or a combination of systems has to guarantee that any occurring quench is detected in order to trigger protective action. The quench detection is put to test during magnet operation, which includes challenging conditions including high stress regions, limited space, cryogenic temperatures and strong electromagnetic fields. Since detection is accompanied by protection, this chapter starts by regarding protection considerations in general. This study is followed by the possible sensors one can apply together with a proposal for a novel HTS quench detection system. The final section considers how the system detects a quench based on sensor signals.

Within the field of LTS quench, many different detection methods have been attempted in the past, either established for protection in various applications or for the purpose of research. Due to the thermal instability, LTS magnets quench at disturbance sources less than a millijoule, making quench in an LTS magnet's lifetime inevitable (See Section 3.1)[18]. Detection is therefore of great concern in the design and operation of a LTS magnet. HTS magnets are typically operated at 70% of their loadline, resulting in high stability margins [20]. Due to this stability, the normal zone propagates slowly through the material (Figure 3.5), decreasing the performance of conventional LTS voltage detection, as been shown already in Figure 1.3. Although HTS materials are very stable, the consequences of thermal runaway pose a risk for any application, which underlines the need for adequate protection.

4.1. QUENCH PROTECTION

Quench protection can be divided roughly into active and passive protection. Active protection requires an external trigger (i.e. detection) after which a direct action is executed, while passive protection offers stability from cable composition and magnet geometry [18].

Stability and detection, although both indispensable in high field applications, are two conflicting concepts. Since detection (and active protection) require(s) time to intervene, the magnet needs sufficient stability to mitigate the runaway before the active measures take effect. In addition, the magnet should be able to withstand the inevitable disturbances up to a certain level, to assure stable operation for longer periods of time. Each quench is a potential hazard for its integrity even with decent protection measures in place and results in interruptions of its operation.

The consequence of passive protection is a reduction of the current density in the superconductor J. Superconducting materials can carry high current densities during operation, up to $4\,\mathrm{MA\,cm^{-2}}$[54]. Hence, significant thermal loads arise after a sudden gain in resistance when entering normal conduction, which can be up to a few orders of magnitude higher compared to standard conductors such as copper[18]. To ease this effect, copper (or aluminium) is added to the cross-section of the tape or cable, as shown for ReBCO tape in Figure 2.7. Apart from redirecting the current, these stabilizers diffuse the generated heat over the cable length by enhancing the thermal conductivity, which leads to faster normal zone propagation (See Equation 3.4). Nevertheless, adding stabilizer reduces the ’fill factor’, the portion of superconductor in the cable cross-section, and thereby the critical current density of the cable, compromising its performance. Additionally, since the soothing effects of stabilization causes less abrupt runaway, it results in less pronounced signals and complicates quench detection.

Aside from stabalizers, stability can be enhanced by non-insulating coil winding [55], which allows the current to pass by a normal zone via adjacent winding turns. The enhanched stability is similar to the observed dependence of the MQE as function of the electric inter strand resistance in Section 3.3.8. Disadvantage of non-insulated cable windings is the limited control of current during nominal operation, which could deteriorate the field quality [56].

Cryostable LTS magnets exist with the ability to regain its superconductor state after quenching without the need of intervention. Although these magnets reduce the protection complexity, practice learns that cryo-stability is at great expense of performance (Reduced critical current density J_c) [18]. Thereby, since the causes of a HTS quench are yet uncharted, it complicates quantifying the cryo-stability a magnet needs for its operation. Especially due to the cost of HTS material at present, commercial applications are likely to be very demanding in terms of performance (i.e. current density J), reliability and lifetime. To make HTS competitive, stability should be sufficient to allow a good operational margin, while detection ensures safe operation with high reliability. Therefore, a practical accelerator magnet requires both active and passive measures for an adequate protection.

To validate if the quench detection is offering sufficient protection, one should consider the detection and protection sequence as a whole. To get a understanding of the of the entire protection sequence, a quick outline is given, while several components are considered in more detail in this chapter. The protection of a superconducting magnet consists of [19]:

1. Detection of unusual behaviour by the sensor;
2. Amplification and filtering;
3. Quench identification by a detection algorithm;
4. Power supply switch off;
5. Magnetic energy dissipation.

Detection starts by identifying unusual behaviour by monitoring the state of the magnet and its surroundings. Quench sensors are operating in harsh electromagnetic environments and their analogue signals are generally small, making them susceptible for noise. Therefore, signals require filtering and amplification before detection can be performed. After the signals have been processed, the signal is fed into a detection algorithm. Analogue detection algorithms for LTS magnets compare signals with pre-set thresholds over a certain time window. When a quench is detected the appropriate protection measures are triggered (See Section 5.2.1).

Protection measures include immediate power supply interruption to limit the ohmic heating in the normal zone. Solid state devices, such as thyristors, are generally used for their speed, while mechanical relais are placed in series for redundancy. Thryristors can switch high currents within milliseconds, while mechanical relais generally take 500 ms to 1 s to change state [20]. The ohmic heating in the normal zone continues while the power supply is still running, resulting in rising hotspot temperatures and threatening the magnet’s integrity.

Part of the stored magnetic energy remains in the magnet after the current supply has been switched off and has to be dumped. For magnets with low stored energy $\ll$ 1 MJ) such as Feather M0 and Feather M2, the magnetic energy is limited and can be gradually dissipated inside the normal zone by connecting the magnet in persistent mode. For magnets with high stored energy full dissipation within the normal zone is poses too high thermal loads and therefore the energy should be dumped externally or dissipated over the whole coil. The magnetic energy in the coil is given by [20]:

$$E_{mag} = \frac{1}{2} L I_{op}^2 . \tag{4.1}$$

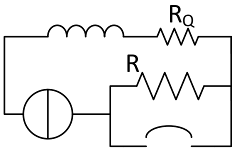

Figure 4.1: Schematic overview of dump resistor circuit. In nominal operation the switch is closed as shown in Figure 3.6. When a quench R_Q is detected, the switch is opened and the current will dissipate inside the dump resistor R.

The stored magnetic energies of Feather M0 and M2 are respectively 1.3 kJ and 15 kJ at 8 kA, which can be dumped in an external resistor placed in series with the magnet, as shown in Figure 4.1. To limit the amount of energy dissipated in the normal zone and to enhance the ramp down speed, the resistance of the dump should be orders of magnitude higher than the normal zone resistance. The resistance is however limited by the maximum allowable voltage over the magnet's leads for safety reasons [18]. Another possibility is to make the magnet itself resistive by stimulating the normal zone growth. If the magnetic energy (Equation 4.1) is spread adiabatically over the whole conductor length of Feather M0 and M2, it will cause a temperature increase by respectively 15 K and 36 K, which is well within the allowable temperature limits. Special quench heaters can be used to quench the magnet along its length, thereby spreading out the magnetic stored energy over the entire coil. Although it requires no extra components such as dump resistors, an internal dump in the magnet suffers longer down time following a quench due to the warm-up of the cryostat.

Protection and detection of a superconducting magnet form an interdependent chain of events, which should be taken into consideration in the early phase of the magnet design. For a more in depth description of general quench protection and the protection of the LHC, the interested reader is referred to [2] [18] [20] [35]. The protection intervention of Feather M0 and Feather M2 takes approximately 5 ms for the protection electronics to activate and 25 ms for the protection measures to take effect. The total time budget required for adequate intervention is therefore approximately 30 ms [57]. With this required specification, the remainder of the chapter will discuss various quench detection methods regarding the protection of Feather M2.

4.2. EXISTING QUENCH MEASUREMENT PRINCIPLES

Quench is a coupled thermal electromagnetic phenomenon, enabling different approaches to recognize its occurrence. However, due to the large operating domain of HTS superconductors, HTS quench has multiple appearances as shown in Chapter 3. Since there is not yet a single exhaustive solution for detection, multiple potential measurement principles are reviewed.

4.2.1. TEMPERATURE

Quench is in essence a thermal runaway, therefore one could consider using temperature sensors for detection of temperature changes. A temperature rise near the conductor is a distinct sign for abnormal operation conditions. To explore the ability of temperature sensors to detect the quench, the heat diffusion is studied to gain insight in the thermal phenomena. Due to the locality of HTS quench, precise temperature measurement with high resolution is required. To illustrate the necessity of fine granularity, the adiabatic longitudinal temperature of the conductor is analysed. The temperature of the superconductor is approximated by Equation 3.3, which describes the temperature of the superconductor of a single tape quench [20]. In an ideal situation it would be possible to measure the exact temperature of the conductor. Hence, rewriting this expression to x and assuming the quench occurs in between two sensors $\Delta x = 2x$ and $\Delta T = T_s - T_{op}$, we obtain:

$$\Delta x(\Delta T, t_{det}) = \underbrace{2V_{nz}t_{det}}_{\text{Normal front}} - \underbrace{\frac{2k_s}{C_s V_{nz}}}_{\text{Thermal path}} \underbrace{\ln\frac{\Delta T}{T_t - T_{op}}}_{\text{Sensitivity}}, \tag{4.2}$$

Δx [mm]	t_{det} [ms]	
ΔT	50	100
0.01	24	34
0.001	28	38

Table 4.1: Required spacing Δx for temperature quench detection for various detection times t_{det} and sensor sensitivities ΔT assuming ideal conductor temperature measurement.

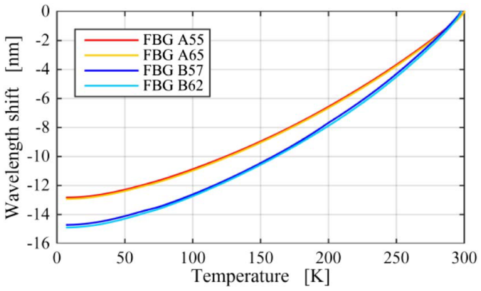

Figure 4.2: Measured wavelength shift versus temperature of a optical fibre showing the sensitivity of FBG-sensors [58]. B-type sensors are used for the Feather M0.4 test (Chapter 5).

with the temperature detection threshold ΔT and the sensor spacing Δx. In Table 4.1 the required sensor spacing is shown for various detection times t_{det}, using the parameters of Section 3.2.1 and assuming a normal zone propagation of $0.1\,\mathrm{m\,s^{-1}}$ (Figure 3.5). A low gain in Δx with respect to the sensor sensitivity is observed, which is caused by the steep temperature gradients at the transition zone. The required sensor granularity in this ideal case can be already problematic, especially for full scale magnets and conventional temperature sensors. In reality the temperature of the conductor can not be measured directly, imposing even higher demands on the required sensor spacing Δx.

The locality of the normal zone poses strict requirements for direct measurement of the hotspot, demanding positioning of the sensor in the vicinity of the cable and fine granularities (Table 4.1). Two examples of non-conventional thermal sensors are presented which have the potential to serve as quench detection sensor.

OPTIC FIBRES

Optical fibres can measure strain and temperature effects along the fibre with a spectrometer. In Fiber Bragg Grating or FBG sensors, a periodic modulation pattern is etched on the fibre by exposing it to UV-light. This pattern reflects only light with a specific wavelength corresponding to the spacing of this pattern. If the sensor is under strain near the pattern, the spacing of the pattern changes slightly. When broadband frequency light is passed through the fibre, the change in pattern causes a different wavelength to be reflected, which can be recognized by the spectrometer. Temperature causes thermal strain of the fibre glass material, but its sensitivity is lost at temperatures below 80 K. To enhance its sensitivity epoxy or polymer coatings are used with reported sensitivity down to 20 K [58], as shown in Figure 4.2.

If the fibre is fixed to the magnet it measures a combination of its own thermal strain and the strain of the host material. In order to measure solely the expansion of the fibre itself, it is placed inside a thin metal tube. The fibre can expand and/or contract stress-free due to temperature changes, while it remains in thermal contact with the base material.[59]

Since these fibres operate with an optical signal they remain insensitive to electromagnetic noise. Optic fibres have small dimension and can attain high temperature sensitivity (mK) [60]. No electric insulation between the fibre and conductor is needed, reducing the thermal barrier and increasing its sensitivity [59]. The fragility of the fibre can pose challenges in its application, especially in high field magnet applications due to the large affiliated mechanical stresses.

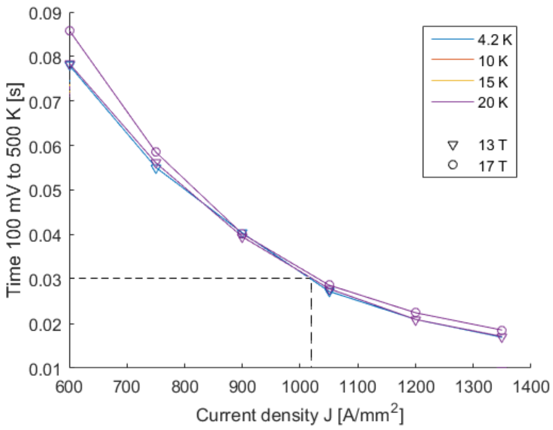

Figure 4.3: Feather M2 time between 100 mV signal and the hotspot reaches 500 K versus current density J for various magnetic fields and operating temperatures. The figure gives an indication of the intervention time required for voltage detection.

LTS WIRE

At low temperatures (<8 K for $Nb-Ti$, <18 K for Nb_3Sn) and low fields (<3 T) [61], a co-wound LTS wire can be used as quench detection [62]. A small current is fed through the wire while the voltage is monitored. Since low temperature superconductors have a low MQE and a sharp transition from superconducting to normal state, this type of sensor could be able to detect a temperature difference during the drift[63]. The wire can be co-wounded with the cable to minimize the thermal path, for example by placing it inside the midgap of the Roebel cable (Figure 2.9). For optimal performance the thermal conductivity to the cables should be high while insulating the sensor electrically to avoid that the measurement current leaves the LTS wire.

For low temperature HTS applications this could be a suitable candidate for quench detection, because of its high sensitivity to very local temperature variations. $Ni-Ti$ is the most viable candidate, since it is a ductile material with high tensile strength and therefore ideal for co-winding. The maximum magnetic field of $Ni-Ti$ is however limited by a critical field B_c of 10 T and T_c of 9.2 K. The use of this type is therefore limited by maximum reachable field limitation and operation temperature, which has to lie well below the B_c and T_c of the LTS material.

4.2.2. VOLTAGE

Voltage detection is the standard in LTS quench detection applications, including detection for the LHC [35] [64]. The abnormal behaviour is detected by measuring a rise in voltage resulting from the resistance of the normal zone (Equation 3.11). Since the normal zone of LTS materials grows rapidly, the quickly growing quench resistance generates large ohmic heating and high hotspot temperatures, requiring fast detection. Analogue quench detection systems with detection thresholds in the order of 100 mV is used, which are discussed in Section 5.2.1.

To asses existing voltage detection for HTS cable applications, the time between a measurable voltage (100 mV) and permanent damage (500 K) is calculated using the numerical model of Section 3.3. This interval is calculated for various magnetic fields and temperatures as function of the current density, as shown in Figure 4.3. Although a small magnetic field dependence is visible, it clearly shows voltage detection does not allow sufficient intervention time (30 ms) for current densities J exceeding 1000 A mm^{-2}. Note that the time the algorithm takes to identify the quench is not yet included. Therefore additional measures are required in order to detect a quench in an earlier stage.

The voltage measured over the magnet consists of an inductive and a resistive part (Equation 3.6). As shown in Equation 3.18, the resistive voltage over the normal zone is largely compensated by its inductive counterpart in multi-strand cables. Since the conventional 100 mV offers insufficient intervention time, the quench should be detected in an earlier stage. In an attempt to increase the signal, several measures to reduce the inductive effects are evaluated.

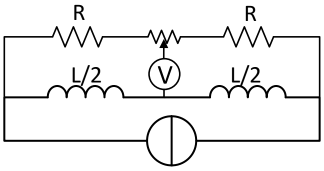

Figure 4.4: Schematic overview of balanced bridge [18] with high power (Thick lines) and voltage detection circuit (Thin lines). By substracting the voltages of two similar coil segments, the inductive compensation can be reduced. The potentiometer is used to adjust (small) inductive inequalities between the segments.

INDUCTIVE VOLTAGE REDUCTION

Inductive voltages can have different causes, including:

1. Ramp up of the magnet;
2. Current redistributions within the cable;
3. Inductive background noise.

In order to reduce the inductive effects, three types of measures can be taken: Balanced bridge, co wound sensor, and segmented voltage measurement. By co-winding the sensor wire with the superconductor cable the inductive noise caused by electromagnetic fields is minimized. [65].

A balanced bridge circuit can be used to compare two similar segments or poles of a magnet, as shown in Figure 4.4 [18]. Since the segments have similar geometry and are placed electrically in series, their inductive behaviour is comparable. An imbalance of voltage between the two sections indicates a possible quench occurring. Extra care should be taken for symmetrical quenches, which can remain undetected when using balanced bridges [18]. For redundancy an additional quench detection system should be operated in parallel for monitoring the individual segments [35] [18].

As discussed in Chapter 3, a voltage can be troublesome to measure during the prequench in a HTS multistrand cable, due to inductive compensation effects following from current redistributions (Equation 3.18). Inductive voltage can be reduced by measuring at multiple positions along the strand, as shown in Figure 4.5, since the voltage of the quenched segment (V_{23}) distinguishes itself from the other segments [18]. A disadvantage of applying the segmented voltage measurement is the rapid increase of signals with the number of segments and number of strands. Since the space inside a high field magnet is limited, implementing voltage taps could be challenging.

The proposed measures reduce the inductive component, but at a cost. Although the inductive voltage can be partly opposed, the resistive component preceding a prequench remains small due to the slow normal zone propagation. As already been mentioned in the introduction (Figure 1.3), the resulting hotspot temperature of the quench is many times higher compared to LTS materials, as was shown in Figure 1.3.

The required intervention time at high currents ($> 1000\,\mathrm{A\,mm^{-2}}$) for HTS applications is very demanding. Due to the locality of HTS cable quench, conventional voltage detection is not sufficient at high current densities, since the precursors to a full quench are too small to detect and detection after the full quench allows too little time for intervention <30 ms. Other types of detection should be explored for this demanding operating region.

4.2.3. QUENCH ANTENNA

Pick up coils or quench antennas detect quenches by measuring the local field distortion due to current redistributions. A cross section of a quench antenna for accelerator applications is shown in Figure 4.6. Abnormal behaviour of the magnet is measured by variations in the higher order (quadra and sextrapole) magnetic fields. LTS magnet applications of quench antennas have proven to be able to recognize a developing quench by detecting field peturbations from flux jumps and the developing quench front [66]. By measuring the field disturbance on multiple locations the position of the normal zone could be determined. Slower developing LTS quenches, such as caused by wire movement, have shown to be more difficult to detect. As a consequence

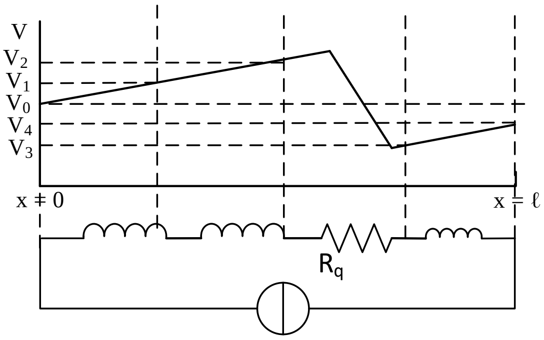

Figure 4.5: Segmented voltage measurement for quench detection. By measuring the voltage over multiple points along the coil, the inductive and resistive voltage can be distinguished.

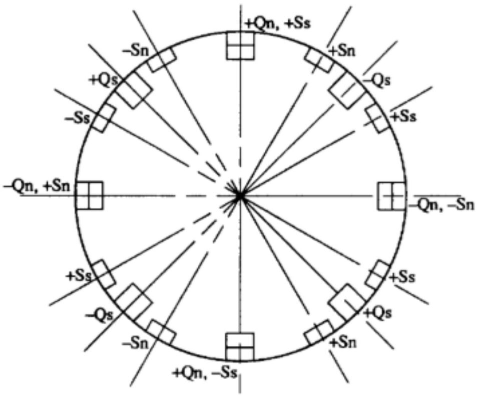

Figure 4.6: Cross section of quench antenna for the Superconducting Super Collider (SSC) [69] consisting of four windings: Skew (s) and normal (n) quadrapole (Q) and sextapole (S) windings to measure variations in higher order fields caused by a quench event.

of the gradual redistribution, the magnetic field changes remain small, making quench recognition from the background noise more difficult [67].

The amplitude of the signal shows a clear operating current dependence, while the signal's shape is roughly constant. This dependency is caused by the current proportionality of the normal zone velocity and the increased amount of current redistributing. The field change in LTS magnets is presumably caused by the current redistribution from parts of the cable experiencing high magnetic fields, where the cable is likely to quench first, to parts subjected to lower fields. Besides, due to magnetoresistance the conductor in normal conducting state has higher resistance at high field regions, causing additional current redistributions [68].

Main advantage of the pick up coils is the ability to diagnose an existing magnet without including extra sensors to the magnet itself. The quench antenna can be inserted using a probe inside the magnet's aperture and remotely detect a developing quench. Although the concept has been proven in LTS applications, its use in HTS seems limited due to the slow normal zone propagation causing small field disturbances.

4.2.4. CONCLUSION

Quenches in HTS magnets caused by local disturbances result in small and slowly developing normal zones. Various LTS quench detection methods have been reviewed for HTS magnet application, including conventional voltage detection. The locality of the normal zone causes rapidly rising hotspot temperatures, while the sensor signals remain small until the runaway has fully developed. Especially at high current densities, the thermal instability causes permanent damage within the order of tens of milliseconds, allowing insufficient time for intervention.

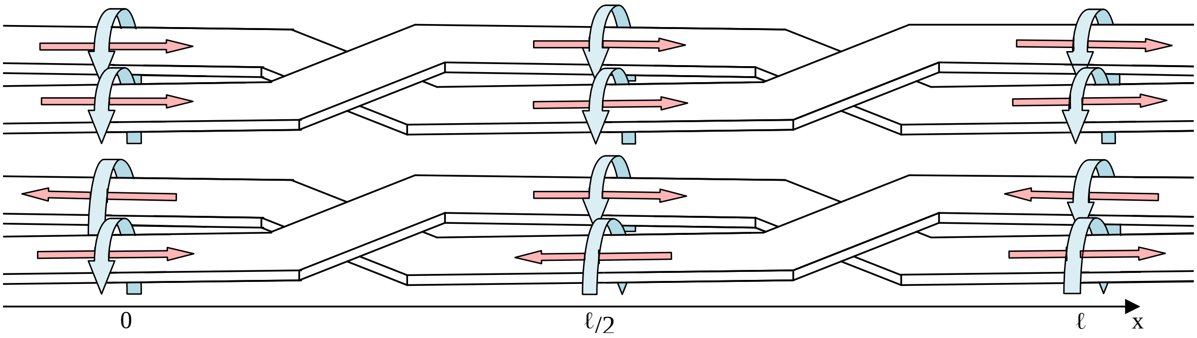

Figure 4.7: Magnetic flux change due to variation of transport current (top) and due to current redistribution (bottom) in a 2 strand Roebel cable.

Due to the inherent slow propagation of heat and the limitations of temperature sensors, they are, apart from detecting drift (and low current density quenches), of limited use for detection of quench caused by local disturbances. The slow heat propagation causes inadmissible latency of detection for a practical temperature sensor. Non conventional sensors, such as optical fibres, offer potential to detect abnormal temperature variations near the conductor.

Specifically at high current densities (J_e >1000 A mm^{-2}) the required intervention time is too stringent for adequate protection using conventional voltage detection. Due to the intervention delay and high thermal instability, quench in HTS magnets at high current density J_{op} remains therefore unprotected. The squared proportionality of ohmic heating with current reduces allowed intervention time significantly after full quench. Hence, it is essential to detect the development of a quench in an early stage, before the quench has fully developed.

4.3. PICK UP COIL OPTIMISATION

In the previous section various measurement principles were presented and evaluated, which showed the difficulties of detection at high energy densities causing limited allowable detection and intervention intervals. Measuring one of the precursors of quench can offer an outcome. Current redistribution inside the cable has revealed itself as a potential candidate, since it emerges well in advance of the full quench. This section will study the electromagnetic behaviour of a cable caused by the current redistributions. Although the main principle could be applied on various kinds of cable types, this report will focus specifically on the Roebel cable geometry. An illustration of the magnetic field in a 2 strand Roebel due to the transport current and the current redistribution in the cable is shown in Figure 4.7. The electromagnetic behaviour and the detection principle are explained in further detail, starting with a simplified 2D representation.

4.3.1. 2-DIMENSIONAL REPRESENTATION

The tape stacks in a Roebel cable (Figure 3.30) are simplified to 2 dimensions by assuming two parallel infinite length conductors, as shown in Figure 4.8. Although the Roebel cable consists of a complex 3D geometry with many strands, the underlying mechanism remains identical which will be considered in the next subsection.

Current causes a circular magnetic flux around the conductor. Following the law of Biot Savart law, the flux is proportional to the conductor's current:

$$\mathbf{B} = \frac{\mu_0 I}{4\pi} \frac{d\vec{\ell} \times \vec{r}}{|\vec{r}|^2}, \tag{4.3}$$

with magnetic permeability μ_0, vector $\vec{r}$ connecting the current carrying element $d\vec{\ell}$ and a point in space. Note that the field is assumed to be linear with respect to the current, which allows to use the superposition principle.

The wires are located in the xz-plane and separated by distance w, as shown in Figure 4.8. In nominal operation both sides of the cable carry equal current. hence $I_1 = I_2 = I/2$. The field given at the center line

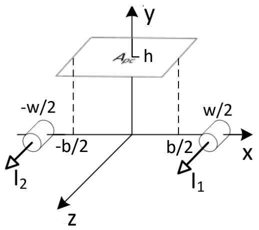

Figure 4.8: Schematic representations of a 2 strand cable for analytic magnetic field calculations.

$[x = 0, y = h]$ is given by:

$$\mathbf{B}_0 = -\frac{\mu_0 h I}{\pi(\frac{w^2}{4} + h^2)}\mathbf{i}. \tag{4.4}$$

Magnetic flux $\mathbf{B}_0$ is the primary field at nominal operation of the magnet. If a quench occurs in one of the strands, the current redistributes from one strand to the other. If the transport current I remains constant, the current in the two strands of the cable are coupled by:

$$\frac{dI_1}{dt} = -\frac{dI_2}{dt} = \frac{di}{dt}, \tag{4.5}$$

with the loop current i. Since this behaviour is expected to occur preceding a quench, the magnetic field change caused by this redistribution is studied. By applying the Biot Savart law, the field change at the mid plane is found to be proportional to the current redistribution:

$$\frac{d\mathbf{B}_r}{dt} = -\frac{\mu_0 w}{2\pi(\frac{w^2}{4} + h^2)}\frac{di}{dt}\mathbf{j}. \tag{4.6}$$

Since this problem is linear, the magnetic field change is not dependent on the field nor the constant transport current. Combining Equation 4.4 and Equation 4.6 results in the total flux change at the symmetry plane $(x = 0)$:

$$\left.\frac{d\mathbf{B}}{dt}\right|_{y=0} = \frac{dB_0}{dI}\frac{dI}{dt}\mathbf{i} + \frac{dB_r}{di}\frac{di}{dt}\mathbf{j}, \tag{4.7}$$

with current redistribution i and transport current I. Both flux change components $\frac{dB_0}{dI}$ and $\frac{dB_r}{di}$ are shown in Figure 4.9.

The high strength main field B_0 of the magnet is a common noise source for any measurement inside the magnet, due to imminent power supply oscillations. To detect the quench, the sensor should:

1. Measure field changes due to redistribution $\frac{d\mathbf{B}_r}{dt}$;
2. Discard response to main field changes $\frac{d\mathbf{B}_0}{dt}$ [68].

Note that the main magnetic flux $\mathbf{B}_0$ points in x-direction, while the field change due to redistribution occurs in y-direction. If the sensor is only sensitive in y-direction, the redistribution could be effectively measured.

To enhance the signal from the current redistribution the height between the sensor and the cable should be minimized, $w \ll h$, while the main flux $\mathbf{B}_0$ decreases to zero. Hence even if the sensor is not fully rejecting field changes in y and z-direction, the error from measuring the change in main field $\frac{d\mathbf{B}_0}{dt}$ is kept minimal when placing the sensor near the cable.

The current redistribution can be measured by the resulting EMF in a coil. The EMF is given by Faraday's law:

$$V_{pc} = -N\frac{d\Phi}{dt} = -NA_{pc}\frac{d(\mathbf{B}\cdot\mathbf{n})}{dt}, \tag{4.8}$$

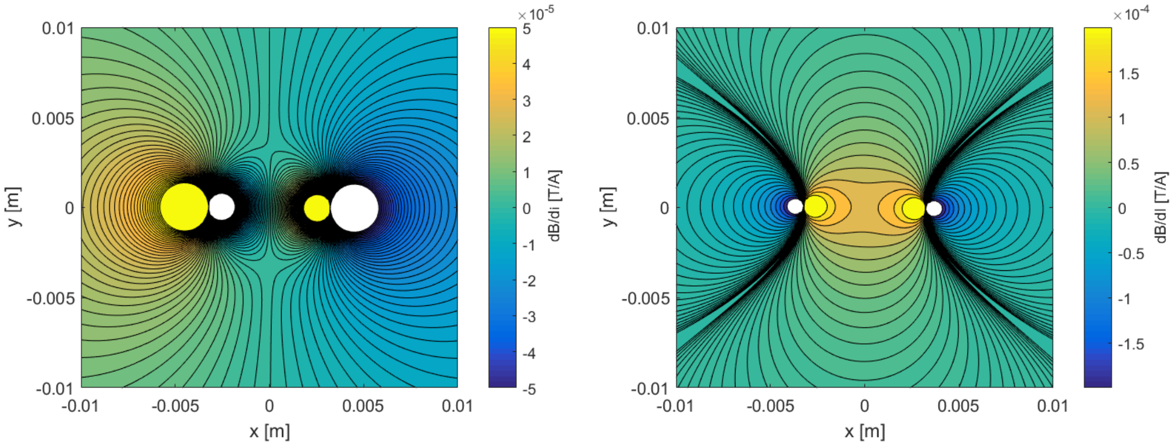

a. Main magnetic field $B0$ from transport current I, $\frac{B_0}{dI}$ **b.** Magnetic field B from redistribution current loop i, $\frac{dB_r}{di}$

Figure 4.9: Field change from current redistribution i and transport current I in the plane parallel to the cross-section of the cable.

with number of turns N and area A_{pc} with normal vector $\mathbf{n}$ of the sensor coil. Since $\frac{dB_r}{di}$ points in vertical (y-) direction, the normal vector $\mathbf{n}$ should be aligned with this field change. Hence, the area of the coil is placed parallel to the xy-plane at $y = h$, as shown in Figure 4.8.

In order to create a signal, the sensor should have a finite area A_{pc} for the flux to pass through. Again using the Biot Savart law to calculate the field change from a current redistribution in space [x,y] of Figure 4.8:

$$\frac{d\mathbf{B}}{dt}(x,y) = \frac{\mu_0}{2\pi}\left\{\left[\frac{h}{y^2+(x+\frac{w}{2})^2)} - \frac{h}{y^2+(x-\frac{w}{2})^2)}\right]\mathbf{i} + \left[\frac{x-\frac{w}{2}}{y^2+(x-\frac{w}{2})^2} - \frac{x+\frac{w}{2}}{y^2+(x+\frac{w}{2})^2)}\right]\mathbf{j}\right\}\frac{di}{dt}. \tag{4.9}$$

with cable width w. Note that for $x = 0$ the equation reduces to Equation 4.6.

For $y \neq 0$, the main field B_0 in y-direction is unequal to zero. However, since the field is anti-symmetric over $y = 0$, the contribution of the main field B_0 is cancelled by centring the pick up coil in the middle of the cable, as shown in Figure 4.8.

To obtain the signal's voltage, the field needs to be integrated over the area of the pick up coil A_{pc}, shown in Figure 4.8. If the coil is assumed to be square with width b, the sensor voltage is found by Equation 4.9 substituted in Equation 4.8:

$$V_{pc} = -NA_{pc}\frac{\mu_0}{\pi}\ln\left[\frac{h^2+\left(\frac{w}{2}-\frac{b}{2}\right)^2}{h^2+\left(\frac{w}{2}+\frac{b}{2}\right)^2}\right]\frac{di}{dt} = -\beta\frac{di}{dt}, \tag{4.10}$$

with the sensor's sensitivity β. A dimensionless parameter study is performed with this formula, which is shown in Figure 4.10. This figure shows the dimensionless signal's sensitivity versus the relative width of the sensor for various relative sensor height ratio's h/w. The optimum width to obtain the maximum signal is found at:

$$b_{opt} = \sqrt{4h^2+w^2}, \tag{4.11}$$

with optimal sensor width b_{opt}. For $b > b_{opt}$, the signal reduces while the area A_{pc} grows, hence the signal to noise ratio is expected to deteriorate.

Since the study has limited itself to the 2 dimensional case, it was assumed the strands were straight, infinitely long and limited diameter ($w \gg d$). Although this is a reasonable assumption for understanding the mechanism, the cable geometry cannot be neglected for the detection design.

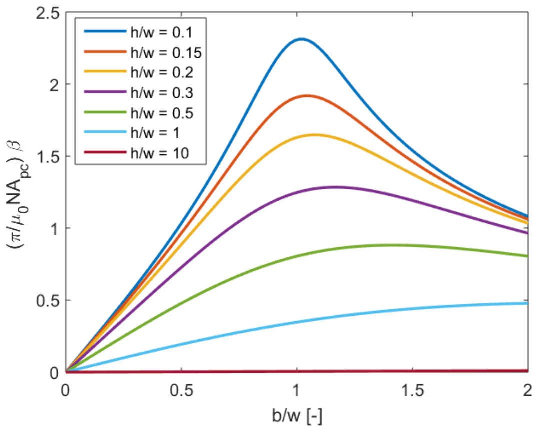

Figure 4.10: Dimensionless pick up coil parameter study based on Equation 4.10 for optimising its location. The dimensionless sensor sensitivity $\beta\frac{\pi}{NA_{pc}\mu_0}$ is shown as function of the relative coil width b/w for various relative coil's distances h/w. Both dimensions are relative to the cable's width, which is kept constant. The pick up voltage signal increases when the coil is closer to the cable ($h/w \to 0$) and shows an optimum b_{opt} when width of the coil approaches the width of the cable ($b/w \approx 1$).

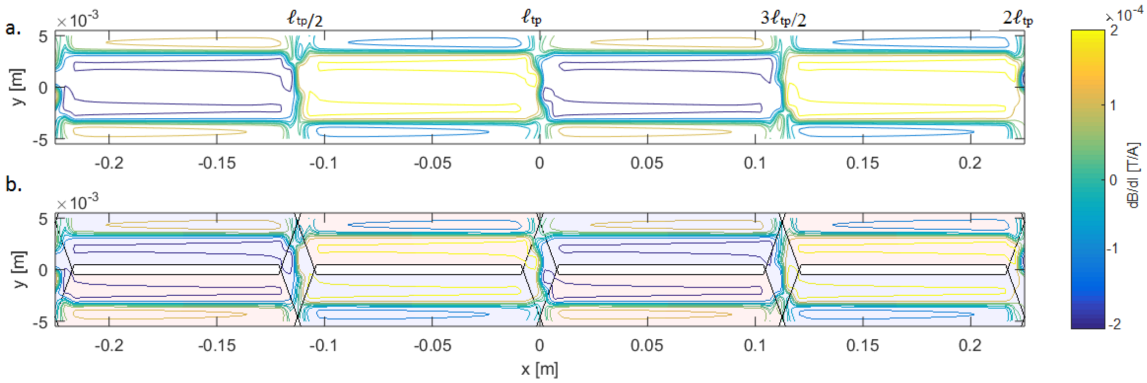

Figure 4.11: Field change based on the model of Appendix B for a single strand quench in a 2 strand Roebel cable with transport current flow from left to right; a. Flux change in z-direction from current redistribution i; b. Flux change including the Roebel cable geometry (Quench occurring in red tape).

4.3.2. ROEBEL GEOMETRY

As discussed in Section 2.4, a Roebel cable consists of multiple tape strands braided together. Since analytic models are very cumbersome in their application, a numerical model for describing the magnetic field of a 2-dimensional Roebel cable is introduced in Appendix B.

As been discussed in Section 2.4, the pattern of the cable geometry is repetitive for every twist pitch ℓ_{tp}. Provided no current redistribution occurs along the cable's length, the magnetic field pattern repeats itself accordingly. The calculated field change due to a redistribution current i in a 2 strand cable is shown in Figure 4.11a and b. The meandering geometry of the quenched strand causes the field to change at each crossover. Hence, the maximum pick up coil length is limited to half a twist pitch $\ell_{tp}/2$. A second pick up coil can cover the rest of the twist pitch, which can be placed in series to double the signal (when respecting their opposite polarity). Due to their opposite polarity, any (homogeneous) background field is rejected.

Up to now only two tapes are considered for simplicity, while the model can be easily extended to n tapes by transposing each neighbouring tape by ℓ_{tp}/n (Figure 2.9). The initial principle remains the same, but the current has the freedom to redistribute to more strands. During a quench in a two strand cable the current redistributes from the quenched strand (red) to the superconducting strand (blue), resulting in the field shown in Figure 4.11. Since the two strands are transposed 180° in phase, the field change resulting from the redistribution is maximum. In a cable containing more than 2 strands, the current will redistribute to strands with smaller phase shift, hence reducing the sensitivity of the sensor β. Since the signal scales proportionally

n	Scaling [-]	n	Scaling [-]
2	1	12	0.546
3	0.667	15	0.533
4	0.667	30	0.517
5	0.6	50	0.510
8	0.571	100	0.505

Table 4.2: Scaling factor γ of the field change from a current redistribution as function of number of strands.

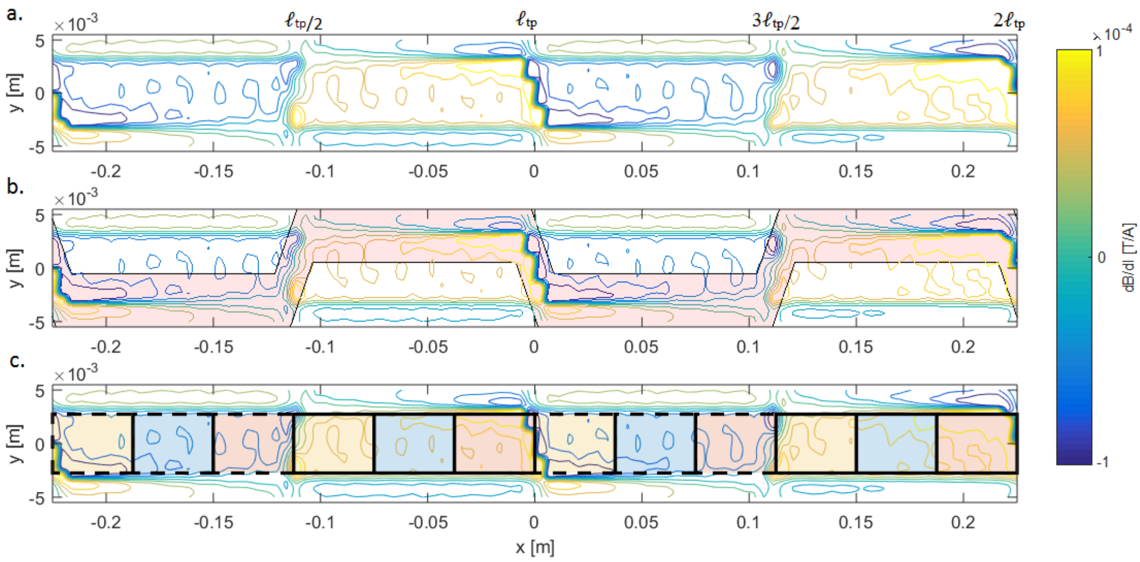

Figure 4.12: Field change based on the model of Appendix B due to single strand quench in a 15 strand cable with transport current flow from left to right; a. Flux change in z-direction from current redistribution i; b. Flux change including the Roebel geometry of the quenched tape; c. Pick up coil quench detection proposal, consisting of 3 arrays. The coils with the same colour placed in series, while the border shows their electric phase.

with the phase and assuming the current redistributes evenly over the remaining tapes in a cable with evenly spaced crossovers, the field change scales as function of the number of strands n:

$$\gamma = \frac{1}{\pi(n-1)}\sum_{k=1}^{n-1}\left[\pi - \left|\pi - k\frac{2\pi}{n}\right|\right] = \frac{1}{n-1}\sum_{k=1}^{n-1}\left[1 - \left|1 - k\frac{2}{n}\right|\right], \tag{4.12}$$

with γ the scaling factor between the field change of a n-strand and a 2-strand cable with constant redistribution current i. The scaling factor γ is shown for various number of strands in Table 4.2. For $n \to \infty$, the scaling factor approaches 0.5, since the current redistributes evenly over the two tape stacks of the Roebel cable. For a 15 strand cable a scaling γ is found of 0.533, which confirms the field change based on Appendix B, shown in Figure 4.12a.

Apart from this scaling factor, the signal amplitude is further reduced by an increasing number of strands since the current carried by the individual tapes is lower (assuming constant I_{op} of the cable, Equation 3.7). Hence the redistributed current i from a strand quench will be lower, which causes a reduced signal in the pick up coils. Hence, to optimise the signal from a current redistribution caused by a local quench, the number of strands in the cable should be kept to a minimum.

Pick up coil detection for cables consisting of many strands makes a dedicated sensor for each strand cumbersome. By reducing the length of the pick up coils, the redistributions in multiple strands can be monitored simultaneously by a single coil. A design with 3 coils per half twist pitch is shown in Figure 4.12c and Figure 4.13. The three coils covering half a twist pitch form three separate arrays, which are indicated by their colour. Within the array, each coil separated by half a twist pitch is connected in series, with their electric

Figure 4.13: Representation of the proposed pick up coil design with actual Roebel geometry. The colours correspond to each of the 3 arrays, while their border shows their polarity with respect to each other.

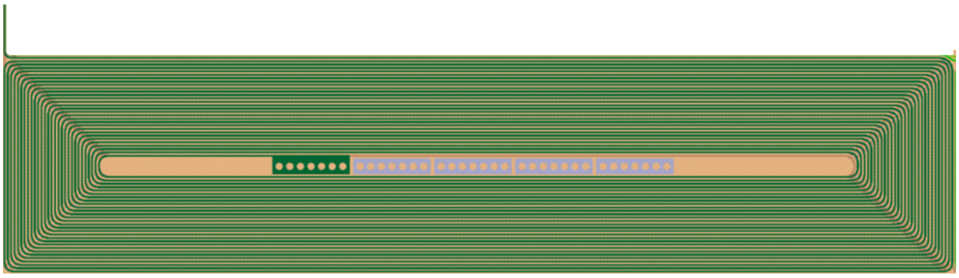

Figure 4.14: PCB single layer pick up coil design. The coil consists of 30 µm windings per side, with connection pads to the other layers located in the center.

polarity indicated by its border. Using the three arrays the redistribution in each strands can be detected, since at least one array is not overlapping with its crossovers.

4.3.3. PCB

Although this principle of detection has a numerically validated potential, its practical implementation is less evident, since space in high field accelerator magnet design is a valuable commodity. For successful implementation, one should use the available space as efficiently as possible.

Since the current redistribution develops over the order of meters, it is possible to cover the quench detection of small magnets with one pick up coil array. The magnet's leads are generally an easy accessible position with less stringent space limitations, as in Feather M0.4, discussed in the next section and Chapter 5.

For larger magnets, more arrays are required to cover the length of conductor. As been analytically shown in Section 3.2.3 and numerically in Section 3.3.5, current redistributions can occur along the length of the cable, depending on the quench, cable and magnet properties. Due to current redistribution inside the cable the current in the conductor can vary along its length, hence reducing the sensor's signal. The sensor should therefore be able to be co-wound with the conductor to measure the current redistributions close to the normal zone. The sensor should comply with the following requirements:

1. Minimum dimension, not exceeding the cable width;
2. Minimum thickness and flexible for co-winding;
3. Electrically insulated from cable winding.

Flex Printed Circuit Boards (Flex PCB) was chosen for this purpose. The PCB consists of a copper layer deposited on a sheet of Kapton. The electrical circuit is covered with a mask, and the uncovered copper layer is etched away. Since a single layer PCB is only approximately 150 µm thick, multiple layers can be stacked upon each other to increase the number of windings. The low E-modulus of the Kapton allows the sensor to bend up to a certain extent, allowing to following the winding's curvature. Disadvantage of the low E-modulus is the expansion under pressure due to the poison ratio. Fibre reinforced materials could be a solution in applications with unavoidable high stresses. The anisotropy allows bending while the fibres resist overstraining the electrical circuits in planar direction.

The single layer pick up coil design is shown in Figure 4.14. A 100 µm wide copper trace is deposited on the kapton back sheet comprising of 30 windings. The trace ends inside a coil at a connection pad, which allows connection to the adjacent PCB layers through metallized holes. The individual layers are electrically insulation by intermediate 50 µm thick Apacal insulation foils. The implementation of pick up coils in Feather M0 and M2 are considered in more detail in the remainder of this section.

Property [70]	[µm]
Kapton backsheet thickness	50
Copper layer thickness	5
Apical insulation thickness	50
Adhesion materials	25
Track width	100
Track spacing	75

Table 4.3: PCB design parameters for pick up coil sensor design.

Magnet	Position	No. Coils	ℓ mm	b mm	Layers	Turns per side
Feather M0	Former	20	50	10	5 layers × 2 sides	20
	Top cap	4				
	Leads	4			1 layer × 2 sides	
Feather M2	Lower deck	12	50	10	5 layers × 2 sides	30
	Upper deck	6				

Table 4.4: Dimensions of the pick up coils in Feather M0.4 and the (future) Feather M2 design.

4.3.4. FEATHER M0

Feather M0.4 is developed as validation for the manufacturing process and quench protection. Multiple sensors are implemented for field quality measurement and quench detection, together with quench heaters to artificially trigger a thermal runaway. Since production of the magnet already started, a modified design of the proposed quench detection was implemented. Although the location of the sensors are not optimal, it offers a showcase to proof its capabilities in non-ideal circumstances.

Feather M0.4 is fitted with a variety of sensors, including pick up coil sensors for magnetic field measurement and quench detection. The various specialized pick up coils of Feather M0.4 are listed in Table 4.4. The remaining sensor types of Feather M0.4 are considered in Section 5.1.1. The pick up coil array in Feather M0.4 can be devided into three classes:

1. Quench detection on the magnet leads (Figure 5.1b 19/20);
2. Quench detection on the lead extensions (Figure 5.1b 21/22);
3. Magnetic field quality measurement inside the former (Figure 5.1a 4-7);
4. Magnetic background field measurement (Figure 5.1a 8).

The magnetic field quality and background field measurement coils are shown in the cross-section of Figure 4.15. Their implementation is further discussed in Chapter 5. Analogous to Equation 4.10, the sensor voltage for each coil is found by:

$$V_{pc} = -\sum_{i=1}^{n} \beta_i \frac{dI_i}{dt}. \tag{4.13}$$

The estimated sensor strand current sensitivity β_i found using Appendix B is shown in Table 4.5 for all 15 strands, based on an estimated 1 mm between cable and sensor. The sensitivities show a change in polarity and reduced magnitude of coupling β_i when the coil overlaps the crossover. Although the values appear to be small, measurable signals should arise during a quench event, as will be shown in Section 4.4.3.

4.3.5. FEATHER M2

Feather M2 as accelerator magnet demonstrator, requires a reliable quench detection system. The pick up coil detection is implemented to cover its high current operating regime. Due to the high magnetic field of Feather M2, especially when operating as insert magnet in Fresca-2, the placement of the pick up coils is limited. An initial design composing of pick up coils placed on the outside winding turn was discarded after FEM analysis showed the radial stress from the coil winding exceeded locally 100 MPa [10], which is above tolerable limits of the PCB.

tape	β_i [μVA^{-1}s]	tape	β_i [μVA^{-1}s]
1	-0.3641	9	0.3410
2	-0.3617	10	0.3435
3	-0.3527	11	0.3493
4	-0.3461	12	0.3567
5	-0.3415	13	0.3735
6	-0.3353	14	0.2270
7	-0.0671	15	-0.0739
8	0.2022		

Table 4.5: Pick up sensor sensitivity coefficient β_i for every strand.

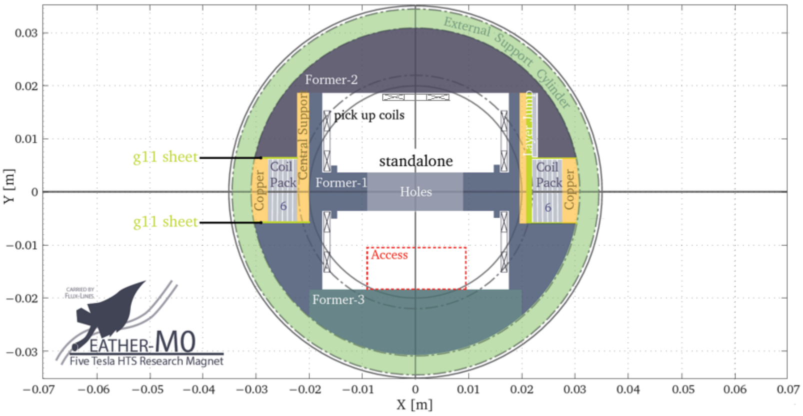

Figure 4.15: Feather M0 cross-section with the 4 magnetic field quality (left and right inside top and bottom inside the former) and single magnetic background (top) field pick up coil arrays [6].

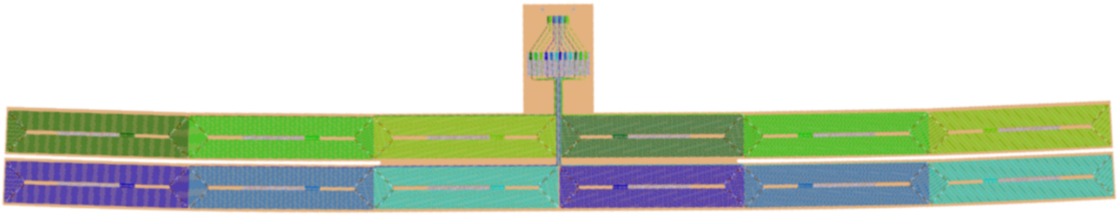

Figure 4.16: PCB component of pick up quench detection design for Feather M2: Double row design each consisting of 6 individual coils. The two rows cover the upper and lower deck respectively. The coils with corresponding colour are placed in counter series within each of the 6 arrays (3 for each deck). The top shows the connection pad for instrumentation wiring.

The revised sensor design consists of pick up arrays placed directly on the former, as shown in Figure 4.17. The YBCO cable winding is wound over the sensors, while the Kapton base layer of the sensor serves as ground insulation to the magnet structure. The sensor thickness is embedded in pockets within the former design, which assists in the alignment of the sensors.

The quench detection design for pick up detection of Feather M2 consists of 4 single row and one double row sensor, the latter is shown in Figure 4.16. The single row sensor covers only the lower winding deck of the magnet, while double row covers both top and bottom deck, as shown in Figure 4.17. Each row consists of 6 coils which cover a full twist pitch of the cable. The coils seperated by half a twist pitch are connected in series, represented by the different colours in Figure 4.16. The three arrays covering the entire bottom deck and the three arrays on the top deck form two seperate systems. Hence, the pick up quench detection for Feather M2 consists of a total of 6 channels, drastically reducing the detection complexity [8]. The pick up sensitivities estimated by Appendix B are found in Table 4.6.

	β_i [µVA^{-1} s]		
tape	Array 1	Array 2	Array 3
1	-2.1844	-2.0956	-2.0120
2	-2.1704	-2.0605	-0.4028
3	-2.1162	-2.0457	1.2132
4	-2.0769	-1.2130	2.0459
5	-2.0487	0.4030	2.0607
6	-2.0120	2.0122	2.0959
7	-0.4028	2.0490	2.1399
8	1.2132	2.0771	2.2408
9	2.0459	2.1165	1.3623
10	2.0607	2.1708	-0.4437
11	2.0959	2.1849	-2.1831
12	2.1399	0.4453	-2.1684
13	2.2408	-1.3606	-2.1127
14	1.3623	-2.2388	-2.0695
15	-0.4437	-2.1370	-2.0253

Table 4.6: Feather M2 Pick up sensor sensitivity coefficient β_i per strand for its three pick up coil arrays.

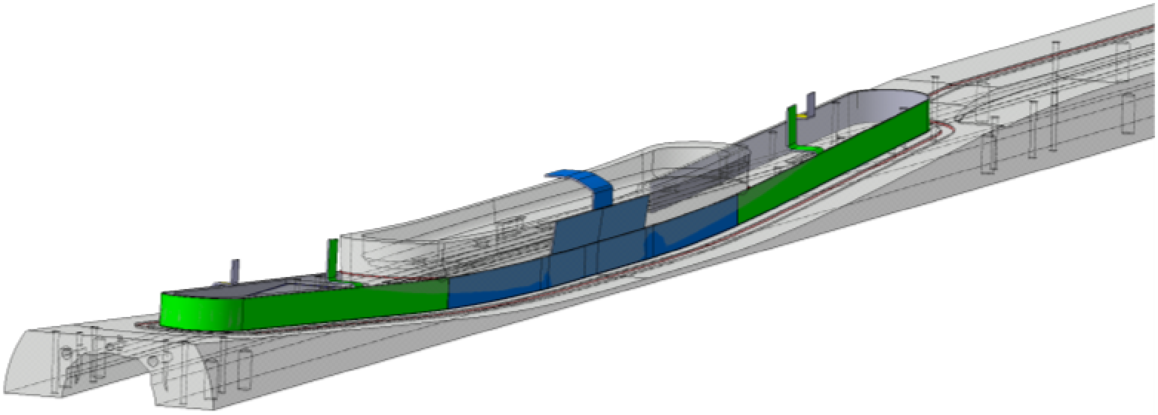

Figure 4.17: Pick up coil design placed on the former of Feather M2. Blue PCB represents the design shown in Figure 4.16, while the 4 green single row PCB designs contain 6 pick up coils each.

4.3.6. CLOSING REMARK

The broad operational field of HTS material cannot be covered by a single detection method alone. The strengths of various sensors should be combined to cover the plausible quench scenarios with sufficient reliability.

Pick up coils have the potential to detect a current redistribution preceding a quench, allowing increased time for intervention compared to conventional voltage detection. Its signal is proportional with the current density, resulting in increased signal amplitude for higher currents. Since current redistributions are occurring over long lengths compared to the normal zone size, it enables:

- Placing multiple coils in parallel, thereby enhancing the signal;
- Flexibility in positioning along the conductor;
- Cover all strands of a cable with only 3 sensors.

In the implementation of the detection design in high field magnet applications, the proposed design requires:

- Minimizing PCB out of plane stresses (< 20 MPa) [70]);

- Positioning close to the conductor [$(h/w \ll 1)$ Figure 4.10];
- Alignment of coil and cable centreline.

The PCB pick up arrays offer an integrated quench detection sensor for high field magnets, while occupying minimal space. The implementation of the pick up coils in Feather M0 is discussed in Chapter 5, while the presented detection design for Feather M2 is currently in production.

4.4. DETECTION

Several sensors have been assessed which could potentially identify a quench and their practical implementation was discussed. Based on the sensor signals the detection algorithm should identify the system's state. Within the safe time window the system has to decide either to continue powering or to trigger a fast or slow protection dump. During this idle period, the Joule heating persists and the hotspot temperature is rising, hence fast and reliable decision making is required.

This chapter will consider the potential algorithms which could be applied for detection purposes. The 2D model of Section 3.3 is applied to study the signal from the different sensors during the quench cases of Section 3.3.4, to determine each sensor's performance.

4.4.1. TEMPERATURE

Quench detection based on ideal temperature measurement of the superconductor was studied in Section 4.2.1. Table 4.1 has shown the minimum required sensor granularity which is required to detect a quench within a given time period. The required granularity based on the ideal case was followed by two potential sensor candidates. Due to the slow propagation of the normal zone (Figure 3.5) and the slow nature of heat diffusion, the ability to detect a local thermal runaway is expected to be limited. Hence, temperature detection should aim for identification of slow thermal phenomena's, such as drift and low current density quench cases. Abnormal variations in local conductor temperature from T_{op} could indicate malfunction of the magnet [63].

In an attempt to study the thermal behaviour, the 2D model of Section 3.3 is used. The model includes a 2 dimensional thermal finite difference model of the multi-strand cable, as discussed in Section 3.3.1. The spatial temperature distribution during the two cases of Figure 3.27 are studied to understand the cable's thermal behaviour.

The spatial temperature distribution of the Strand 1 and 8 during the quench of Case 1 are shown in Figure 4.18. Case 1 shows a temperature peak of T_{hs} =170 K at t = 50 ms in Strand 1 caused by the disturbance, followed by a diffusion over its length and transverse to the neighbouring strands. After the heat has diffused throughout the cable, the temperature of Strand # 8 rises gradually over its full length.

Case 2 shows a drift in both strands followed by a rapid thermal runaway of Strand #1 caused by the ohmic heating. Due to this temperature drift, Strand # 8 reaches a temperature T_{hs} =10 K at t = 0.16 ms), followed by the full quench of the cable. Since Strand # 8 carried the highest current at the end of the prequench (t = 0.17 ms. Figure 3.27b), its temperature shows a very steep ascend.

From a detection point of view, the longer quench duration at low current density cases (such as Case 1) allow the heat to diffuse over both the length and width of the cable, enabling the sensors to identify an abnormal temperature gradient. High current density cases are generally too unstable to be detected by temperature quench detection. However, the slow drift of Case 2 allows the heat from the disturbance to diffuse over the cable, resulting in potentially measurable signals ($T \approx$10 K). Based on the observations during these two cases, temperature sensors should aim for the detection of:

1. Low current density (Shown in Case 1);
2. Drift (Shown in Case 2).

Within the model a spatial temperature distribution of an adiabatic cable was considered, which is insulated from its surroundings, offering ideal conditions for temperature detection. Actual signals during a quench are expected to be significantly lower, due to its practical implementation. Since this is a very simplified repre-

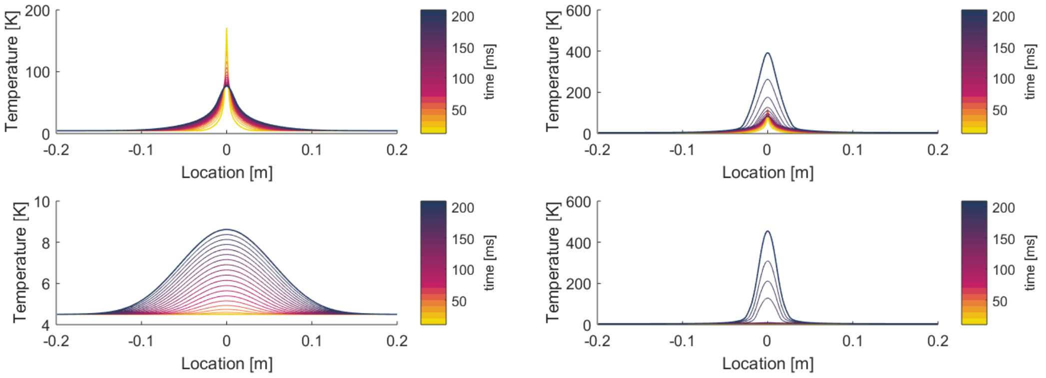

a. Case 1: 650 $\mathrm{A^2\,mm^{-1}}$ (Figure 3.27a); **b.** Case 2: 1250 $\mathrm{A^2\,mm^{-1}}$ (Figure 3.27b).

Figure 4.18: Spatial distribution of the temperature in the affected Strand 1 (top) and Strand 8 (bottom) during the quench events of Figure 3.27 [21].

sentation, results should be considered qualitative. Simulation of heat diffusion requires detailed modelling including the 3D magnet geometry.

Although temperature quench detection has numerically proven potential to detect drift and low current density quench, implementation in HTS magnet applications is not trivial. Practical temperature detection is considered subsequently in two different cases: Liquid and gas cooling.

Direct threshold detection based on the local temperature inside the magnet is a viable option when testing in liquid helium or nitrogen. The phase transition ensures a stable temperature throughout the cryostat of 4.5 K or 77 K respectively. An abnormal temperature deviation could reveal a potential quench source. Tight threshold ΔT for temperature deviation can be set to minimise detection time t_{det} (Equation 4.2).

Detection based on temperature in a helium or nitrogen gas environment is more complex, due to temperature variations of the coolant. Variations in the inlet coolant temperature can cause temperature gradients between parts of the magnet in direct or indirect contact with the coolant gas. A temperature deviation does therefore not relate directly to a quench. Two options of detection are considered:

1. Local temperature gradient;
2. Temperature time derivative.

By comparing the signal of two sensors with comparable conditions (type, location etc.), the abnormal behaviour can be identified by comparison of the two values. Comparison of non-adjacent sensors is preferred for detection, for example located in opposite poles, to detect the drift in larger lengths of conductor.

A sudden rise in temperature can indicate a hotspot forming. Since differentiation of measurement data introduces noise, low pass filtering for signal conditioning is needed. Noise rejection is of primary concern, which is dealt with briefly in the following chapter.

Hence, the temperature sensor sensitivity ΔT of Section 4.2.1 does not relate directly to the practical sensitivity of the quench detection. Both noise sources and natural temperature gradients can arise within the magnet during operation. Hence, the practical sensitivity of the detection is governed by the ability to recognize abnormal (quench) behaviour from these natural temperature variations and background noise.

4.4.2. VOLTAGE

The limitations of conventional voltage threshold detection were considered in Section 4.2.2 and quantified based on the numerical simulations. Several existing sensor and measurement techniques for signal enhancement were presented. Voltage detection in LTS applications aims for measuring the resistance rise during a full quench of the cable. To illustrate the challenge of quench voltage detection, the voltage of both cases studied in Section 3.3.4 are considered. The resistive voltage of each strand (continuous) and the total voltage measured over the magnet (striped) for both cases are shown in Figure 4.19.

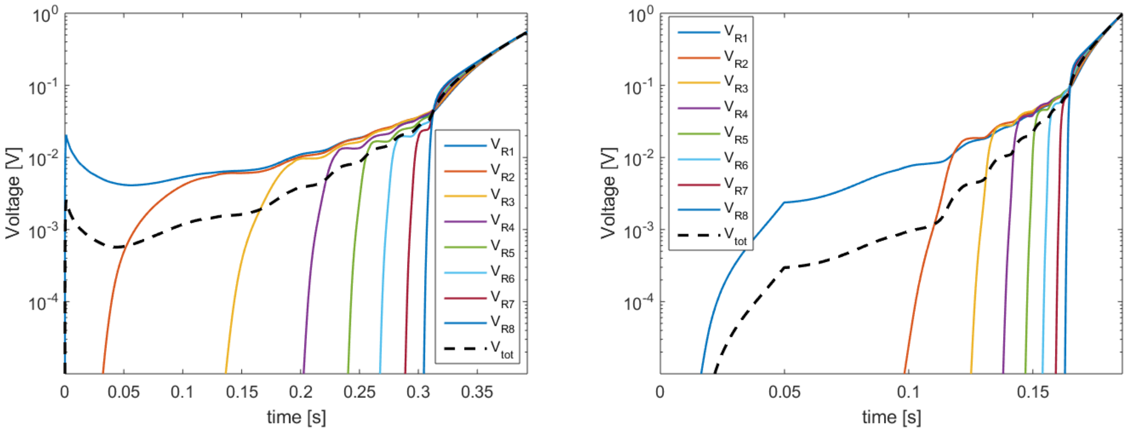

a. Case 1: 650 $A^2\,mm^{-1}$ (Figure 3.27a);

b. Case 2: 1250 $A^2\,mm^{-1}$ (Figure 3.27b).

Figure 4.19: Resistive voltages V_{ri} for each strand (continuous) and measured voltage over the magnet V_{tot} (dotted line) during the quench the two cases of Section 3.3.4.

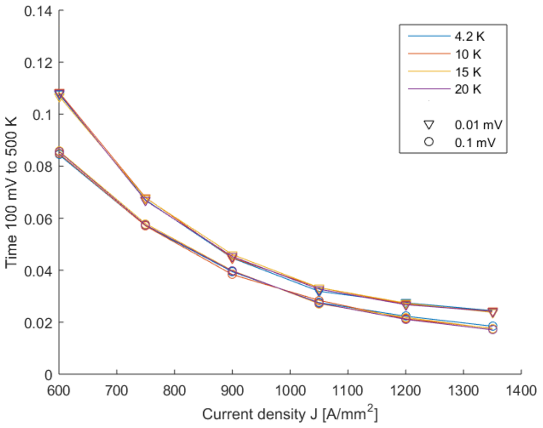

Figure 4.20: Maximum allowable intervention time versus current for 0.01 V and 0.1 V detection threshold at 17 T

Apart from the sharp voltage spike following the disturbance pulse in case 1 at $t = 0$, the voltage shows a gradually rising pattern which increases with the spread of the normal zone. It shows a step behaviour for each subsequent strand transitioning to normal conduction. Distinctive voltages (i.e. 10 mV) arise when the magnet nears the full quench. As been shown in Section 4.2.2, voltage detection with a threshold of 100 mV is only sufficient for lower current densities (<1000 $A\,mm^{-2}$).

In order to detect the signal in an early stadium, inductive components and noise should be rejected as much as possible. In Section 4.2.2 the measures to reduce the inductive voltages were already studied. Since the voltage during a quench is a gradually rising signal, low pass filters (For example f_c =40 Hz) can be used for noise rejection, while analogue detection electronics are preferred for their fast response.

By either reducing the inductive signal or lowering the protection threshold the quench can be detected earlier. In Figure 4.20 the effect of a tighter threshold is shown. By lowering the threshold by a factor 10, only marginal improvement is found (approximate increase of 50 $A\,mm^{-2}$). Additionally, since this voltage is reached during the prequench, the time between 10 and 100 mV is quench dependent (As shown in Section 3.3.4).

4.4.3. PICK UP COILS

The analytic study of Section 4.3 showed the potential of the pick up coil sensors to detect a quench in the prequench stage by measuring magnetic flux changes following from a current redistribution. The pick up

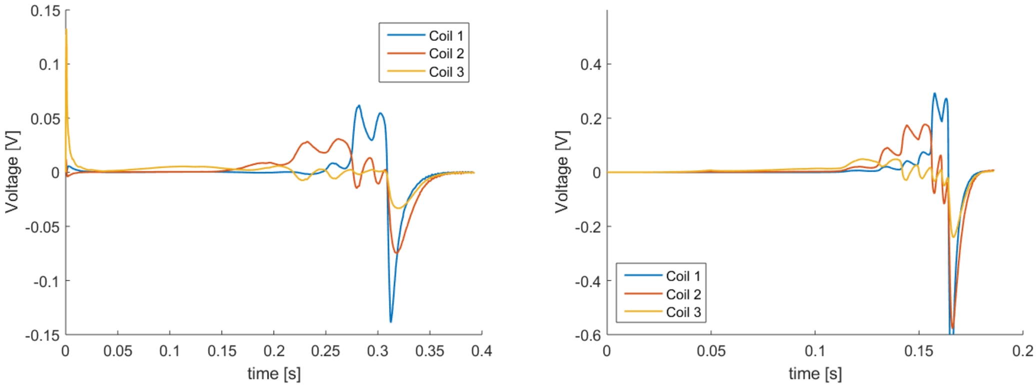

a. Case 1: 650 $\mathrm{A^2\,mm^{-1}}$ (Figure 3.27a); **b.** Case 2: 1250 $\mathrm{A^2\,mm^{-1}}$ (Figure 3.27b).

Figure 4.21: Pick up coil signal per coil for the three sensor arrays during the quench events Figure 3.27. The voltage V_{Ri} denote the resistive voltage of strand i, while the dotted line shows the signal over the magnet V_{tot}.

coil signals during a quench are studied based on the cases of Section 3.3.4. The current redistribution during the quench was already presented in Figure 3.27. By applying Equation 4.13 with the values found in Table 4.6, the signals presented in Figure 4.21 are found.

Apart from the difference in quench duration, the signal's amplitude differ approximately a factor 4 between both cases, hence the performance of pick up coil quench detection clearly enhances with increasing current densities. The short and high power disturbance of Case 1 results in a sharp peak of the signal at $t = 0$ caused by the high current redistribution from the quenched strand (similar to the voltage peak observed at $t = 0$ in Figure 4.19a). Meanwhile the slower disturbance of Case 2 causes a drift, where per definition no current redistributions occurs since all strands are still superconducting. The quench of the first strand causes in both cases the highest signal in coil array 3, which does not overlap with the tape's crossovers. The subsequent quenches of the remaining strands are accompanied by increasing amplitude, due to the higher currents and faster redistributions, as can be seen in the current profile of Case 1 and Case 2. While Array 3 shows the highest signal during the quench of Strand 1, the transposition of subsequent strands causes their crossover to overlap with this array. Hence Array 2 shows therefore the highest signal for quench of strand 2-4, while Array 1 shows the highest signal during the quench of strands 5-9. The full quench causes a final redistribution to all the tapes, resulting in a sharp peak with opposite sign in all three arrays.

Comparison of the two cases show similar signal behaviour for both quench events with three main distinctions:

1. Signal during drift/prequench, caused by the difference in disturbance.
2. Signal's duration/frequency, caused by the decreased stability at higher current densities.
3. Amplitude of signal, caused by the higher currents and faster redistributions.

The signal amplitude of a single coil during the prequench is significantly higher compared to the voltage signal of Figure 4.19. Measurable signals arise well before the quench occurs, allowing sufficient intervention time.

If a single strand quenches, the specific strand can be identified by the pick up coil signals, since the signal in the three arrays differ for the current redistribution of each of the strands. A low signal in one of the arrays suggests the array's coils to overlap with the crossovers of the tape, while the polarity of the signal indicates the tape stack in which the strand is located. Therefore the signal data can offer insight in the current redistribution which has occurred.

A Discrete Fast Fourrier Transform has been performed to study the signal's frequency content. The spectrograms of both signals are shown in Figure 4.22. The responses show, despite of the differences already mentioned above, great similarity in the frequency domain. The frequency bands caused by the redistribution of each strand quench (indicated by the red arrows) could serve as an indicator for the upcoming quench. The resemblance between both events suggests the prequench behaviour is a characteristic of the superconduc-

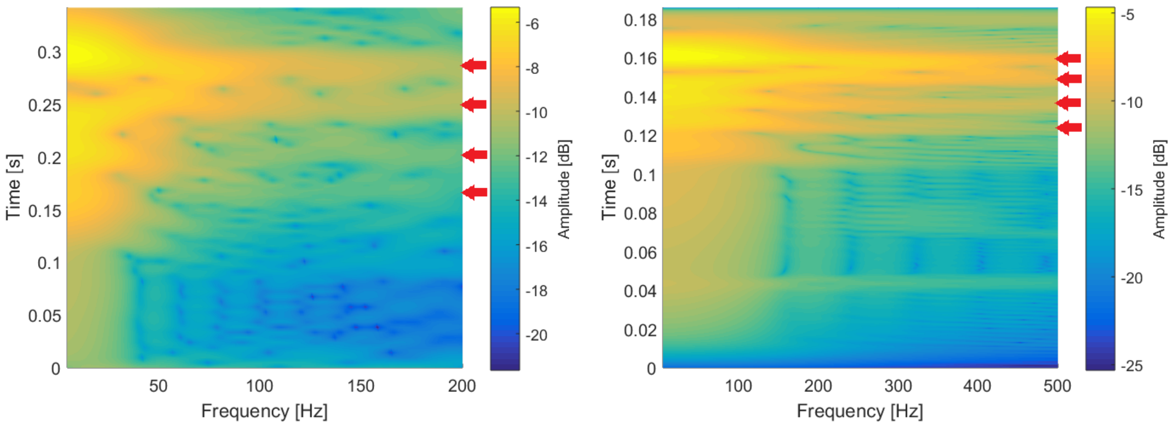

a. Case 1: 650 A (Figure 3.27a);

b. Case 2: 1250 A (Figure 3.27b).

Figure 4.22: Spectogram of the pick up coil signal of array 1 for the cases of Figure 4.21. The figures show the frequency content of the signal (x-axis) versus the duration of the signal (y-axis). The colours depict the voltage amplitude in decibel.

tor cable. Although only two cases of the wide operating and possible disturbance domain were considered, the existence of these frequency bands could be potentially useful for future quench detection.

The main observations with respect to quench detection design based on the two events are:

1. Signals appear well before the occurrence of a full quench;
2. Qualitative comparison shows analogous behaviour for two cases;
3. The instability is characterized by signals from subsequent strand quenches with increasing amplitude and frequency;
4. Signal due to redistributions during prequench and full quench show opposite polarity.

4.4.4. Detection scheme proposal

Based on the insight gained from the behaviour of HTS quench, the proposed detection scheme for Feather M2 is presented in Table 4.7. The conceptual detection algorithms should include the following concepts:

1. Temperature:
    - Abnormal temperature gradients (gas/liquid cooling dependent) or;
    - (Conductor) Temperature approaching T_{cs} or;
    - Temperature rise of resistive joints.
2. Voltage
    - Resistive voltage of superconductor or;
    - Resistance runaway of resistive connections.
3. Pick up coil
    - Fast (and local) redistributions or;
    - Subsequent chain of redistributions.

Note the operating domains covered by the voltage and pick have to overlap in order to assure reliable quench detection. Whether this condition is satisfied depends on the actual magnet conditions, indicated by the asterisk.

	Operating temperature	
	High T_{op}	Low T_{op}
Drift	Optic fibre	
Prequench	Pick up coil*	Pick up coil
Full quench	Voltage	Voltage*

Table 4.7: Proposed Feather M2 quench detection scheme for the various stages of a quench.

4.5. CONCLUSIONS

The locality of the normal zone restrains the ability of detection, while the unstable runaway poses high demands for timely intervention. The operating domain of HTS materials is too broad to be covered by a single detection system. Temperature sensors are restricted to drift behaviour (and low current density quench detection), while conventional voltage detection is expected to offer adequate protection up to $1000\,\mathrm{A\,mm^{-2}}$. The performance of existing methods offer only adequate protection within the low to medium current density operating domain.

The introduced pick up coil concept offers numerically proven potential to identify a prequench, allowing time for intervention at high current densities ($> 1000\,\mathrm{A\,mm^{-2}}$). Its signal enhances with increasing current density, therefore considered as supplementary to the existing detection systems. Based on insight of HTS cable quench gained by studying the model, a detection concept combining multiple detection systems for HTS magnets is proposed.

4.6. DISCUSSION

Understanding of HTS cable quench behaviour resides on extensive modelling and its underlying assumptions. Although the proposed quench detection system shows potential in numerical simulation of the high performance operating domain, the actual quench behaviour remains difficult to predict. Nevertheless, the parameter sweep of the previous together with the expected quench signals suggest the viability of the detection layout.

For increasing current densities the performance of the pick up arrays is expected to increase while the ability of voltage detection depreciates. It is uncertain the protection coverage of both systems overlap, offering adequate protection in the entire operating domain. As been shown in Section 3.3.4, the total quench duration including the prequench shortens with increasing current density. Since the stability of the cable decreases while the current density J approaches J_c, the prequench will get shorter. Hence, the pick up coil detection will be limited in operating domain by the duration of the (pre)quench and the time of intervention measures to take effect.

Additionally, symmetric quench cases exist where only limited "stack to stack" current redistribution will occur with very limited pick up coil signal as result. For example if a quench is initiated at top and bottom of the Roebel cable, the symmetry of quench causes only minimal signals. Analogous to the balanced bridge voltage detection discussed in Section 4.2.2, additional quench detection is required to cover this exceptional but risky event.

The simulated pick up coil signals are based on sensor sensitivities β_i which are calculated by Appendix B. These parameters show a high dependence on the distance to the coil (As shown in the dimensionless study of Figure 4.10), hence the practical signal amplitude remains difficult to predict. Within this study 1 mm was assumed based on the 3D CAD model (Shown in Figure 4.17). The magnetic field model of Appendix B models the superconductor as a line element with infinitely small diameter. Although the magnetic field of a conductor tape with finite width will quantitatively deviate from the model, the qualitative redistribution mechanism is expected to be similar.

Modelling and the detection analysis has focussed on the single affected strand case, analogous to LTS studies [34]. In case the initial disturbance affects multiple strands at once, fewer superconducting strands will remain which will shorten the duration of the pre-quench region. The intervention period will be reduced compared to the values shown above. To cope with unforeseen quench cases, quench detection design should cope by retaining margin for robustness.

Any quantitative statements concerning the detection or quench behaviour remains delicate, since the model of the last chapter and the 3D model [9] reside on minimal empirical data. Before advancing with quench detection design, the model requires validation. Hence the next chapter presents the test performed with Feather M0.4 and the implemented pick up coil detection.

5

EXPERIMENT

In the previous chapter a HTS quench protection framework including a novel detection method was proposed for future HTS magnets. The main principle of the introduced pick up coil design was already demonstrated by numerical modelling, while this chapter will concern its experimental validation. The test performed with Feather M0.4 aims to study HTS magnet behaviour to validate the numerical models and form a basis for quench detection design. A variant of the detection principle has been implemented to serve as proof of concept (Section 4.3.4). This chapter starts with a brief overview of the experimental setup with emphasis on Feather M0.4, followed by the developed DAQ/Detection system and the measurement procedure. Finally the results are evaluated and compared to the numerical model of Chapter 3.

5.1. EXPERIMENTAL SETUP

The test of Feather M0.4 is performed in CERN's SM18 test station. This test station performs tests of superconducting magnets at temperatures from 4.2 to 80 K with currents up to 20 kA. This section gives an outline of the magnet Feather M0.4 and the test facility. More details on the design of Feather M0.4 and the test station can be found in [6][7] [8] [71].

5.1.1. MAGNET INSTRUMENTATION

An overview of the Feather M0.4 instrumentation is shown in Figure 5.1a and listed in Table 5.1. The magnet is made with 5 meters of Roebel cable, consisting of 15 tapes of YBCO Bruker tape, wound into a 4 turn racetrack coil [8]. The magnet's connection, the magnet leads, exit the magnet at the far end of the coil together with the sensor wiring (Figure 5.1a 11+12). The positive and negative lead, are referred to respectively as the lower and upper lead, based on their vertical transposition, as was shown in Figure 1.2.

Due to the deficient length of total cable the two magnet leads are too short for direct connection with the power supply. Hence two additional roebel superconductor cables are soldered to the magnets leads (Figure 5.1b E+F). These cables are referred to as (HTS) leads, while the two soldered connections are named splices. A calibrated Carbon Ceramic temperature Sensor (CCS) is placed on the right splice to observe the temperature, while voltage taps (Figure 5.1a 11;23 and 12;24) and pick up coils (Figure 5.1a 19;21 and 20;22) are placed on the HTS and magnet lead to monitor respectively the splice resistance and the current redistributions.

5.1.2. DIODE CRYOSTAT

To operate the magnet in its superconducting state, it needs to be cooled below the critical temperature. A stable operating temperature is of great importance, since the critical current density J_c decreases up to 4% per kelvin. Feather M0.4 is tested in the vertical diode cryostat at the SM18 test facility. An overview of the test station is shown in Figure 5.2. The diode cryostat is a 1.6 meter long vertical thermally insulated hollow

Sensor	No.	Location	Side	Figure 5.1a+5.1b
CCS Array	1 × 11	Copper ring	Right	1
	1 × 25	Copper ring	Left	2
Calibrated CCS	1	Copper ring	Top	3
	1	Lower Splice	Right	23
Pick up array	2 × 5	Top inside Former	Left+Right	4+5
	2 × 5	Bottom inside Former	Left+Right	6+7
	1 × 5	Top cap	Center	8
	2 × 1	Magnet leads	Left+Right	19+20
	2 × 2	HTS leads	Left+Right	21+22
Hall Probes	2	Former	Center	9+10
Voltage taps	2	Magnet Leads	Left+Right	11+12
	2 × 2	Cable around heater	Right+Bottom	13+14
	2 × 2	Bottom of HTS lead	Left+Right	23+24
	2 × 2	Top of HTS lead	Left+Right	25+26
	2 × 1	Clamp connections	Left+Right	27+28
Heater	2	Straight Section	Left+Right	16+17
	1	Coil end	Bottom	18

Table 5.1: Overview of the instrumentation of Feather M0.4; The last column refers to Figure 5.1a and Figure 5.1b.

double-walled tube (Figure 5.2b 7). The top of the cryostat is closed by an insert, shown in Figure 5.2c. The magnet is suspended below the insert with a support structure (Figure 5.1b, Figure 5.2a and Figure 5.2c G). The operation current I_{op} is delivered via the insert through the resistive current leads (Figure 5.1b and Figure 5.2c K and L). The sensors are connected to the instrumentation outside of the cryostat via the connector plate (Figure 5.2c I) and current is delivered to the heaters by specific high power connectors (Figure 5.2c II).

To operate the magnet at temperatures between 20 and 100 K a satellite gasifier is used. This vessel is used to deliver $3\,\mathrm{g\,s^{-1}}$ of helium gas of a temperature between 20 and 80 K with a 1 K stability [7]. A schematic overview of the satellite is shown in Figure 5.3a. Liquid helium enters the top (Figure 5.3a 1) and is vaporized by two 500 W heaters (Figure 5.3a 2). The gas is fed to a second heater (Figure 5.3a 3), which heats the gas to the desired temperature. The flow to the cryostat is actively controlled by a valve (Figure 5.3a 4), while the remaining gas is heated up to 300 K before returning to the reservoir (Figure 5.3a 5). The cold gas is delivered to the top of the cryostat (Figure 5.2b 5) and enters via the insert, shown in Figure 5.2c IV. For temperatures below 20 K an additional circuit provides liquid helium at 4.2 K. A heater inside the cryostat is used for liquid evaporation and temperature control (Figure 5.2a P). The temperature of the cryostat and the outlet gas is closely monitored by 8 Cernox sensors placed throughout the cryostat to ensure a stable operating temperature T_{op} of the magnet during test.

5.1.3. High Power Circuit

The operating current is delivered by a 20 kA power supply, with four 5 kA modules in series. A simplified schematic is shown in Figure 5.4. Each module consist of a 3-phase bridge rectifier which transforms the delivered 3-phase current in to a DC current. The output is smoothed by an inductive load before passing through the protection switches, which are explained in the following section.

After the protection switch the current is passed through a water cooled busbar (Figure 5.2b 1) to the current leads of the cryostat insert (Figure 5.2a M+N). The insert leads descend via the lid of the insert, through the insulation and connection plates and arrive inside the cryostat (Figure 5.2aK+L). The current from these leads is delivered to the magnet via the HTS leads. These leads are clamped to the resistive leads with indium to reduce contact resistivity. A contact pressure of 3 MPa is applied using spring washers to minimize resistance while limiting stress on the tape. A copper strip (Cross-section of 15x2 mm) runs along the HTS leads for electrical and mechanical stabilization and to avoid direct contact of the HTS with indium in the clamped joint, which has caused de-lamination in previous experiments.

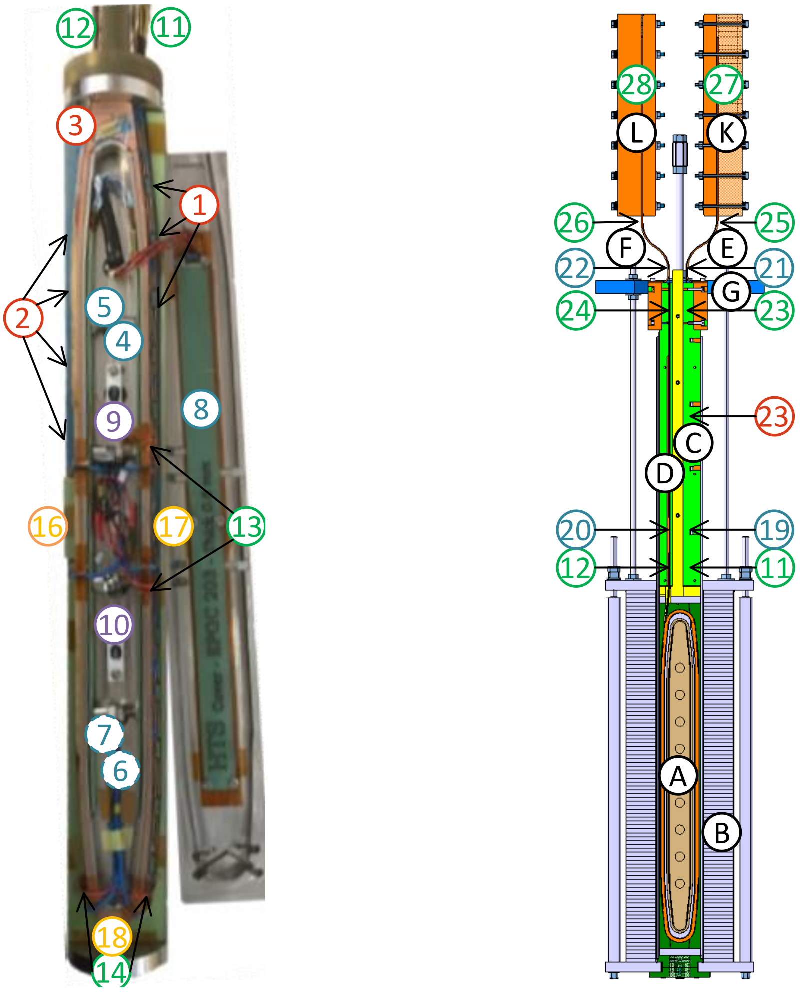

a. Feather M0.4 Sensor layout [7];

b. Cross-section of Feather M0.4 cryostat insert assembly.

Figure 5.1: Feather M0.4 test setup. The sensor numbering refers to Table 5.1. Feather M0.4 includes temperature sensors (red), voltage taps (green), pick up coils (blue), hall probes (purple) and artificial quench heaters (orange). Feather M0.4 (A) is placed inside the an iron yoke (B) and is electrically connected via the splices (C + D) and the HTS leads (F + E) to the copper current leads of the cryostat through a clamped joint (K+L).

5.1.4. DAQ HARDWARE

All sensor signals from the cryostat and magnet are recorded during the test, while a selection of these signals is used for quench detection which runs in parallel. An overview of the sensors in the magnet (Table 5.1) and the cryostat used during the FM0 test are shown in Table 5.2, together with their corresponding Data Aqcuisition (DAQ) system. The acquisition of the measured signals can be divided in two types:

1. State monitoring: Low frequency status monitoring for performance and general parameter monitoring;
2. Quench detection: High frequency status monitoring with the purpose quench analysis for detection design.

Four systems run in parallel during the test of Feather-M0 to perform both state monitoring and quench protection as shown in Figure 5.5. SM 18's original DAQ systems consist of [73]:

1. Quench DAQ (NI PXI-1045);
2. Digital Multimeter or DMM (NI PXI-1044).

The DMM is used for continuous acquisition of temperature signals with low frequency (1 Hz) and monitors the stability of the cryostat during the entire test duration. The Quench DAQ only records data in a certain

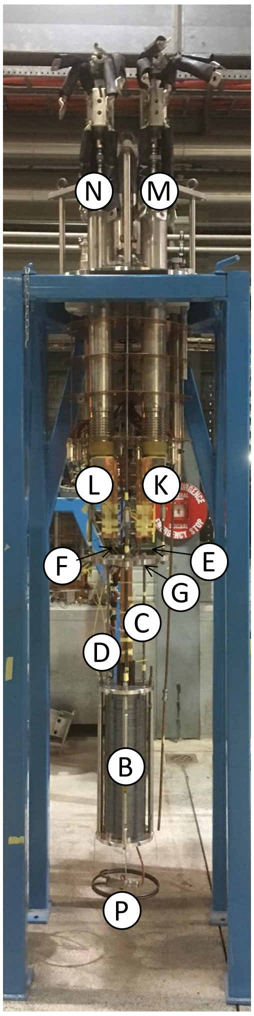

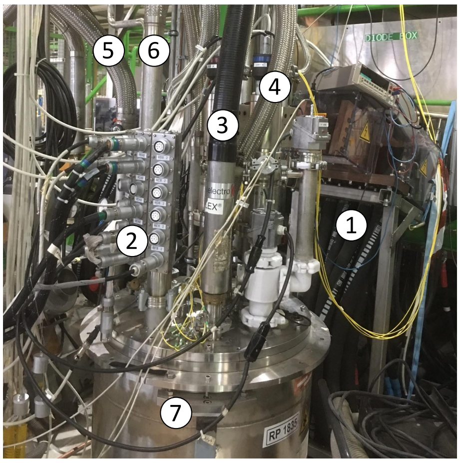

b. Cryostat with Feather M0.4 inside;

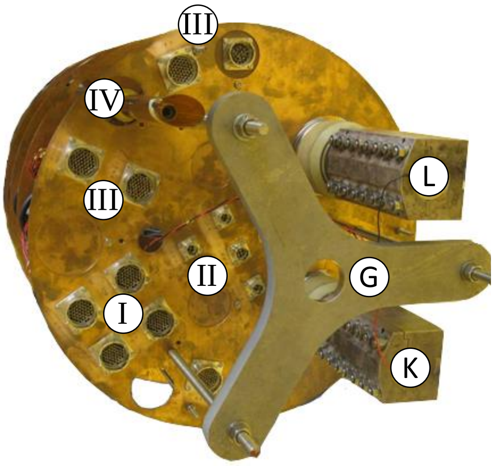

a. Magnet assembly and insert;

c. Bottom view of cryostat insert.

Figure 5.2: Magnet assembly and diode cryostat (numbering agreeing to Figure 5.1): a. Picture of Feather M0.4 (B) assembly (shown in Figure 5.1b) connected to the cryostat insert showing the current supply leads (N-L,M-K) b. Feather M0.4 inside the cryostat (7) with the power supply connection (1), sensor connectors (2), helium gas in/outlet (3/4) and liquid in/outlet (5/6); c. Bottom of the diode cryostat insert (Source: insert report). The current leads (K+L) delivering the current from the power supply, the mechanical suspension (G) and sensor connectors (I,II,III,IV)

time window after it has been triggered (Archive mode), with three frequencies (Low, medium and high frequency: 10 Hz, 5 kHz and 200 kHz). The Quench DAQ is triggered either manually or automatically by the quench detection, which is performed by the Potential Aimant unit (PotAim) (Figure 5.3b F), further discussed in Section 5.2.1.

Data from the optical strain and temperature fibres are measured with a Micron optics SM130. The operation principle of FBG-fibres is found in Section 4.2.1. This device can both acquire data continuously or in archive mode from a maximum of 16 sensors in parallel.

A DAQ system based on a compactRIO-9064 (Figure 5.3b A) is developed for quench detection and acquisition of all the remaining sensors. With 7 NI 9205 modules, this system is able to acquire a total 224 analogue signals simultaneously with a maximum aggregate acquisition rate of 250 kS/s per module [74]. One NI 9401 DO-module is used for control of the heaters, synchronisation and protection trigger purposes. A more detailed description of the cRIO hardware and its programming can be found in Appendix E.

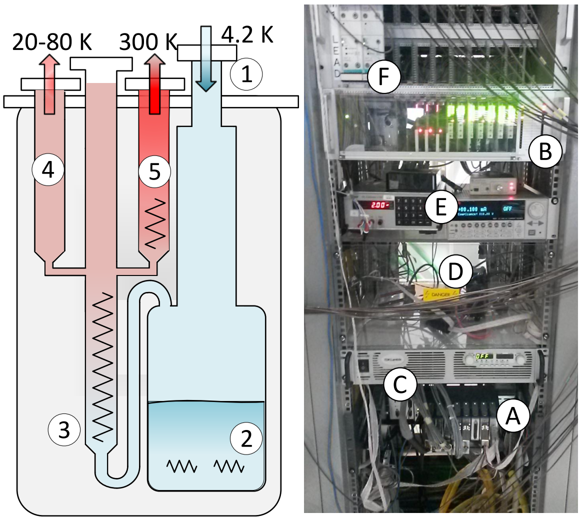

a. Satellite gasifier;

b. Quench Detection and DAQ of Feather M0.4 Test.

Figure 5.3: Test station setup: a. Satellite gasifier for operating the magnet between 4.2 K and 80 K. The liquid helium enters the top (1), where it is vaporized (2) and heated up to the desired temperature (3). The flow is actively controlled by a valve (4) based on the temperature inside the cryostat. The remaining gas is heated up to 300 K before returning to the cryogenic facility. b. Quench detection and acquisition hardware. The cRIO (A) performs the DAQ and quench detection of all non-voltage sensor signals, while the Potaim (F) performs the voltage quench detection. If either of the systems identifies a quench, the safety matrix (B) is triggered. The artificial quench heaters are powered by DC power supply (C) and controlled via the relais (D) by the cRIO. The three current supplies (E) deliver the power for the CCS, CCS array and hall probe sensors.

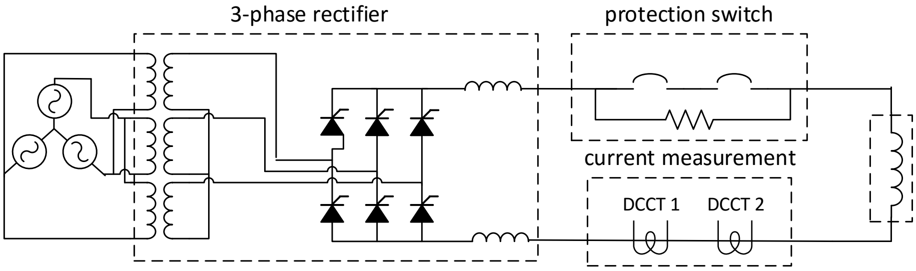

Figure 5.4: High power circuit schematic[72]. Power supply with 3-Phase power rectifier with inductive load, protection switch with dump resistance, the magnet and current measurement through two Direct Current-Current Transformers (DCCT).

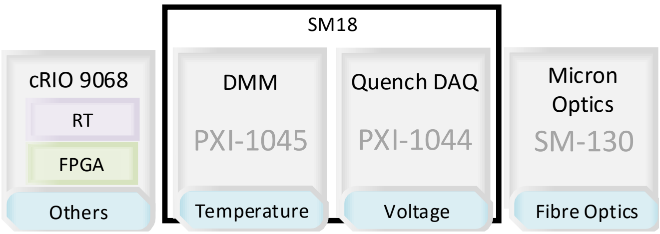

Figure 5.5: Data acquisition systems during Feather M0.4 test: Standard LTS magnet test DAQ DMM and Quench DAQ and the specialized NI cRIO 9068 and Micron Optics SM130.

	Sensor	Number	DAQ Freq	cRIO	DMM	Quench DAQ	Micron Optics
Magnet	CCS Arrays	2	100 Hz	×			
	CCS (Calibrated)	2	100 Hz	×			
	Pick up array	5×5	10 kHz	×			
	Hall Probes	2	10 kHz	×			
	Voltage taps	8	200 kHz			×	
	Optic fibres	2	1 kHz				×
Cryostat	Cernox	8	1 Hz	×			
	Optic thermometer	1	1 kHz				×
	Optic strainmeter	1	1 kHz				×

Table 5.2: Overview of sensors and accompanied data acquisition of Feather M0.4 test.

Sensor	Current supply	Operating current
Calibrated CCS	Keithley 6221	100 μA
CCS arrays	Knick DC Calibrator j152	2 mA
Hall Probe	Lakeshore 120	100 μA

Table 5.3: Calibrated current supplies for 4-wire measurement (Figure 5.3b.

SYNCHRONISATION

Since the data acquisition is performed on four separate systems, synchronisation is of great importance for reconstructing the events preceding and during a quench. Apart from Network Time Protocol synchronisation, which is approximately accurate up to 100 ms [72], hardware synchronisation triggers were used to enhance synchronisation. An overview of the different synchronisation signals is shown in Figure 5.6.

The fibre optics measurement is started and stopped by a signal from the cRIO using a block wave (Figure 5.6, SO). Since both systems perform acquisition on NTP time basis, coarse synchronisation is done using NTP, while precise synchronisation (<10ms) is enabled via the hardware trigger.

The Low Frequency-module (LF) of the Quench DAQ and the DMM are primarily used for temperature acquisition and have sample frequencies of respectively 100 ms and 1 s. Hence the accuracy of Network Time Protocol (NTP) synchronisation is for these systems is sufficient.

Conversely, the Medium Frequency (MF) and High Frequency (HF) module are operated solely in archive mode. Acquisition of the data is performed after an external trigger signal is received from either the PotAim or the power supply. An additional trigger from the cRIO quench detection system was used to trigger the MF and HF archive acquisition (Figure 5.6, ST). All triggers are logged in the quench cRIO during operation, including the trigger from the PotAim quench detection. The synchronisation between the systems was verified within 10 ms.

MEASUREMENT SETUP

Main concern in designing the measurement setup for a quench detection system is reducing noise. The selected measurement scheme of the compactRIO is shown in Figure 5.7. The measurement equipment and power supplies are floating while the cryostat is grounded for safety reasons. The signals are measured in differential mode with smallest possible measurement bandwidth (± 0.2, 1,2, 10 V) to enhance the signal resolution, while divided evenly over the different modules, in order to employ the maximum aggregate acquisition rate. Each module is dedicated to a single sensor type and all idle input channels are short circuited to reduce their capacitive crosstalk.

The sensor cabling both in and outside the cryostat are affected by changing electromagnetic fields, for example caused by instability of the power supply. Shielded twisted cables are used for every signal between the cryostat and the cRIO, while inside the cryostat twisted cables were adopted. The cable lengths are kept as short as possible and the minimum amount of connectors where used. The sensor signal and 4-wire sensor power supply cabling was separated. The current supplies (Figure 5.3b D) used for each sensor and their operating current is shown in Table 5.3.

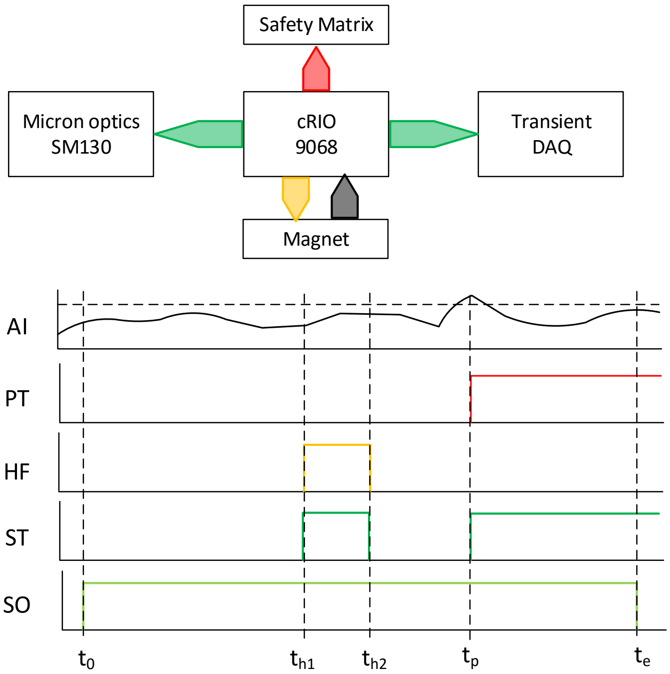

Figure 5.6: Synchronisation signal overview: Signal acquisition AI during t_0 and t_e, the protection trigger PT when the threshold is exceeded at t_p, heater fire HF between t_{h1} and t_{h2}, Transient DAQ synchronisation trigger ST during heater fire/protection trigger and optic fibre synchronisation signal SO during whole acquisition period.

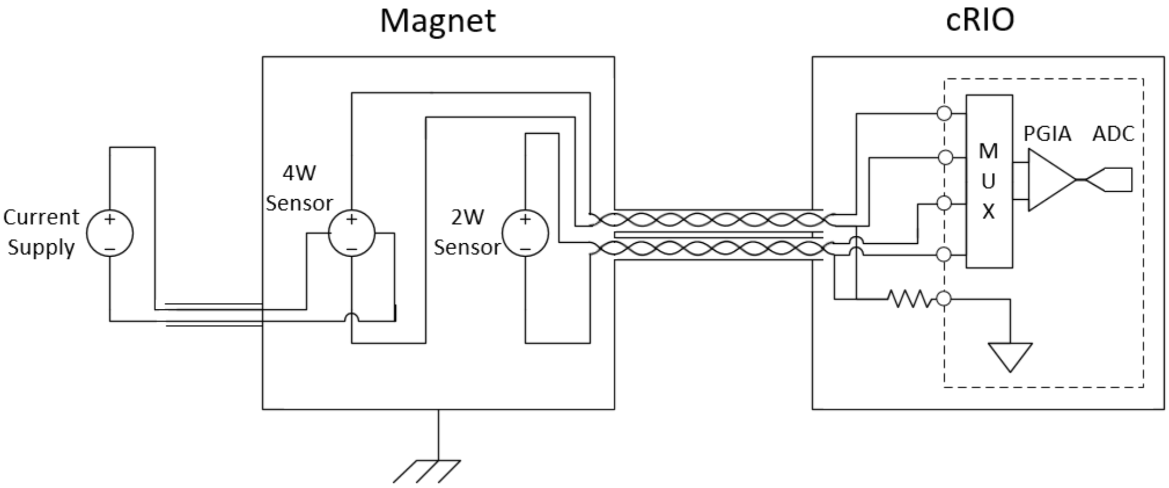

Figure 5.7: Measurement setup cRIO: All sensor wires are shielded twisted pairs, which connect the grounded shielding of the magnet with the floating cRIO. The cRIO, since the NI-9201 input module consists of a multiplexed (MUX) digital analogue converter (ADC), all signals are connected to the module's ground reference. 4-Wire measurements, such as hall probes and CCS use separate shielded wires for sensor current supply.

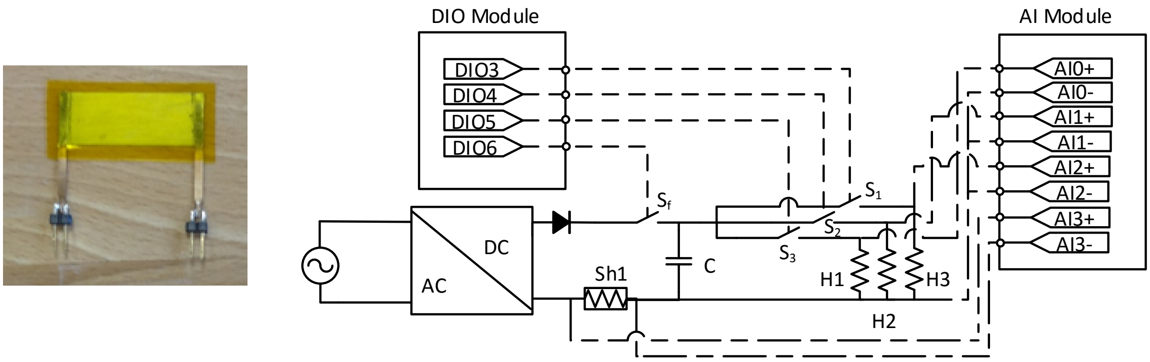

a. Quench heater; **b.** Schematic overview Quench heater circuit

Figure 5.8: Quench heater and a schematic overview of the heater circuit. a. The heater consists stainless strip insulated with Kapton. b. Heater circuit. High power circuit (Thick lines) and measurement and control (Thin lines) of the heater circuit. The cRIO output module controls the power through the three heaters (H1,H2,H3) via the 4 relais (S_1, S_2, S_3 for activating each heater and S_f for discharge). The power is delivered by the GEN3300W DC power supply through a 10 µF capacitor (C). Current is measured via a calibrated shunt (Sh1) and voltage is measured directly by the cRIO input module.

PROTECTION

The current supply should be switched off in case of a quench to avoid excessive Joule heating. A thyristor and mechanical relais are placed in series for redundancy (Figure 5.4), respectively for their switch velocity and reliability [18]. The cRIO is connected to the electronics controlling the power supply and protection switches, called the safety matrix(Figure 5.3b B). After a quench is detected, the magnet is decoupled from the power supply within 30 ms. A resistance of 70 mΩ is placed in parallel with the switches to mitigate the effects of a quench. When the protection is triggered, both thyristor and mechanical switch open and the remaining current will dissipate in the dump resistor.

QUENCH HEATER

Quench heaters are implemented in the magnet to artificially start a quench, as was shown in Figure 5.1a indicated by 16-18. The heaters consist of small stainless steal strips as shown in Figure 5.8a, directly applied on the coil winding. The quench heaters are controlled from the output of the cRIO via four solid state relais as shown in Figure 5.8b. A TDK Lambda GEN3300W DC power supply (Figure 5.3b C) delivers the power to the heaters (max. 150 V, 22 A). Both voltage and current are measured to determine the applied heater power to empirically determine the MQE of the magnet after a artificial quench caused by the heater.

5.2. QUENCH DETECTION

The overall goal of the test is to compare the performance of the different detection systems during controlled quench. A total of 36 signals can be used for the quench detection of Feather M0.4 performed by the PotAim and cRIO system in parallel. The two systems are briefly discussed in more detail subsequently in this section.

5.2.1. VOLTAGE

Voltage protection is performed by 8 PotAim-units with a total of 16 detection channels. The layout of the PotAim detection system is shown in Figure 5.9. Either single ended signals or differential signals can be treated, which are filtered to reduce the noise level. Subsequently the signals divided by a factor 100 and passed through a galvanic insulation inside the amplifier, to protect the detection circuit from electric breakdown. After the insulation, the signal is amplified and compared with a pre-set threshold. When the threshold is exceeded an analogue clocks times the period. If the period passes the pre-set time window, the quench detection triggers the safety matrix.

The amplifier gain, threshold and time window for each channel of the PotAIM quenc detection during the Feather M0.4 test is shown in Table 5.4. Note the gain is including the division by 100 mentioned above.

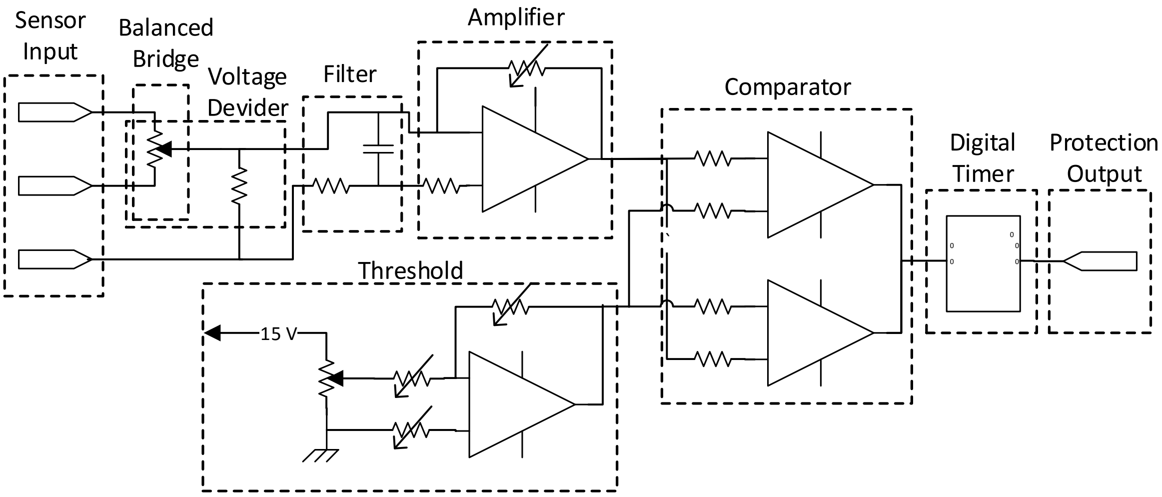

Figure 5.9: Schematic overview of analogue electronics inside PotAim. The differential signal enters the PotAim via a balanced bridge (discussed in Section 4.4.2), via a voltage divider and filter to a amplifier with galvanic insulation. The signal is compared with the defined threshold and if the threshold is exceeded the digital timer starts counting. When the counter reaches the detection window, the protection is triggered.

Signal	Gain	Threshold [mV]	Window [ms]	Description
Vdiff0	0.1	11	20	Full magnet balanced over heater 2
Vdiff1	0.1	10	20	Full magnet with splices balanced over heater 2
Vdiff2	10	1160	30	Full magnet with splices balanced over heater 2
Vsum1	4	71	30	Full magnet with splice and leads
Vsum2	0.04	-	10	Full magnet with splice
Splice1	40	10	10	Splice 1
Splice2	40	20	20	Splice 2
Cable1	40	5	20	Positive magnet lead to heater 1
Cable2	40	3	10	Over heater 1
Cable3	40	3	10	Heater 1 to heater 2
Cable4	40	3	10	Over heater 2
Cable5	40	3	10	Heater 2 to negative magnet lead
VgazA	40	60	10	Positive resistive cryostat lead
VgazB	40	60	10	Negative resistive cryostat lead
VconA	40	10	10	Positive clamp to HTS lead
VconB	40	10	10	Negative HTS leads to clamp

Table 5.4: PotAIM voltage quench detection channel overview. All signals listed are used for voltage detection. The signal and threshold are amplified by the listed gain in the amplifier of Figure 5.9 before comparison. The time window represents the period for which the threshold is exceeded before the protection is triggered.

The presented threshold value excludes the amplification, hence the threshold corresponds to the unaltered sensor signal.

5.2.2. cRIO

The NI compactRIO 9068 was programmed for embedded quench detection and monitoring of all non-voltage signals in the magnet. The cRIO 9068 combines a dual core ARM Cortex A9 processor running a Real Time operating system and a Artix-7 Field Programmable Gate Array (FPGA). The Real Time processor of the cRIO can perform deterministic tasks with a clock speed of 1 MHz, while the FPGA chip offers the flexibility to perform rapid prototyping on a hardware based platform. The FPGA can perform true parallel operations at a clock speed of 40 MHz. Due to the hardware implementation, FPGA programming requires understanding of the internal structure of the chip. The interested reader is referred to Appendix E for an overview of the DAQ

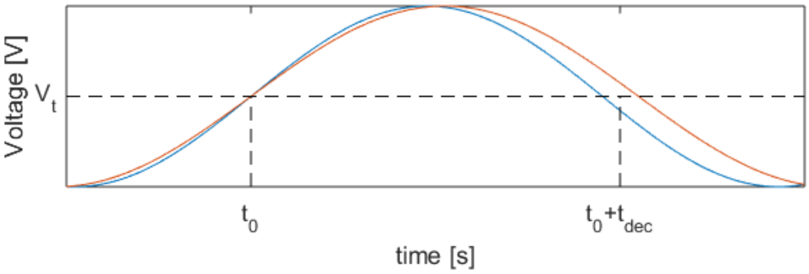

Figure 5.10: Validation of the quench detection method: A sine wave is generated by a NI-6001 device and connected to one of the inputs of the cRIO. The sine wave is offset by the detection threshold V_t, while its period is varied. If half of the sine's period T is smaller than the detection window t_{dec} (blue curve), normal operation continued. Contrarily, if $T/2$ exceeds the window (red curve), the protection should be triggered. The detection was validated at various t_{dec} and V_t within 0.5 ms accuracy of the time window.

and quench detection software or to [74] for more information concerning cRIO programming and hardware in general.

The NI cRIO-9068 was programmed to perform quench detection on 34 channels in parallel. The core detection algorithm implemented in the FPGA is similar to the PotAim (Figure 5.9):

The input signal is averaged by a block average filter, with the ability to average signals over 4, 16 and 64 samples. If the average exceeds the predefined threshold, a digital counter times the length period the threshold is violated. After the time window is passed, the protection is triggered.

The detection settings for each of the channels can be configured separately from the host computer. Implementation of the detection has been validated using a NI-6001 as a precise signal generator, the validation method is shown in Figure 5.10.

The cRIO program offers an fully integrated data acquisition and detection system which is controlled and monitored from a remote location (Host). The interface on a connected computer allows monitoring of the current state of the DAQ and detection system in real time. Potential quench data is displayed after the heater is fired or the protection is triggered for easier post analysis. The state and tasks performed by the FPGA and RT are logged automatically for easier trouble shooting and data review.

The raw measurement data is stored in binary files for minimizing utilization of the RT processor. Readout of data by programs other than Labview is facilitated using the built-in conversion tool with compatibility for TDMS, TXT or CSV formats. An example of the converted data is shown in Appendix F.

5.3. MEASUREMENT PROCEDURE

The main goal of the Feather M0 test is gaining insight in its quench behaviour while limiting the operational risk. Earlier HTS magnet experiments have experienced uncontrolled thermal runaways with as result a premature end of both the test and the magnet [22]. Based on the numerical model, the voltage quench detection is only expected to offer sufficient protection at low current densities, while the pick up coils have been solely validated based on numerical results. Hence a controlled environment is needed to test the performance detection and protection on Feather M0.

The test of Feather M0.4 starts with validating the overall test conditions. After the magnet has reached its operating temperature domain, all sensor readings and insulation values are probed before current is applied to the magnet. This test at low current includes verifying the superconducting state and quantifying the resistances of the resistive joints. This way the model parameters can be verified and potential risks identified. Since the initial run is standardized for all prototype magnet tests, it is of limited interest for the HTS quench behaviour study.

In Chapter 3 the effects of the quadratic current proportionality of the magnetic energy were shown. At high operating temperatures (> 40 K) the critical current density J_c is relatively low (Figure 5.11). The dissipated power in the normal zone is therefore limited, reducing the risk while allowing more time for intervention. As been considered in Chapter 4, the voltage detection should be adequate for protection in this operating

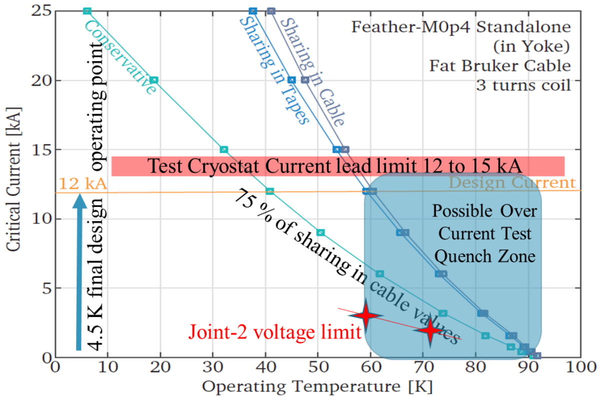

Figure 5.11: Expected critical current I_c versus operating temperature T_{cs} [7] based on the tape's theoretical load rating. The critical current depends on the assumptions made, either if the current is shared over all tapes or only within the tape. Since de-lamination of the tape was observed during cable manufacturing, 75% of the cable sharing value is adopted as target. Based on the expected MQE and the power rating limit of the heaters is expected to artificially quench the magnet only at higher temperatures.

domain. Moreover, the performance of the pick-up detection is expected to increase for higher currents, due to its current proportionality of the signal. The performance of this detection method should be explored throughout its operating domain. Hence, the operating temperature should be gradually decreased to explore higher energy domains, while limiting the overall risk by relying on the voltage quench detection in parallel.

A quench can be initiated by running the magnet locally over its current density J_c, which is referred to as natural quench. The risk of this method is the lack of controllability of this superconductor property. During the ramp up the quench detection is influenced by inductive voltages and electromagnetic field disturbances, as was discussed in Section 4.2.2 and Section 4.4.3. Hence controlled quenching and repeatability of the event is challenging. Heaters are used instead to initiate a controlled quench. This way protection measures can be taken out of precaution after a 'safe quench window', even if no quench signal is detected. The time window is based on numerical results and aims to gather quench data without risking to damage the magnet. When the heater is fired and the time window has past, the protection is triggered as a safeguard.

To initiate a quench artificially using one of the heaters, the MQE should be locally lower than the energy provided by the heater. Since the heater has only limited power, it is only able to artificially quench the magnet in a domain shown in Figure 5.11. Care has to be taken during ramp up of the magnet, since local degradation can still cause uncontrolled natural quenches.

The data gathered during the test will offer insight on the practical quench behaviour and provide validation of the numerical model. The detection algorithm of the cRIO can be reconfigured based on the acquired results accordingly. The detection performance is verified by reproducing the test conditions with the protection safeguard active. If the algorithm detects the quench, the test is repeated at slightly lower temperature to check its resilience. The temperature steps should be kept limited to 1-2 K to minimize risk, since the quench energy rises rapidly together with the operating current. If the detection failed, a new detection concept can be based on the newly gathered data. By performing multiple empirical iterations a better insight is gained for building a reliable quench detection.

5.4. RESULTS

Feather M0.4 was tested at various currents and operating temperatures during several test runs. The initial test plan had foreseen two subsequent test runs: The first run served as verification of all instrumentation, the stability of the cryogenic facility and the quantification of the resistive joints. The second run aimed to study the magnets behaviour at higher currents for quench detection design. Due to a misbehaving splice resistance during run 2, it was preliminary terminated. After measures were taken including revising the cooling of the splice, the revised set-up was retested in run 3. The various runs are discussed subsequently in more detail.

	RnΩ	
Connection	50 K	70 K
Cryostat current lead	100	170
Joint	<10	< 10
Splice	<10	< 10

Table 5.5: Result Run 1 joint and splice resistance measurement [7]

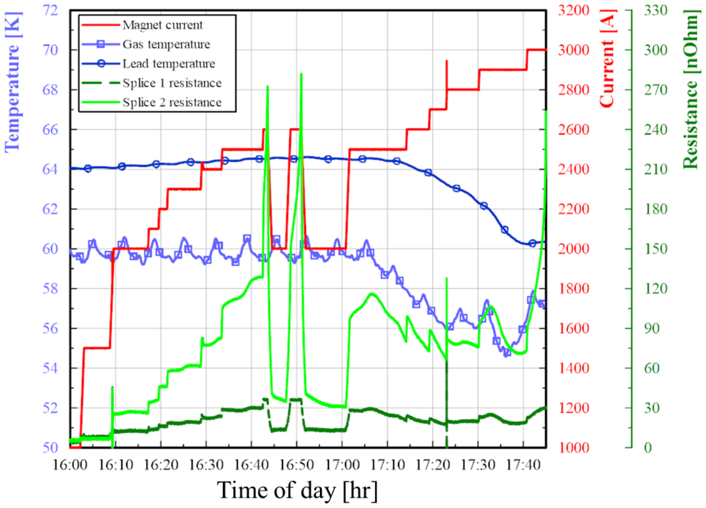

Figure 5.12: Repetitative slow thermal runaway of Splice 2 during run 2 at constant current: The resistance of Splice 2 rises rapidly with each current increment at high current density. [7]

5.4.1. RUN 1

Test run 1 aimed for validating the superconductivity of the magnet and to check if the data acquisition and protection system were operational. Apart Feather M0.4 itself, it was the first operational task for the cRIO data acquisition. After cool down all instrumentation remained operational and measured values were within expected ranges. The sensor readings of the temperature sensors were confirmed with the data acquired by the DMM. The temperature stability of the cryostat was verified and the critical temperature of magnet was found near 100 K. A 600 A power supply was used for powering the magnet, since the larger 20 kA supply was in high demand of other tests which ran in parallel. Several tests, including a RRR and splice and joint resistance measurement were performed at low current at 4.2 K to parametrize the magnet. The resistive connection test results are summarized in Table 5.5.

5.4.2. RUN 2

After studying the data of the run 1 and a thermal cycle upto room temperature, run 2 constituted the performance test of Feather M0.4 at high power. The 20 kA power supply of Figure 5.4 was connected and the behaviour of the magnet between 50 and 70 K was studied. The first test coped with a slow thermal runaway at the splice joint at approximately 60% of the expected J_c. The resistance of Splice 2 (Figure 5.2a C), which was well behaving at low currents, showed a clear increase in resistance for higher currents. Figure 5.12 shows the gradual runaway of Splice 2 resistance (light green curve at 16:44) at 2600 A and 60 K. After manual current ramp down the resistance runaway of splice 2 was reproduced at 16:51, showing identical behaviour.

In an attempt to study the failure mode, the temperature was gradually decreased at constant current near the runaway. Note the gradual resistance increase between 17:00 and 17:05, which shows a significant decrease after the temperature is lowered by less than 1 K. Subsequently at 57 K, a current of 3200 A was reached before the runaway behaviour was observed.

The attained currents in Run 2 are shown in Figure 5.13 versus the operating temperature. Since Splice 1 shows the same but less drastic resistance behaviour (Dark green in Figure 5.12), both splices were revised.

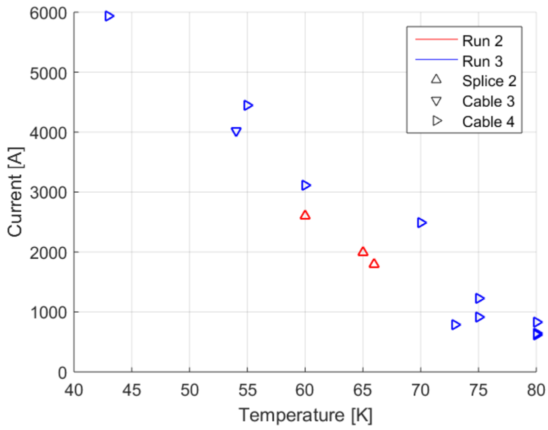

Figure 5.13: Reached operation currents versus temperature during run 2 (red) and 3 (blue). The cooling measures taken have a clear effect on the critical current I_c.

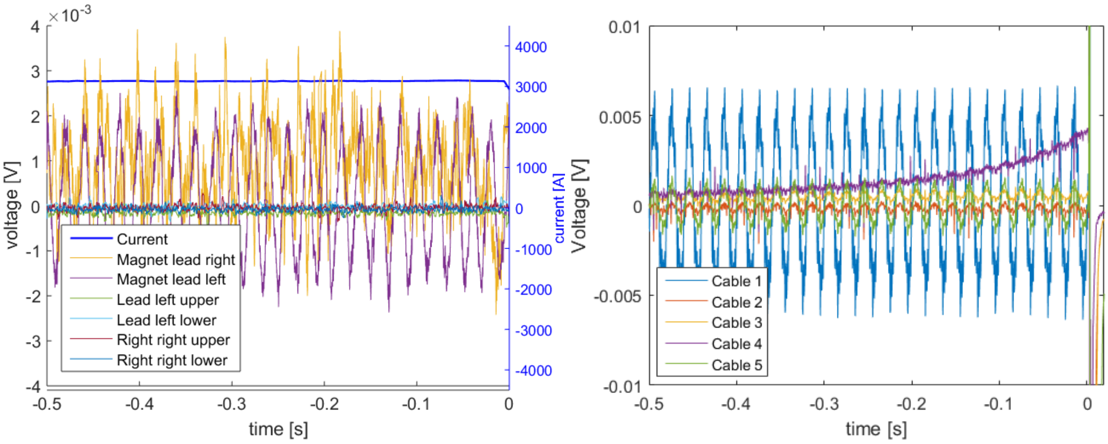

a. Pick up coil signals

b. Voltage signal

Figure 5.14: Experimental results preceding a quench of a cable section inside the coil at 4012 A and 55 K. Pick up coil signal measured by the cRIO (left) and voltage signal from the QuenchDAQ (right) before the protection was triggered at $t = 0$.

Liquid helium cooling (at 4.5 K) was redirected to pass along both of the splices, aiming to attain a locally lower operating temperature at the splice, while keeping the overall cryostat temperature stable.

5.4.3. RUN 3

Stability of the cryostat temperature remained to be challenging, due to the heat diffusion via the copper parts to the magnet's inside or convection to the cryostat's atmosphere. After a transient a stable temperature could be attained, with both splices approximately 10 K lower than the rest of the magnet. Despite of the delicate temperature stability caused by the operation of two cooling system in parallel, the critical current was improved. The critical currents versus operational temperature are shown in Figure 5.13. The operational temperature is taken as average of the temperature gradient caused by the introduced splice cooling. In contrast to run 2, the splices were not limiting the magnet in its maximum operating current and most quenches occurred within the magnet.

To study the data measured by the cRIO during a quench, the quench event at 4012 A, 54 K is considered in greater detail. All measured signals leading up and during the quench are shown and discussed in detail in Appendix F. Several signals preceding this quench have been extracted and shown in Figure 5.14a and the corresponding voltage signals measured by the Quench DAQ shown in Figure 5.14b. The quench was detected

	High freq Noise	50 Hz	
Pick up coil	HTS leads	±3	< ±1
	Magnet leads	±3	±2
	Inside former	±3	±4
	Magnetic	±5	±8
Hall probe		±2	NA
CCS	Copper ring	±4	-
CCS Array		±100	-

Table 5.6: Noise levels observed during the test (Appendix F.0.1)

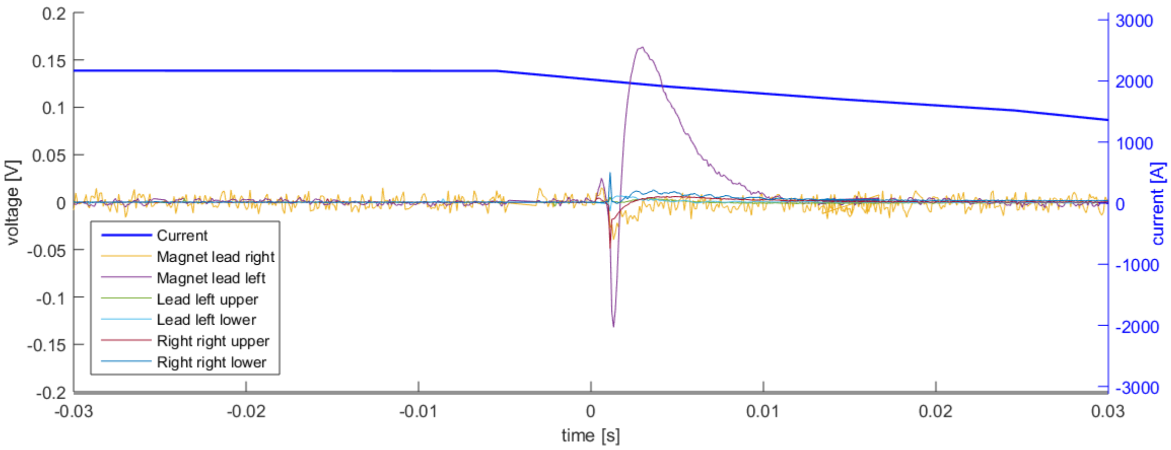

Figure 5.15: Experimental results from the measurements of the pick up coils during a quench of a cable section inside the coil at 4012 A and 55 K and the subsequent quench and current extraction (blue). These signals are discussed together with various other signals measured by the cRIO in Appendix F.

and triggered by the PotAim voltage detection during a current ramp-up 20 kA s^{-1}. The voltage measured over one of the cable segments (Cable 3) shows a gradual rise over more than half a second upto 10 mV, triggering the protection at $t = 0$.

Based on the signals from the pick up coils no precursor of the upcoming quench was recognized. A signal is measured during the quench and the simultaneous current extraction, as shown in Figure 5.15. After the inductive effects at $t = 0$, a decaying signal is observed. The observed noise levels precedent to the quench are summarized in Table 5.6. The complete set of signals measured by the cRIO preceding and during the quench are presented and discussed in Appendix F.

Attempts to artificially quench the magnet using the heaters have not been successful. The current was increased upto 850 A at an operating temperature of 75 K, while the magnet prior to this test already naturally quenched at 780 A at similar temperature. After firing the heater at maximum power (measured 117 W for a duration of 0.2 s), the magnet remained superconductive.

5.5. CONCLUSIONS

Although Feather M0.4 has reached high currents densities, validation of the quench detection system and the modelling was not possible based on the acquired data within the duration of this report. The measurement setup and data acquisition have been able to acquire data with desired frequencies over more than 12 hours continuously, while the acquisition systems have proven to be synchronized within a window of 10 ms.

Attempts to artificially quench the magnet using the heaters have not been succesful. Although the heaters exceeded the MQE according to the numerical model (Section 3.3.7) and emperically single tape quench [21] by a substantial margin, no irregular behaviour was observed from any measurement signal. Hence the heaters were not capable to heat the conductor to cause a measurable normal zone within their maximum power rating. Although the magnet has naturally quenched, the modelled quench studied in Chapter 3 was not possible to reproduce in reality.

A natural quench is expected to develop significantly slower compared to the quench caused by local disturbance, which was studied in Chapter 3. The longer quench duration allows the the heat to diffuse over the cable, resulting in slower current redistributions. Hence, the signals measured with (sub-)millivolt noise could not identify any current redistributions precedent to the quench. Therefore the test conditions did not allow validation of the pick up sensor design and detection algorithm.

5.6. DISCUSSION

The cause of the resistance drift at high current densities is not possible to allocate exactly from the test data. While the joint behaves well at low current, the voltage rises sharply when the current increases. Local degradation of the superconductor at the splice is most likely, considering the observed temperature sensitivity. Optical inspection revealed no abnormalities, hence future dismantling of the splice should offer more insight in the defect. Since both splices show similar issues, the soldering of the splice should be reviewed before building its successor.

The splice cooling measure has introduced an extra degree of freedom which interferes with the cryogenic stability. Apart from the stability of the entire cryostat, which is well monitored by several temperature sensors, a gradient could originate within the magnet. Since the temperature within the magnet is only measured with a single calibrated sensor, the local operating temperature of the conductor is merely known. Reproduction of a quench event is not possible, which is seen in the large scatter of measured critical currents I_c.

The measured I_c is merely representative for the short sample current of the cable. The I_c is likely to be inhomogeneous throughout the cable, due to degradation during cable manufacturing or winding, and temperature gradients, introduced by the additional splice cooling. Nonetheless, a natural quench occurred in two different parts of the magnet, which could indicate the I_c of the short sample length is nearby.

Control of the heater energy to artifically quench a magnet has already been proven challenging in the past [21]. The duration and heating power are difficult to control, due to the losses in the wiring, the thermal capacity of the heater and the thermal insulation with the magnet's winding. Nevertheless the applied power (117 W) should easily trigger a quench in the magnet especially at high operating temperatures (75 K). No signal was observed in any sensor, while the optic fibre sensors were able to see a strain/temperature change caused by a heater pulse at room temperature. Causes could either include bad contact between heater and coil, resulting in slow and gradual diffusivity, or even short circuit. With the magnet still in the cryostat, it is challenging to identify the cause, since the connecting cable's and the heater have comparable resistance.

The test conditions did not allow to validate the implemented pick up quench detection, despite of the low measured noise levels. The quench pick up coils should allow identifying the current redistributions during the prequench as shown in Figure 4.21 even at low current densities. Due to the lack of quench signals, reconstruction of the quench development is problematic. The gradual increase of resistive voltage indicates a gradual temperature rise of the conductor, allowing time for the heat to diffuse over the whole cable. The low current density is expected to cause lengthy current redistributions with low amplitudes, which are difficult to distinguish from the noise and inductive effects caused by the ramp up. Validation of the detection requires either natural quenches at higher current densities should be performed, which poses higher risks to the magnet's integrity and runs into the facilities limits of 12 kA, or the ability to artificially quench the magnet.

CONCLUSIONS

The aim of this study on quenches in HTS multi-strand cable was to explore the possibilities of quench detection design in future HTS magnets. Quench behaviour can be characterized by the cable's stability, which is described by the coupling between current and thermodynamics when subjected to local disturbances. The stability of HTS cables is studied for the design of compliant quench detection, able to cope with both variations in operation conditions and magnet properties.

The study of the electrodynamics within non-insulated multi-strand cables has provided a dimensionless analytic description of the current redistribution behaviour following a constant quench resistance. The ability to redistribute, which relates directly to the cable's stability, was parametrized by several time constants.

In an effort to describe the thermal-electric behaviour, a 2D HTS cable quench model was introduced. Although considerably simplified for optimising its efficiency, it showed satisfying resemblance of the behaviour compared to other models. The stability of HTS cable as function of several parameters including current density was studied and showed analogy with the behaviour of LTS cables.

High current densities are accompanied by reduced stability and sudden thermal runaway posing high demands for quench detection. Numerical simulations showed conventional voltage detection is inadequate to detect quench timely allowing for intervening measures to take effect. Based on the insight gained from several analytic descriptions and numerical simulations, an optimised pick up coil geometry and positioning was introduced for quench detection in HTS cables to cover these demanding operating conditions. The onset of a thermal runaway is recognized by capturing the local magnetic field variations due to current redistributions between the strands of the cable preceding a quench. Numerical simulations shows the precursors appear well before the thermal runaway develops, hence allowing sufficient time for intervention. This detection principle is implemented in the sensor design for quench detection of Feather M2.

In an effort to proof its concept and validate the numerical model, a truncated design was implemented in Feather M0.4. The magnet test was not capable to validate the quench detection due to malfunction of the quench heaters. Hence it was not possible to reconstruct quench caused by local disturbance, hindering the empirical validation of both quench model and detection design.

The embedded system for quench data acquisition developed during the project recorded the behaviour of Feather M0.4 during several natural quenches while synchronised within 10 ms with the other acquisition systems. The functionality of the first iteration of the quench detection algorithm was validated. Production of Feather M0.5 and Feather M2 are launched including the full quench detection design, which aim respectively for validation of the quench detection and exploring the 16 to 20 T range accelerator dipole field.

RECOMMENDATIONS

The following recommendations are offered for future related research in the field of quench detection for HTS applications:

- Experimental validation of the cable quench behaviour during a controlled thermal runaway is required for both detection sensor design and validating quench models. Functional quench heaters, or another artificial disturbance source, are recommended to gain insight in the quench behaviour following a local disturbance within a controlled environment. Hence, the artificial quench heater design should be further developed to enhance its reliability.
- If a quench signal preceding a quench can be identified from the pick up signals, the performance of the pick up sensors should be explored within the full operating domain. Based on the performance of the implemented detection subsequent detection design iterations can be made.
- The phenomena of cable quench requires more fundamental empirical studies, due to the extensive number of uncertainties. The quench behaviour within Feather M0.4 is complex and too challenging to quantify based on the available signals. Short sample measurement could offer an outcome, which reduces the complexity while offering controlled test conditions. In particular the prequench behaviour is of interest for model validation and detection algorithm design.
- In the absence of empirical validation, numerical simulations should focus on qualitative understanding of the phenomena's behaviour instead of detailed modelling. The exploration of model parameter in this report has specifically focussed on the Feather M2 properties and operating conditions. Further study should aim for a more general approach for the protection of HTS magnets. Analytic and numerical models should attempt to capture the stability into scaling laws, such as the suggested MQE as function of $r\eta$, to qualitatively gain understanding in its complex behaviour.
- The protection coverage of the operating systems by voltage and pick up coil detection systems was discussed. In order to offer HTS quench detection for general applications, the performance of both systems and their limits in the full magnet operating regime should be quantified.
- Based on the numerically found MQE and its dependency on duration and spatial distribution, possible HTS quench causes can be evaluated. Understanding of the quench source should be studied as its behaviour gives insight in the onset of quench, which helps to improve quench detection.
- As been shown during the experiment, resistive joints present a weak point and should be reduced to a minimum. However, since resistive joints in superconductor magnets are inevitable (e.g. power supply), more extensive study is required in order to minimize its deficiency and to understand its possible failure mechanisms.
- This report has focussed itself mainly on the electrodynamics during a quench, while the spatial adiabatic thermal diffusivity behaviour has only been considered briefly. Study of the thermal propagation requires more extensive 3D modelling and dedicated experiments on cable samples, including the local magnet geometry.

ACKNOLEDGEMENTS

With this statement I would like to thank my colleagues for the inspiring coffee breaks, discussions, debates and friendly disputes.

First I would like to thank my supervisors, **Glyn** and **Gijs** for offering me this opportunity. Within these 10 months I have learnt more than I have ever held possible. Thank you for supporting me!

Fred van Keulen,
who has advised me to look for student vacancies at CERN and has supported me throughout the process. Thank you for your enthusiastic assistance during the many Skype meetings we have had!

Stefanie,
thank you for acting as intermediary, with your help I was able participate on this project!

Jeroen,
this work was absolutely not possible without your support. Thank you for keeping your patience after all the questions I have asked!

Jaakko,
apart from being a great colleague with a unique sense of humour, I enjoyed running through the fields and of course the orienteering!

Lucio,
grazie mille for this great possibility to work in this group. It was an honour to work as a technical student on this amazing project.

Adriaan and his team,
thank you for assisting me in programming the cRIO. I have learnt a lot from your expertise and could definitely not have done it without your help.

Luca Bottura,
thank you for your patience in helping with the analytic equations. I am impressed about your expertise and it was a pleasure working with you.

Hugo Bajas,
nous avons eu maint discussions, mais avec un très bon résultat! En néerlandais: Sans friction, il n'y a pas de brillance. C'était agréable de travailler avec toi!

Francois Olivier,
j'ai de l'admiration pour ton expertise, qui s'est confirmé avec l'assemblage de Feather M0.4. Je suis content j'ai pu contribuer et je veux te remercier pour notre collaboration. Je suis désolé que nous n'avons pas pu parler Français plus souvent!

Frederic,
j'ai travaillé avec plaisir avec toi. Merci pour tout l'aide pendant la fabrication, le câblage et l'installation du systeme d'acquisition.

Jerome Feuvrier,
merci pour ton aide pendant l'installation de l'acquisition et pour avoir répond á tout mes questions sur le station de test.

Max Chamiot-Clerc,
merci pour avoir rafraichi mes connaissances en électronique. C'est sympa que tu as pris le temps pour éclaircir !

Mathieu & Luca,
ce n'était pas toujours facile pour faire le design de Feather M0 et M2, mais enfin Feather M0.4 a marché et a obtenu l'objectif! Je souhait que le projet Feather M2 va marcher beaucoup plus fluide.

The entire EUCARD-2 team,
which have inspired me during the many project meetings

And off course all my colleagues which I did not mention. It had a fantastic time being part of the team!

Appendix A Derivation analytic equation combined current

The cable current redistribution model is given by:

$$\frac{dI}{dt} = \alpha \frac{d^2 I}{dx^2} \quad \text{with } \alpha = \frac{r}{2\mathcal{M}} = \frac{r}{2(l-m)}. \tag{A.1}$$

The transport current I is assumed to be constant and initially distributed evenly over the number of strands n:

$$\sum_{i=1}^{i=n} \frac{dI}{dt} = 0; \tag{A.2}$$

$$I_i(0,x) = \frac{I}{n}. \tag{A.3}$$

To simplify the joint resistance R_j is neglected. Since the strands are in parallel, the voltage over all the strands need to be equal toV_tot:

$$V_i(x=L,t) = V_j(x=L,t) \text{ with: } i,j = 1..n. \tag{A.4}$$

The analysis is again limited to the 3 strand model. The quench occurs at $x=0$ of strand 2 and has a constant resistance R_Q:

$$V_i(x) = \int_{x=0}^{x} (l-m)\frac{dI_i}{dt}dx + \begin{cases} R_Q\left[\frac{I}{3} + I(0,t)\right] & \text{for: } i=2 \\ 0 & \text{for: } i=1,3 \end{cases} \tag{A.5}$$

Since the joint resistances are neglected, the distribution at the end of the cable should be zero:

$$\left.\frac{dI}{dx}\right|_{x=L} = 0. \tag{A.6}$$

The second boundary condition is obtained by substituting Equation A.5 in Equation A.4. Rearranging gives:

$$\int_{x=0}^{x} (l-m)\frac{dI_2}{dt}dx + RI(0,t) = \int_{x=0}^{x} (l-m)\frac{dI_1}{dt}dx. \tag{A.7}$$

Substituting Equation A.1 and Equation A.2 into Equation A.7 for $n=3$ and rearranging gives:

$$-\frac{3}{4}r\int_{x=0}^{x} \frac{d^2 I_2}{dx^2}dx = R_Q I_2(0,t). \tag{A.8}$$

Solving the integral and using the boundary condition of Equation A.6:

$$\frac{3}{4}r\left.\frac{dI_2}{dx}\right|_{x=0} = R_Q I_2(0,t), \tag{A.9}$$

which is used as the second boundary condition.

The equations can now be made dimensionless by:

$$\tilde{I}_i = \frac{nI_i}{I}; \qquad \tilde{V}_i = \frac{nV_i}{RI}; \qquad \tilde{x} = \frac{x}{L}; \qquad \tilde{t} = \frac{\alpha t}{L^2}; \qquad \mathcal{R} = \frac{4RL}{3r}. \tag{A.10}$$

The normalized differential equation is now given by:

$$\frac{d\tilde{I}}{d\tilde{t}} = \frac{d^2\tilde{I}}{d\tilde{x}^2}. \tag{A.11}$$

Separation of variables can be used to find the following solution, obeying the boundary conditions:

$$\begin{aligned}\tilde{I}(\tilde{x},\tilde{t}) &= \sum_{m=1}^{\infty} C_m \left[\cos\lambda_m \tilde{x} + \tan\lambda sin\lambda\tilde{x}\right] e^{-\lambda_m t} \\ &= \sum_{m=1}^{\infty} C_m \cos\lambda_m (1-\tilde{x}) e^{-\lambda_m t},\end{aligned}$$

with the eigenvalue problem:

$$\frac{\mathscr{R}}{\lambda_m} = \tan\lambda_m. \tag{A.12}$$

In order to agree with the boundary conditions, the following equation needs to be solved:

$$\tilde{I}(\tilde{x},0) = \sum_{m=1}^{\infty} C_m \cos\lambda_m (1-\tilde{x}) = 1. \tag{A.13}$$

To solve this initial heat problem, a variable $y = 1 - x$ is introduced. Now by multiplying both sides by $\sin\lambda_n\tilde{x}$ and integrating over y from 1 to 0, the following expression is obtained:

$$\int_{y=1}^{0} \cos\lambda_n y dy = \sum_{m=1}^{\infty} C_m \int_{y=1}^{0} \cos\lambda_m y \cos\lambda_n y \mathrm{d}y. \tag{A.14}$$

By evaluating the right side, it is found:

$$\sum_{m=1}^{\infty} C_m \int_{y=1}^{0} \cos\lambda_m y \cos\lambda_o y \mathrm{d}y = \begin{cases} -\frac{1}{2\lambda_m}\left[\lambda_m + \frac{\sin 2\lambda_m}{2}\right] & \text{for: } m = o \\ -\frac{\lambda_m \sin\lambda_m \cos\lambda_o - \lambda_o \cos\lambda_m \sin\lambda_o}{\lambda_m^2 - \lambda_o^2} & \text{for: } m \neq o \end{cases} \tag{A.15}$$

By evaluating the eigenvalue condition of Equation A.12, it is found the expression of Equation A.15 is zero for $m \neq o$. Equation A.14 can now be written as:

$$-\frac{1}{\lambda_m}\sin\lambda_m = -\frac{C_m}{2\lambda_m}\left[\lambda_m + \frac{\sin 2\lambda_m}{2}\right]. \tag{A.16}$$

Thereby C_m can be found as:

$$C_m = \frac{4\sin\lambda_m}{2\lambda_m + \sin 2\lambda_m}. \tag{A.17}$$

Resulting in the expression for the current redistribution of strand i:

$$\tilde{I}(\tilde{x},\tilde{t}) = \sum_{m=1}^{\infty} \frac{4\sin\lambda_m}{2\lambda_m + \sin 2\lambda_m} \cos\lambda_m (1-\tilde{x}) e^{-\lambda\tilde{t}}. \tag{A.18}$$

The voltage at position x is given by:

$$\tilde{V}_2(\tilde{x},\tilde{t}) = -\frac{2r}{3\mathscr{R}} \sum_{m=1}^{\infty} \left[C_m\lambda_m \left(\sin\lambda_m(1-\tilde{x}) - \sin\lambda_m\right) e^{-\lambda_m^2 t}\right] + \sum_{m=1}^{\infty} C_m \cos\lambda_m e^{-\lambda\tilde{t}}; \tag{A.19}$$

$$\tilde{V}_1(\tilde{x},\tilde{t}) = \frac{r}{3\mathscr{R}} \sum_{m=1}^{\infty} \left[C_m\lambda_m \left(\sin\lambda_m(1-\tilde{x}) - \sin\lambda_m\right) e^{-\lambda_m^2 t}\right]. \tag{A.20}$$

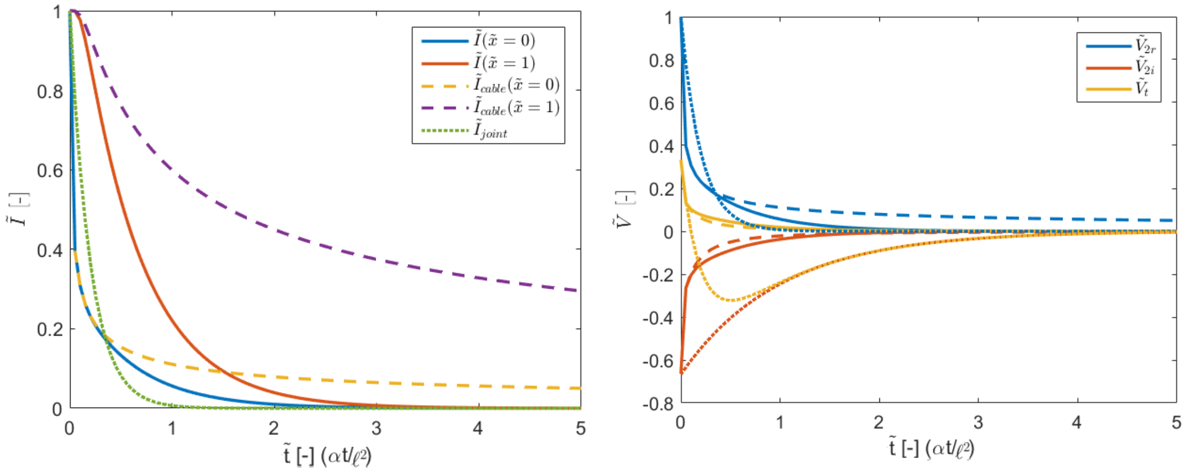

Figure A.1: Comparison of the three analytical redistribution models: Dimensionless current distribution versus location for various time instants at $\tilde{x} = 0$ and $\tilde{\mathrm{I}} = 0$ (left) and the dimensionless resistive $\tilde{V}_{r2}$ and inductive voltage $\tilde{V}_{i2}$ of the quench strand # 2 and the total voltage over the magnet V_i versus time (right). The joint (short striped), cable (long striped) and combined model (continuous) are compared for $\mathscr{R} = 5$.

Appendix B Magnetic field model

In order to approximate the Roebel geometry of the cable, tape i can be divided into m conductor elements with length $d\ell$ as shown in Figure Figure B.1. The tape is reduced to a simple line element which carries current I. A local coordinate system is introduced in the center of the element $[x, y, z]$. The magnetic field of element k of strand i in its local axis with finite length $d\ell$ is given by:

$$B_{ik}(x, y, z, I) = \frac{\mu_0}{4\pi R}(\sin\alpha_1 - \sin\alpha_2)I, \tag{B.1}$$

with R connecting the middle of the wire with the point in space (x, y, z):

$$R(x, y, z) = \sqrt{x^2 + y^2 + z^2}. \tag{B.2}$$

The angles α_1 and α_2 are respectively given by:

$$\alpha_1 = \arctan\left(\frac{z - d\ell}{2\sqrt{x^2 + y^2}}\right); \qquad \alpha_2 = \arctan\left(\frac{z + d\ell}{2\sqrt{x^2 + y^2}}\right). \tag{B.3}$$

By assuming the element length to be small, the magnetic field can be approximated spherical. Following the biot Savart-law (Equation 4.3), the field is pointing perpendicular to the wire $d\ell$ and the vector R. Hence, the field in y-direction can now be found by:

$$B_y = -B\frac{\sqrt{x^2 + z^2}}{R}; \tag{B.4}$$

The Roebel geometry in 2 dimensions consists of straight conductors which are rotated with respect to each other, as shown in Figure B.2. The global coordinate system of the cable is defined by $[X, Y, Z]$, with the local

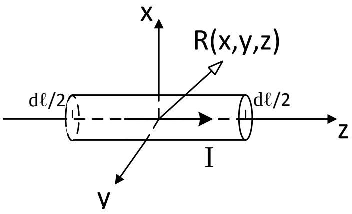

Figure B.1: Conductor element with length ℓ carrying current I.

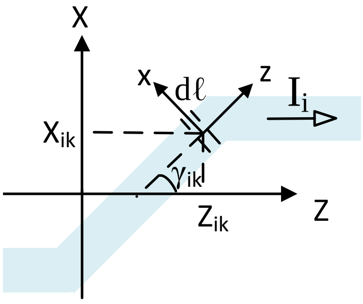

Figure B.2: Conductor element with length ℓ in Roebel cable. The local coordinate system of the element $[x, y, z]$ is rotated by angle γ_{ik} and transposed by $[X_i, Y_i, Z_i]$ in the global coordinate system $[X, Y, Z]$.

Property	Value	Description
$d\ell$	1 mm	Element length
p	11	Field elements in x-direction
q	11	Field elements in y-direction
r	100	Field elements in z-direction
X	[-5,5] mm	Field range x-direction
Y	[-5, 5] mm	Field range y-direction
Z	[$-2\ell_{tp}$,$2\ell_{tp}$]	Field range z-direction

Table B.1: Parameters used for magnetic model calculations.

origin of the conductor element of strand i located at $[X_{ik}, Y_{ik}, Z_{ik}]$ and rotated by γ_{ik}. Hence, rotation matrix $\mathbf{R_z}$ is introduced:

$$\mathbf{R_z}(\gamma) = \begin{bmatrix} \cos\gamma & 0 & \sin\gamma \\ 0 & 1 & 0 \\ -\sin\gamma & 0 & \cos\gamma \end{bmatrix}. \tag{B.5}$$

The transformation between global and local coordinates of element x_{ik} is found by:

$$\mathbf{x}_{ik} = \mathbf{R}^{-1} \begin{bmatrix} X - X_k \\ Y - Y_k \\ Z - Z_k - \frac{\ell_{tp}}{n} i \end{bmatrix}. \tag{B.6}$$

with total strands n in the cable. The 3D magnetic field is described by a grid with $u \times v \times w$ elements spanning $[X, Y, Z]$. The grid is transformed using Equation B.6 to local coordinates, which can be used to calculate the magnetic field at its y-component by Equation B.1 and Equation B.4 respectively. The magnetic field of the cable is found by summing all the conductor elements of a each tape:

$$B_{pqr} = \sum_{i=0}^{n-1} \sum_{k=0}^{r} B_y(\mathbf{x}_{ik}, I_i). \tag{B.7}$$

The model parameters used in calculating the magnetic fields is shown in Table B.1.

Appendix C State space equation numerical model

The state space equation of the electric model is given by:

$$
\begin{bmatrix}
A_{11}^{11} & \dots & A_{11}^{n-11} & A_{11}^{n2} & \dots & A_{11}^{n-2m} & A_{11}^{a} & A_{11}^{b} \\
\vdots & \ddots & \vdots & \vdots & \ddots & \vdots & \vdots & \\
A_{n-11}^{11} & \dots & A_{n-11}^{n-11} & A_{n-11}^{n2} & \dots & A_{n-11}^{n-2m} & A_{n-11}^{a} & A_{n-11}^{b} \\
A_{12}^{11} & \dots & A_{12}^{n-11} & A_{12}^{n2} & \dots & A_{12}^{n-2m} & A_{12}^{a} & A_{12}^{b} \\
\vdots & \ddots & \vdots & \vdots & \ddots & \vdots & \vdots & \\
A_{n-2m}^{11} & \dots & A_{n-2m}^{n-11} & A_{n-2m}^{n2} & \dots & A_{n-2m}^{n-2m} & A_{n-2m}^{a} & A_{n-2m}^{b} \\
A_{ab}^{11} & \dots & A_{ab}^{n-11} & A_{ab}^{12} & \dots & A_{ab}^{n-2m} & A_{b}^{a}+A_{a}^{a} & A_{a}^{b}+A_{b}^{b} \\
0 & \dots & \dots & \dots & \dots & 0 & 1 & 1
\end{bmatrix}
\begin{bmatrix}
i_{11} \\ \vdots \\ i_{n-11} \\ i_{12} \\ \vdots \\ i_{n-2m} \\ \dot{I}_a \\ \dot{I}_b
\end{bmatrix}
+
\begin{bmatrix}
B_{11}^{11} & \dots & B_{11}^{n-11} & B_{11}^{n2} & \dots & B_{11}^{n-2m} & B_{11}^{a} & B_{11}^{b} \\
\vdots & \ddots & \vdots & \vdots & \ddots & \vdots & \vdots & \\
B_{n-11}^{11} & \dots & B_{n-11}^{n-11} & B_{n-11}^{n2} & \dots & B_{n-11}^{n-2m} & B_{n-11}^{a} & B_{n-11}^{b} \\
B_{12}^{11} & \dots & B_{12}^{n-11} & B_{12}^{n2} & \dots & B_{12}^{n-2m} & B_{12}^{a} & B_{12}^{b} \\
\vdots & \ddots & \vdots & \vdots & \ddots & \vdots & \vdots & \\
B_{n-2m}^{11} & \dots & B_{n-2m}^{n-11} & B_{n-2m}^{n2} & \dots & B_{n-2m}^{nm} & B_{n-2m}^{a} & B_{n-2m}^{b} \\
B_{ab}^{11} & \dots & B_{ab}^{n-11} & B_{ab}^{12} & \dots & B_{ab}^{nm} & B_{b}^{a}+B_{a}^{a} & B_{a}^{b}+B_{b}^{b} \\
0 & \dots & \dots & \dots & \dots & 0 & 0 & 0
\end{bmatrix}
\begin{bmatrix}
\imath_{11} \\ \vdots \\ \imath_{n-11} \\ \imath_{12} \\ \vdots \\ \imath_{n-2m} \\ I_a \\ I_b
\end{bmatrix}
=
\begin{bmatrix}
v_{11} \\ \vdots \\ v_{n-11} \\ v_{12} \\ \vdots \\ v_{n-2m} \\ I_a \\ I_b
\end{bmatrix}
. \tag{C.1}
$$

with transformation matrix **T** as:

$$
\begin{bmatrix}
I_{11} \\ I_{21} \\ I_{31} \\ \vdots \\ I_{n-11} \\ I_{n1} \\ I_{12} \\ I_{22} \\ \vdots \\ I_{n-1m} \\ I_{nm}
\end{bmatrix}
=
\begin{bmatrix}
1 & 0 & 0 & \dots & \dots & \dots & \dots & \dots & 0 & 0 & 1 \\
-1 & 1 & 0 & \ddots & \dots & \dots & \dots & \dots & 0 & 0 & 0 \\
0 & -1 & 1 & \ddots & \ddots & \dots & \dots & \dots & \vdots & \vdots & \vdots \\
\vdots & \ddots & \ddots & \ddots & \ddots & \dots & \dots & \dots & \vdots & \vdots & \vdots \\
\vdots & \ddots & \ddots & \ddots & 1 & 0 & 0 & \dots & 0 & 0 & 0 \\
\vdots & \ddots & \ddots & \ddots & -1 & 0 & 0 & \dots & 0 & 1 & 0 \\
\vdots & \ddots & \ddots & \ddots & 0 & 1 & 0 & \dots & 0 & 0 & 1 \\
\vdots & \ddots & \ddots & \ddots & 0 & -1 & 1 & \dots & 0 & 0 & 0 \\
\vdots & \ddots & \ddots & \ddots & \dots & \ddots & \ddots & \ddots & \vdots & \vdots & \vdots \\
\vdots & \ddots & \ddots & \ddots & \dots & \dots & \dots & \dots & -1 & 0 & 0 \\
0 & \dots & \dots & \dots & \dots & \dots & \dots & \dots & 0 & 0 & 1
\end{bmatrix}
\begin{bmatrix}
i_{11} \\ i_{21} \\ i_{31} \\ \vdots \\ i_{n-21} \\ i_{n-11} \\ i_{12} \\ i_{22} \\ \vdots \\ i_{n-2m} \\ i_{n-2m}
\end{bmatrix}
. \tag{C.2}
$$

And the various components of matrix **A** and **B** of Equation C.1 are found by:

$$
\begin{aligned}
A_{ij}^{kl} &= M_{ij,kl} - M_{ij,k+1l} - M_{i+1j,kl} + M_{u+1j,k+1l}\,;\\
A_{ij}^{a} &= A_{a}^{ij} = \sum_{l=1}^{m} M_{ij,1l} - M_{i+1j,1l}\,;\\
A_{ij}^{b} &= A_{b}^{ij} \sum_{l=1}^{m} (M_{ij,nl} - M_{i+1j,nl})\,;\\
A_{ab}^{ij} &= \sum_{k=1}^{n-1} (M_{1j,kl} - M_{1j,k+1l} - M_{nj,kl} + M_{nj,k+1l})\,;\\
A_{a}^{a} &= \sum_{l=1}^{m} \sum_{j=1}^{n} M_{1j,1l}\,;\\
A_{a}^{b} &= A_{b}^{a} = \sum_{l=1}^{m} \sum_{j=1}^{n} M_{1j,1l}\,;\\
A_{b}^{b} &= \sum_{l=1}^{m} \sum_{j=1}^{n} M_{nj,nl}\,;
\end{aligned}
$$

$$
B_{ij}^{kl} = \begin{cases} 2R_j & \text{for } j = l = 1 \vee m, i = k\,;\\ -R_j & \text{for } j = l = 1 \vee m, i = k-1 \vee k+1\,;\\ 0 & \text{else}\,. \end{cases} \qquad + \begin{cases} R_c & \text{for } i = k, j = l = 1 \vee m;\\ 2R_c & \text{for } i = k, j = l \neq 1 \vee m;\\ -R_c & \text{for } i = k, j = l-1 \vee l+1\,;\\ 0 & \text{else }. \end{cases};
$$

$$
B_{ij}^{a} = B_{a}^{ij} = \begin{cases} R_j & \text{for } i = 1\,;\\ 0 & \text{else}\,. \end{cases}
$$

$$
B_{ij}^{a} = B_{a}^{ij} = \begin{cases} -R_j & \text{for } i = n-1;\\ 0 & \text{else} \end{cases};
$$

$$
B_{ab}^{ij} = \begin{cases} R_j & \text{for } i = 1;\\ -R_j & \text{for } i = n-1;\\ 0 & \text{else} \end{cases}
$$

$$
\begin{aligned}
B_{a}^{a} &= B_{b}^{b} = 2R_j\\
B_{a}^{b} &= B_{b}^{a} = 0
\end{aligned}
$$

Appendix D Sweep results

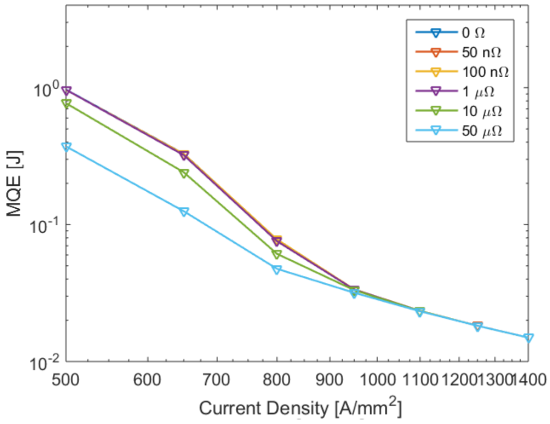

Figure D.1: Numerically found MQE versus current density for various joint resistances. Increasing the joint resistance allows less redistribution over the joint, which is mainly present for low current densities. Hence al low current densities, a lower stability is visible after the resistance has significantly increased. (Standard value ≈ 50 nΩ [for Feather M0.4])

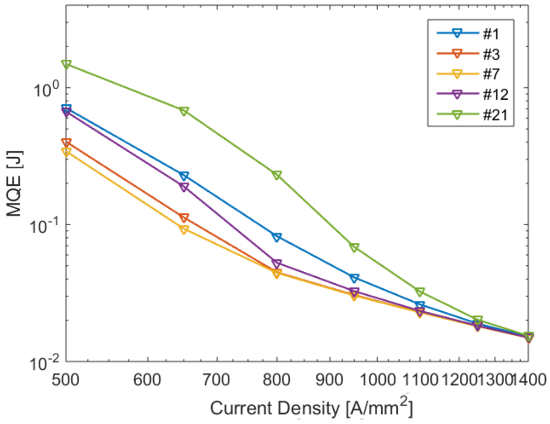

Figure D.2: MQE versus current density for various quench locations (current element 10 is the center of the coil). The magnet shows reduced stability when nearing the center of the coil. Note the asymmetry between element 1-21, the two leads of the dipole. The upper deck have a significantly higher stability, presumably due to its smaller dimensions.

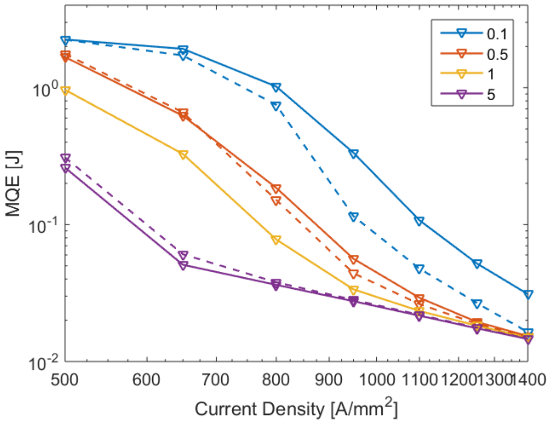

Figure D.3: Numerically found MQE versus current density to show the analogy of the model with respect to induction (continuous) and interstrand contact resistance (dotted). The parameter r_c and the induction matrix are subsequently scaled by the scaling factor shown in the legend, while the other parameter is kept constant.

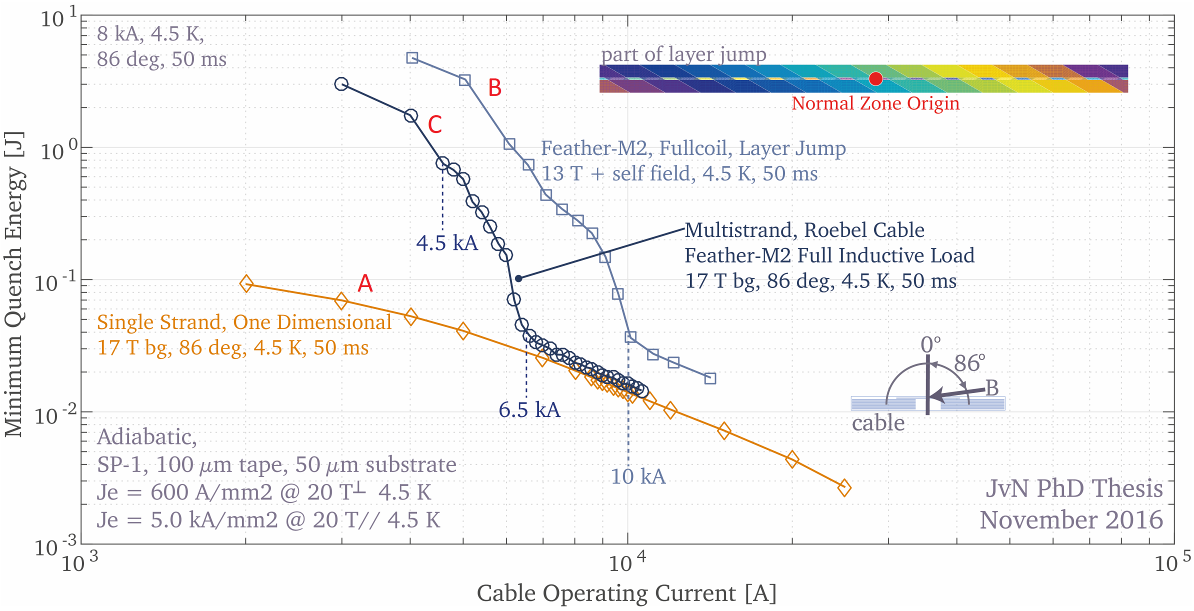

Figure D.4: MQE versus current density J found by the 3D model [9] for a single tape (A), the cable model without cable redistribution (C) and fixed magnetic background field and the full magnet (B). For qualitative validation of the quench behaviour described by the presented 2D model. The models are both based on the tape model, hence the basis of both models is comparable.

Appendix E Data aqcuisition and quench detection program

E.1. HARDWARE

To perform quench detection for future HTS magnets, stand-alone embedded system was developed. Since quench detection has to be reliable and have a fast reaction time, a compact Reconfigurable Input Output (cRIO) was chosen. As shown in figure E.1, the cRIO-9086 includes the following features:

1. Field programmable gate array (FPGA)
2. Dual Core Real Time processor (RT)
3. Chassis with 8 module slots, containing:
    - 7x NI 9205 32-channel analogue input (AI) module
    - 1x NI 9401 8-channel digital input/output (DIO)
4. USB-B for external hard disk (HD)

The cRIO can be used as autonomous embedded system. The combination of the FPGA and the RT-processor offer the ability for reliable operation with fast response. The cRIO was envisioned as a auxiliary detection module for future HTS magnets in the existing test station. Details of the test station can be found in chapter 4.

E.2. SOFTWARE

The program serves as basis for future magnet data aqcuisition and quench detection, while using the available resources as efficient as possible. The software is written within modular sub-programs, each component is coded with a distinctive task as shown in Figure Table E.2. The cRIO is programmed in Labview and consists of three levels: Host, RT and FPGA. The RT application is deployed on the RT processor which operates on Linux Real Time OS. The FPGA program is converted by the Xilinx compiler eventually into bitfiles, which implements the logic blocks on the FPGA chip.

The two following definitions are used within the following paragraph: [74]

1. Clock time: Time of a single hardware computation cycle
2. Sample time: Time between 2 measurement samples, inverse of the sampling frequency
3. Loop time: Interval in which a operation is repeated
4. Loop duration: Time to perform the operation inside a loop

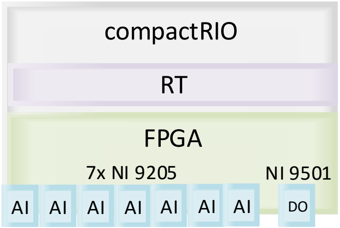

Figure E.1: cRIO Hardware overview consisting of the RT and the FPGA, which has direct access to the analogue input and digital output modules

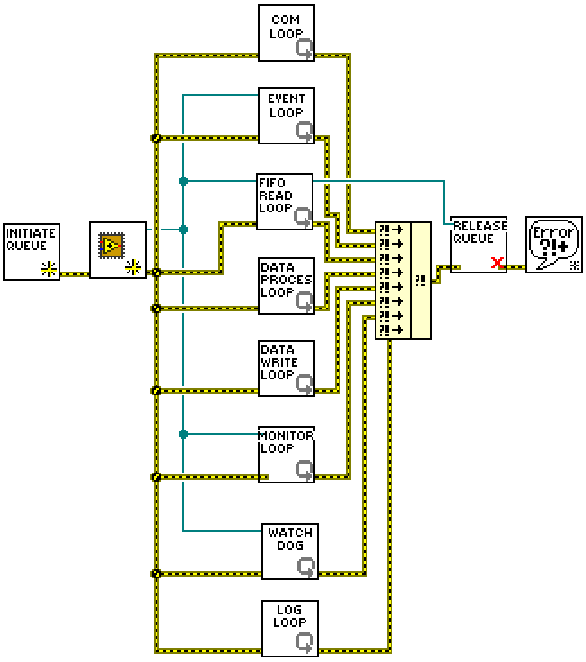

Figure E.2: RT DAQ program, showing the modularity. From left to right top to bottom: Initiation of the DAQ (left), including start of acquisition by the FPGA. The function blocks in the center form the main operations, with communication with the host computer and event operator as master operations (top two blocks). Followed by read from FPGA, data processing, write and monitoring of de data. The watchdog checks if the RT processor is still response, and takes appropriate action if latency is unacceptable. The log loop records all operations performed by the RT processor with a time stamp. Subsequently, if the program is closed, the operations such as returning allocated memory are performed.

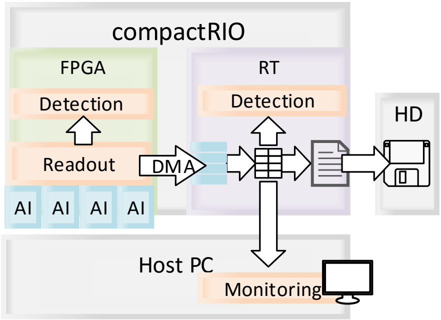

Figure E.3: Aqcuisition overview, showing the flow of data in the cRIO. The data is read by the FPGA and send via the DMA to the RT for quench detection. In the RT the data is processed and saved to the harddisk. Additionally, the RT resamples the data for monitoring on the host computer.

E.2.1. DATA ACQUISITION

The primary goal for the cRIO is to record data for all of its channels. This data can later be used for studying the magnet's behaviour and quench detection design. The requirements for the cRIO programming are:

1. Acquiring data for at least 8 hours with a channel dependent frequency
2. High reliability, minimized data loss
3. Autonomous system with real time monitoring
4. Synchronized with parallel DAQ systems

The data acquisition overview is shown in figure E.3. The FPGA and RT both contribute to acquiring and storing the measurement data. The analogue input signals from the magnet enter the cRIO via one of the input modules. The inputs are directly accessed by the FPGA, which samples the data and sends the data to the RT via a Direct Memory Access First In First Out (DMA FIFO). The data is sampled with two frequencies: 100 Hz and 10 kHz, which both operate in parallel.

A DMA FIFO handles the measurement data communication between the RT and FPGA. The DMA has the advantage of not loading the RT processor during a data transfer. It is the most efficient way to communicate data arrays between RT and FPGA [74]. Since the DMA interface between FPGA and RT can be temporarily overloaded or temporarily not accessible for any reason, the FPGA can store a number of samples internally in an intermediate FIFO. These samples are retained until the DMA becomes accessible, after which they are offered to the DMA in chronological order. If the intermediate buffer of 1023 samples is filled and the DMA is still not accessible, this intermediate buffer is erased and the user is notified of the loss of data.

The data acquisition of the RT FIFO is split in three main operations: Read, processing and write. These operations are split in different loops as shown in Table E.2, since:

1. The cRIO-9068 contains 2 RT-processors, therefore operations can be performed in parallel.
2. RT timed loop containing quench detection should contain a minimum amount of operations to preserve determinism.
3. Writing and reading operations depend on external components (DMA and Hard disk), which can form bottleneck.

The RT reads the measurement data through the DMA FIFO. To limit the CPU usage, the data is buffered before read-out. Since this read-out is directly used for quench detection, it runs in a RT timed loop. The timed loop ensures timely operation of the quench detection. After the DMA FIFO read out, the time stamp data is added and the array enters a Real Time FIFO. The RT FIFO ensures the deterministic character of the RT FIFO [74].

The RT FIFO is read by a processing loop, which converts the data array to a single format, reshapes it into a matrix and identifies the individual channels. The data is formatted, buffered, and send through a queue to the write loop. Buffering takes place to minimize again the CPU load while handling writing operations. Apart from processing data, the process loop re-samples for real time data monitoring.

The data write loop reads the data from the queue. The sensor data is written to the corresponding binary file and saved on the external hard disk. Binary files were chosen since they have minimal load on the CPU. File sizes are kept to a limit of 10 MB, to limit writing latency. An external post processing tool can convert the data into txt, csv or tdms files.

The acquisition of the data on all 60 channels is performed in parallel, with a nominal CPU load of 15%. The data acquisition does not rely on the host connection. The data acquisition operates in standalone, but can be stopped and started from the host computer if needed.

E.2.2. MONITORING

The RT processor resamples the live data in the process loop for the real time monitoring. The resampled data is bundled before sending to the host to limit data traffic. All signals together with the system's operating state can be monitored in real time from the host computer.

Apart from real time monitoring, reviewing data with full resolution is possible with the post analysis tool. Based on the user's time window, the data is red from the recordings by the read/write module. The post-analysis tool is automatically activated when either the protection is triggered or one of the heaters is fired.

E.2.3. QUENCH DETECTION

Quench detection consists of a digital block averaging with a threshold window comparison as shown in figure E.4. The goal of the current quench detection is to empirically iterate for the detection parameters of different channels during the measurement. Therefore the interface of the host computer offers the possibility to adjust the detection threshold, comparison window and averaging window.

Quench detection is performed both by the real time processor and the FPGA. Simple operations, such as the averaging of small sample sizes are performed on the FPGA to enhance response time, while larger averages

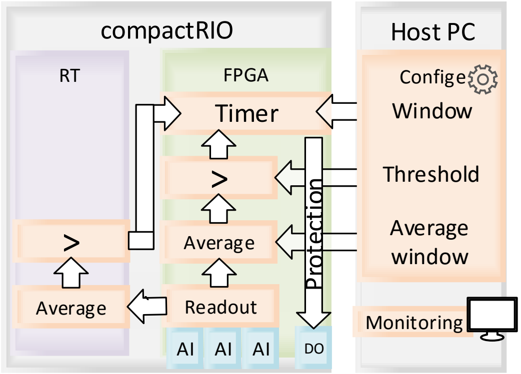

Figure E.4: Detection overview, illustrating the various operations. The white lines show the signal, while the gray arrows depict the configuration from the host PC.

are performed on the RT. The FPGA enables the user to choose averaging between 4, 16 or 64 elements, while larger block sizes are left to the RT.

The averaged value is passed to another part of the FPGA for comparison with a user defined threshold. While the threshold is exceeded, a timer will count the loop cycles. If the threshold is still exceeded after the user defined time window, the detection is triggered. Analogue algorithm is implemented in the RT for larger average blocks. If a quench is detected by either of the systems, a trigger is send to the safety matrix for activation of protection measures, as discussed in Chapter 5.

The quench detection was validated using simulating various signals with a NI-9006 as shown in Figure 5.10. A simple digital signal generator was used to check the detection threshold and window were working properly. The detection time was verified below ms using the FPGA's digital output and internal timing.

Appendix F Measured quench signals

The following figures shows the signals measured by the pick up coils and voltage taps during the quench at 3120 A at 55 K at the August 16th 17:34:

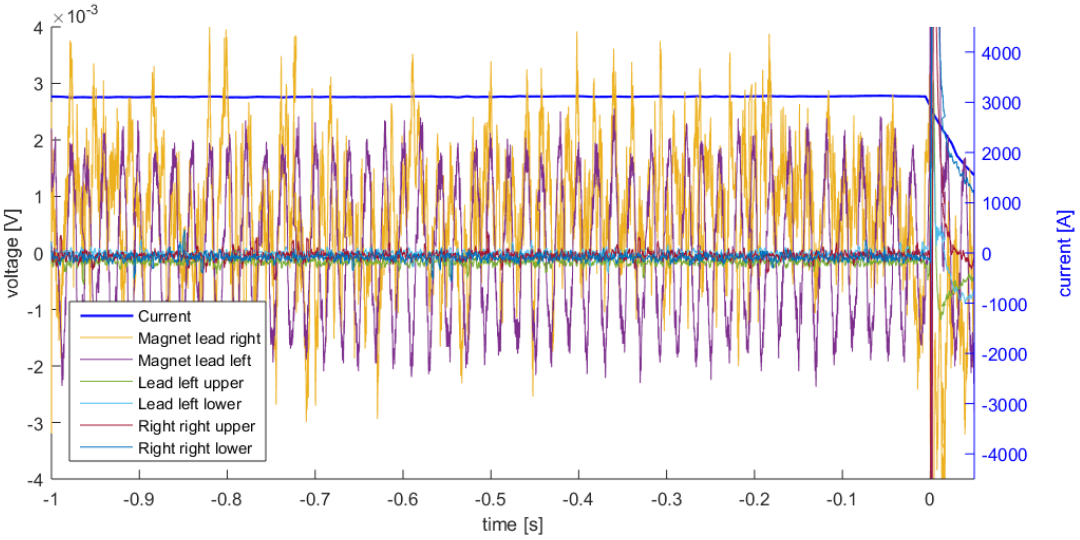

Figure F.1: Pick up signals before and during the quench, found in Table 5.1a

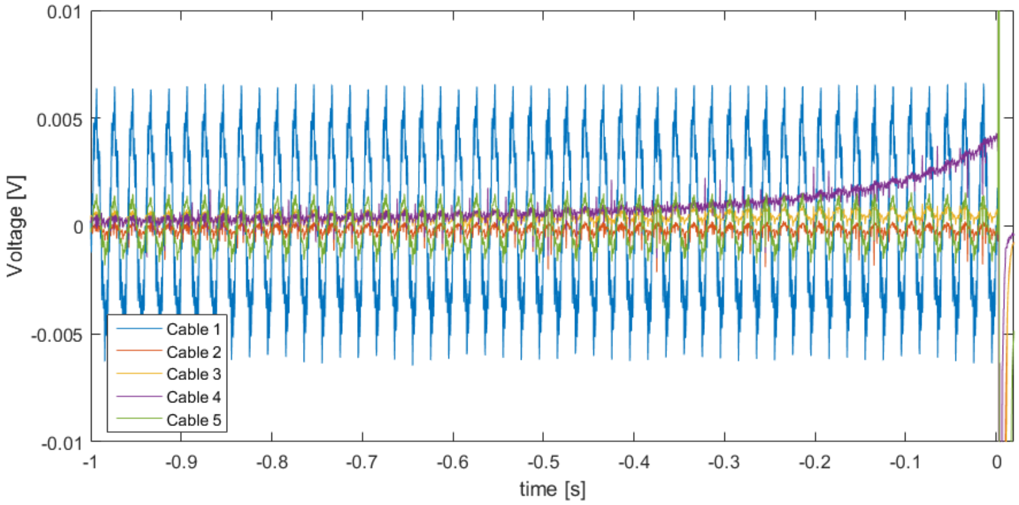

Figure F.2: Voltage tap signals before and during the quench, found in Table 5.4

F.0.1. SIGNAL NOISE BEFORE QUENCH

Care has been taken in the design of the measurement setup and placement of sensors in order to reduce noise. Disturbances from (electro-)magnetic fields cause significantly more noise in sensors inside the magnet. Note the alignment of the pick up coils has significant influence on the overall noise band and the 50 Hz interference, supposedly caused by the power supply.

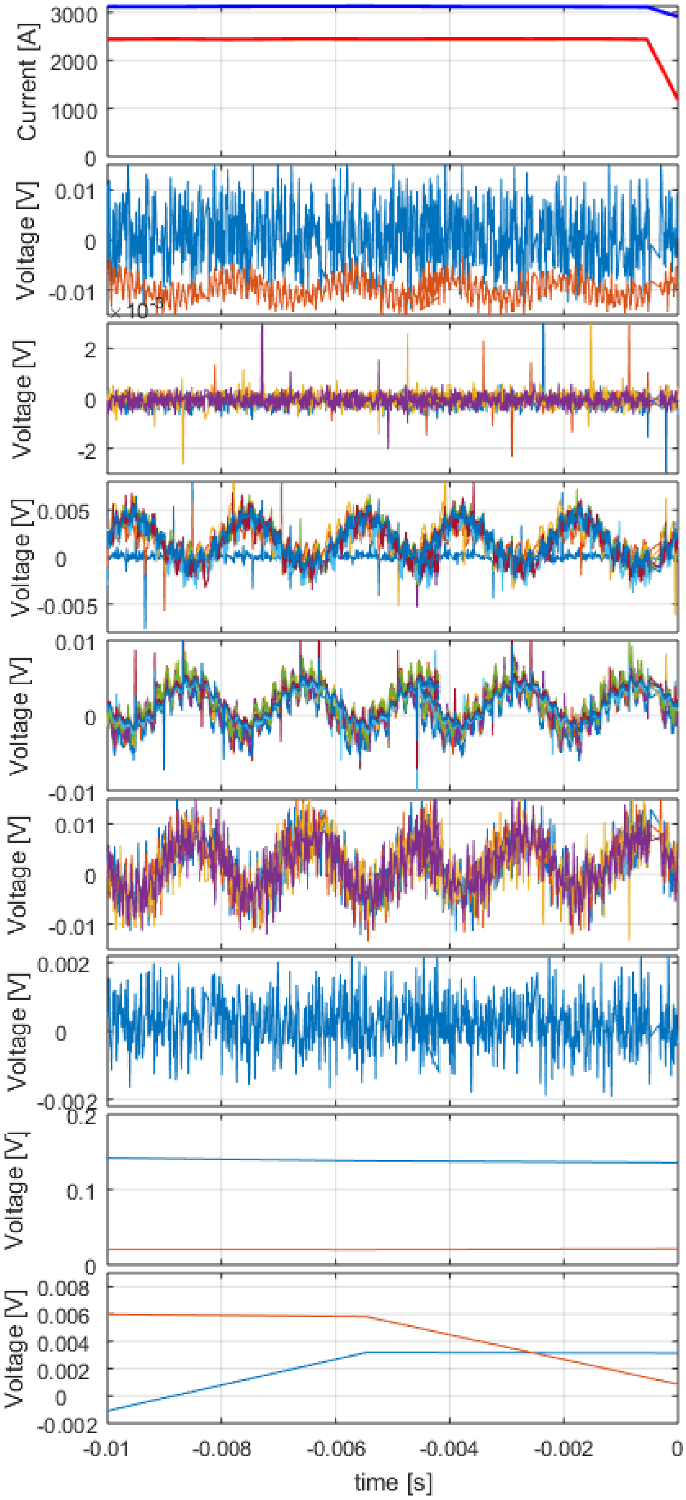

Current (blue, converted) from power supply and **trigger signal** (red, scaled) received from PotAim (100 Hz). At $t = 0$ the protection is triggered by the PotAIM and the current is extracted

Pick up coils at the magnet leads: Both pick up coils show slight 50 Hz noise component. Larger noise band level for right side possibly caused by bad contact.

Pick up coils at extension leads: Submillivolt noise level, presumably since are outside the main magnetic field

Pick up coils inside former right: Noise level dominated by pick up 50 Hz component, except for UPCLR1 (Pick up coil at the top).

Pick up coils inside form left: Similar behaviour compared to pick up coils former right.

Pick up coils in top cap: Both signal 50 Hz and band noise significantly increased; likely to be caused by alignment with the main field.

Hall Probes: Hall probe signal to noise ratio deteriorates for higher currents, due to magnetic field disturbances (Second hall probe out of range, shows similar behaviour)

Calibrated CCS sensor: Calibrated temperature sensor inside the coil shows correct temperature (54 ± 5 K, requires averaging over seconds, CCS at splice shows an unexpected value

CCS temperature array: Temperature arrays pick up high amount of noise. Averaging shows signal correlation with temperature.

F.0.2. SIGNAL DURING QUENCH AND CURRENT EXTRACTION

All signals are cut off at 0.2 V due to the configured voltage range. The pick up coil signals show (with few exceptions) the magnetic field change due the current ramp down. A clear difference between redistributions left and right in the cable is visible in both magnet and extension lead pick up coils. Additionally, a slight time delay is observed between subsequent signals.

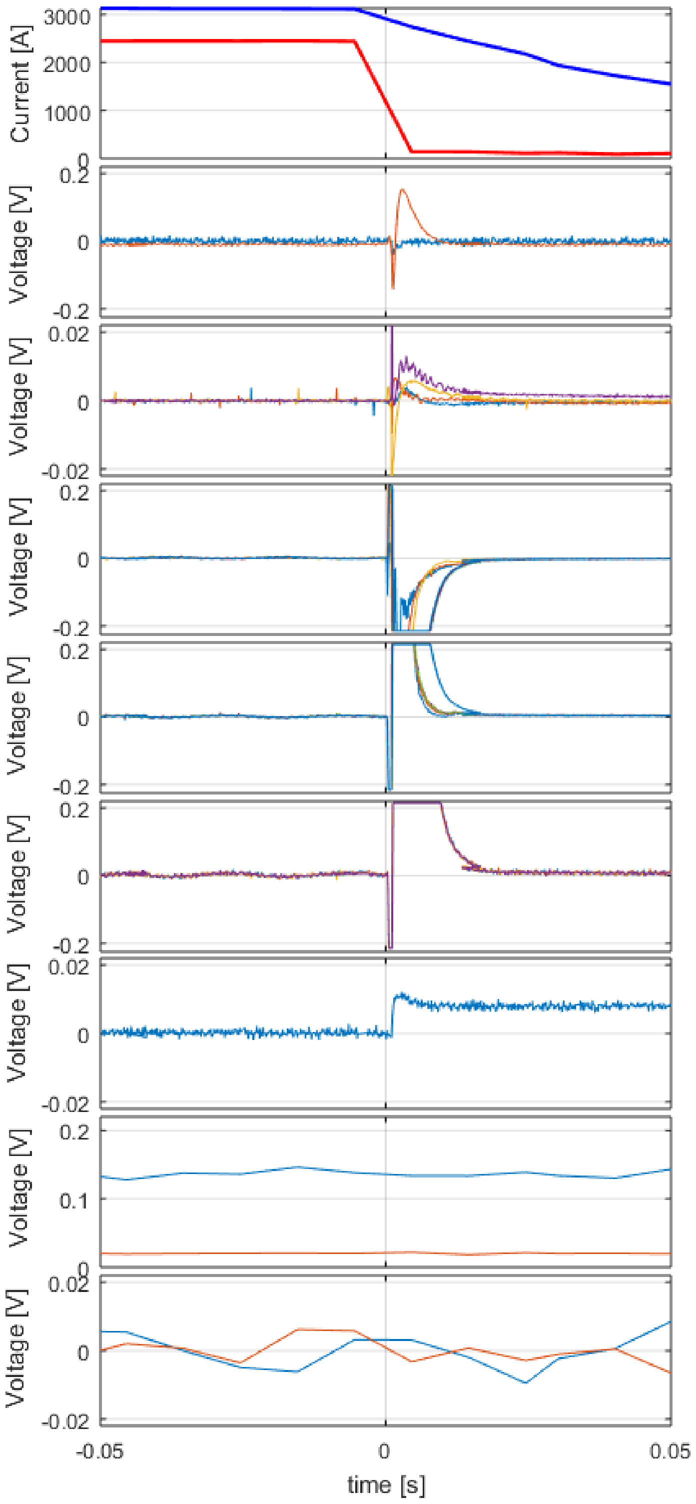

Current (blue, converted) from power supply and **trigger signal** (red, scaled) received from PotAim (100 Hz). At $t = 0$ the protection is triggered by the PotAIM and the current is extracted

Pick up coils at the magnet leads: Left (Red) shows an contrasting signal compared to right (Blue) and the pick up coils at the extension leads.

Pick up coils at extension leads: Left (Purple, yellow) and right (blue red) show distinctive pattern, caused by the inductive effect of the magnet.

Pick up coils inside former right: High peak from extraction in all signals, while the signals show distinctive responses. Pick up coils at the upper layer of the coil show delayed decay.

Pick up coils inside form left: Mirrored behaviour of pick up coils former right.

Pick up coils in top cap: High signal peak during extraction; likely caused by alignment with the main field.

Hall Probes: Hall probe shows a rise when extraction starts, likely due to the change in magnetic field, followed by the current extraction. (Second hall probe out of range, showing same behaviour)

Calibrated CCS sensor: Calibrated temperature sensor inside the coil shows correct temperature (54 ± 5 K, requires averaging over seconds, CCS at splice shows odd value

CCS temperature array: Temperature arrays pick up high amount of noise. Averaging shows signal correlation with temperature.

Appendix G Mutual induction matrices FM0/FM2

11.13	10.83	10.64	10.40	10.11	9.85	9.65	9.50	9.50	9.65	9.85	10.12	10.40	10.64	10.83
10.83	11.13	10.83	10.64	10.39	10.11	9.85	9.65	9.50	9.50	9.65	9.85	10.11	10.40	10.64
10.64	10.83	11.13	10.83	10.64	10.39	10.11	9.85	9.65	9.49	9.49	9.65	9.85	10.11	10.40
10.40	10.64	10.83	11.13	10.82	10.63	10.39	10.10	9.84	9.64	9.49	9.49	9.65	9.85	10.11
10.11	10.39	10.64	10.82	11.12	10.82	10.63	10.38	10.09	9.83	9.63	9.49	9.49	9.64	9.85
9.85	10.11	10.39	10.63	10.82	11.11	10.81	10.62	10.37	10.09	9.83	9.64	9.49	9.49	9.65
9.65	9.85	10.11	10.39	10.63	10.81	11.10	10.80	10.61	10.37	10.09	9.84	9.64	9.49	9.50
9.50	9.65	9.85	10.10	10.38	10.62	10.80	11.10	10.80	10.62	10.38	10.10	9.85	9.65	9.50
9.50	9.50	9.65	9.84	10.09	10.37	10.61	10.80	11.10	10.81	10.63	10.39	10.11	9.86	9.66
9.65	9.50	9.49	9.64	9.83	10.09	10.37	10.62	10.81	11.11	10.82	10.64	10.40	10.12	9.86
9.85	9.65	9.49	9.49	9.63	9.83	10.09	10.38	10.63	10.82	11.12	10.83	10.65	10.40	10.12
10.12	9.85	9.65	9.49	9.49	9.64	9.84	10.10	10.39	10.64	10.83	11.13	10.84	10.65	10.41
10.40	10.11	9.85	9.65	9.49	9.49	9.64	9.85	10.11	10.40	10.65	10.84	11.14	10.84	10.65
10.64	10.40	10.11	9.85	9.64	9.49	9.49	9.65	9.86	10.12	10.40	10.65	10.84	11.14	10.84
10.83	10.64	10.40	10.11	9.85	9.65	9.50	9.50	9.66	9.86	10.12	10.40	10.65	10.84	11.13

Table G.1: Mutual Induction Feather M0 [9]

463.8	459.0	456.1	452.7	448.9	445.2	442.1	439.6	439.6	442.1	445.1	448.7	452.6	456.0	459.0
459.0	463.8	459.0	456.1	452.7	448.8	445.2	442.2	439.6	439.6	442.1	445.2	448.8	452.7	456.0
456.1	459.0	463.8	459.0	456.1	452.7	448.9	445.3	442.3	439.7	439.7	442.2	445.3	449.0	452.7
452.7	456.1	459.0	463.9	459.1	456.1	452.8	449.0	445.5	442.4	439.8	439.8	442.3	445.4	448.9
448.9	452.6	456.1	459.1	463.9	459.1	456.2	452.9	449.1	445.5	442.4	439.8	439.8	442.3	445.3
445.2	448.8	452.7	456.1	459.1	463.9	459.1	456.3	452.9	449.1	445.4	442.3	439.7	439.7	442.2
442.1	445.2	448.9	452.7	456.2	459.1	464.0	459.2	456.3	452.9	449.0	445.3	442.2	439.6	439.6
439.5	442.1	445.3	449.0	452.9	456.3	459.2	464.1	459.3	456.3	452.8	448.9	445.3	442.2	439.6
439.6	439.6	442.3	445.4	449.1	452.9	456.3	459.3	464.1	459.2	456.1	452.7	448.8	445.2	442.1
442.1	439.6	439.7	442.4	445.5	449.1	452.9	456.3	459.2	463.9	459.0	455.9	452.5	448.7	445.1
445.1	442.1	439.7	439.8	442.4	445.4	449.0	452.8	456.1	459.0	463.7	458.8	455.8	452.5	448.7
448.7	445.2	442.2	439.8	439.8	442.3	445.4	448.9	452.7	456.0	458.8	463.6	458.8	455.9	452.5
452.6	448.8	445.3	442.3	439.8	439.7	442.2	445.3	448.8	452.6	455.9	458.8	463.6	458.9	455.9
456.0	452.7	449.0	445.4	442.3	439.7	439.7	442.2	445.3	448.8	452.5	455.9	458.9	463.7	458.9
459.0	456.0	452.7	449.0	445.3	442.2	439.6	439.6	442.1	445.2	448.7	452.5	455.9	458.9	463.8

Table G.2: Mutual Induction Feather M2 [9]

Bibliography

[1] S. Wiegers *et al.*, *Design and construction of a 38 t resistive magnet at the nijmegen high field magnet laboratory,* IEEE Transactions on Applied Superconductivity **22**, 4301504 (2012).

[2] O. Bruning, *LHC Design Report* (CERN, Geneva, 2004).

[3] L. Rossi *et al.*, *The eucard-2 future magnets european collaboration for accelerator-quality hts magnets,* IEEE Transactions on Applied Superconductivity **25**, 1 (2015).

[4] E. Todesco *et al.*, *Magnets for hl-lhc,* Cern Document Server (2014).

[5] D. Tommasini, ed., *EU/CERN program on 16T dipoles for the FCC,* FCCW2016, Roma (2016).

[6] G. Kirby *et al.*, *Accelerator Quality HTS Dipole Magnet Demonstrator Designs for the EuCARD-2, 5 Tesla 40 mm Clear Aperture Magnet,* IEEE Transactions on Applied Superconductivity **25** (2015).

[7] G. Kirby *et al.*, *First cold powering test of rebco roebel wound coil for the eucard2 future magnet development project,* (Due for publishing in March 2017 ASC).

[8] G. Kirby *et al.*, *Status of the Demonstrator Magnets for the EuCARD-2 Future Magnets Project,* **26** (Due for publishing in March 2017 ASC).

[9] J. van Nuchteren, *High Temperature Superconductor Accelerator Magnets*, Ph.D. thesis, University of Twente (due to 2017).

[10] J. Murtomaki, ed., *Structural design of HTS magnet for EuCARD-2* (EUCARD-2 3rd Annual Meeting, 2016).

[11] S. Kathiravan *et al.*, *A review on potential issues and challenges in mr imaging,* The Scientific World Journal (2013).

[12] A. Ballarino, *Current leads for the lhc magnet system,* IEEE Transactions on Applied Superconductivity **12**, 1275 (2002).

[13] K. Ding *et al.*, *Results of the testing of iter cc hts current lead prototypes,* IEEE Transactions on Applied Superconductivity **26**, 1 (2016).

[14] A. Ballarino, *Development of superconducting links for the large hadron collider machine,* Supercond. Sci. Technol. **27**, 044024. 7 p (2014).

[15] P. Tixador, *Development of superconducting power devices in europe,* Physica C: Superconductivity **470**, 971 (2010), proceedings of the 22nd International Symposium on Superconductivity.

[16] K. Kim *et al.*, *Design and performance analysis of a ni-type hts field magnet for superconducting rotating machines,* IEEE Transactions on Applied Superconductivity **25**, 1 (2015).

[17] L. Cooley, ed., *Cost drivers for very high energy p-p collider magnet conductors* (2016).

[18] N. Wilson, *Superconducting Magnets* (Oxford Science Publications, 1983).

[19] K. Mess *et al.*, *Superconducting Accelerator Magnet* (World Scientific, 1996).

[20] Y. Iwasa, *Case Studies in Superconducting Magnets,* 2nd ed. (Springer Science, 2009).

[21] J. van Nuchteren, *Normal Zone Propagation in a YBCO Superconducting Tape,* Master's thesis, University of Twente (2014).

[22] G. Nielsen *et al.*, *Dipole magnet from high tc superconductor,* Physics Procedia **36**, 824 (2012).

[23] M. Tinkham, *Introduction to Superconductivity: Second Edition* (Dover Publications, 2004).

[24] K. Bennemann *et al.*, *Superconductivity: Volume 1: Conventional and Unconventional Superconductors Volume 2: Novel Superconductors* (Springer Berlin Heidelberg, 2008).

[25] P. Lee, *Engineering Superconductivity* (Wiley-IEEE Press, 2001).

[26] C. Chu *et al.*, *Superconductivity above 150 k in $hgba_2ca_2cu_3o_{8+[delta]}$ at high pressures,* Nature **365**, 323 (1993).

[27] A. Verweij, *The 10T dipole magnet of the FRESCA facility: an overview of 6 years of operation*, Tech. Rep. (CERN, 2005).

[28] Dell'Orco *et al.*, *Fabrication and component testing results for a Nb_3Sn dipole magnet,* Applied Superconductivity, IEEE Transactions on **5**, 1000 (1995).

[29] A. Godeke, *Performance boundaries in Nb_3Sn conductors*, Ph.D. thesis, University of Twente (2005).

[30] E. Todesco *et al.*, *Limits to high field magnets for particle accelerators,* IEEE Transactions on Applied Superconductivity **22**, 4003106 (2012).

[31] A. Golovashkin *et al.*, *Low temperature direct measurements of hc2 in htsc using megagauss magnetic fields,* Physica C: Superconductivity **185**, 1859 (1991).

[32] J. Schwartz *et al.*, *High field superconducting solenoids via high temperature superconductors,* IEEE Transactions on Applied Superconductivity **18**, 70 (2008).

[33] T. Sekitani *et al.*, *Upper critical field for optimally-doped ybco,* Physica B Condensed Matter **346-347**, 319 (2004).

[34] G. Willering, *Stability of superconducting Rutherford cables for accelerator magnets*, Ph.D. thesis, University of Twente, Enschede (2009).

[35] L. Coull *et al.*, *Lhc magnet quench protection system,* LHC Note 251 (1994).

[36] J. Fleiter *et al.*, *On roebel cable geometry for accelerator magnet,* EuCARD-2 Publication (2014).

[37] E. Gmelin, *Review: Thermal boundary resistance of mechanical contacts between solids at sub-ambient temperatures,* Physics D: Applied Physics **32** (1999).

[38] J. Ekin, *Experimental techniques for low temperature measurements : cryostat design, materials, and critical-current testing* (Oxford University Press, 2006).

[39] J.Schwartz, *Quench in high temperature superconductor magnets,* CERN Yellow Report (2014).

[40] W. H. Cherry *et al.*, *Thermal and electrodynamic aspects of the superconductive transition process,* Solid-State Electronics **1** (1960).

[41] V. Keilin *et al.*, in *Les Champs Magnetiques Intenses, Paris, CNRS* (1960).

[42] L. Dresner, *Analytic solution for the propagation velocity in superconducting composites,* IEEE Transactions on Magnetics **15**, 328 (1979).

[43] N. Whetstone, *Thermal phase transitions in superconducting $Nb-Zr$ alloys,* Journal of Applied Physics **36** (1965).

[44] M. Bonura *et al.*, eds., *Summary of the latest measurements on REBCO tapes at UNIGE*, WAMHTS-3 (Universite de Geneve, 2015).

[45] L. Bottura *et al.*, *Analytical calculation of current distribution in multistrand superconducting cables,* IEEE Transactions on Applied Superconductivity **13** (2003).

[46] G. Ries, *Stability in superconducting multistrand cables,* Cryogenics **20**, 513 (1980).

[47] B. Turck, *Influence of a transverse conductance on current sharing in a two-layer superconducting cable,* Cryogenics **14**, 448 (1974).

[48] L. Bottura *et al.*, *A general model for thermal, hydraulic and electric analysis of superconducting cables,* Cryogenics **40**, 617 (2000), 4th Workshop on Computation of Thermal Hydraulic Transients in Superconductors.

[49] A. Faghri *et al.*, *Advanced Heat and Mass Transfer* (Global Digital Press, 2010).

[50] A. Mills, *Basic Heat and Mass Transfer* (Pearson Education, 1998).

[51] H. Cheng *et al.*, *A fast adaptive multipole algorithm in three dimensions,* Journal of computational physics **155**, 468 (1999).

[52] J. Fleiter *et al.*, *Characterization of roebel cables for potential use in high-field magnets,* IEEE Transactions on Applied Superconductivity **25**, 1 (2015).

[53] C. Senatore *et al.*, *Field and temperature scaling of the critical current density in commercial rebco coated conductors,* Superconductors Science and Technology **29** (2015).

[54] R. Nakasaki *et al.*, eds., *Continuous improvements in performance and quality of 2G HTS wires produced by IBAD-MOCVD for coil applications* (Superpower, 2015).

[55] W. Markiewicz *et al.*, *Quench analysis of pancake wound rebco coils with low resistance between turns,* Superconductor Science and Technology **29**, 025001 (2016).

[56] K. Tanaka *et al.*, *Development of the current bypassing methods into the transverse direction in non-insulation hts coils,* Physics Procedia **65**, 229 (2015).

[57] H. Bajas, *Private communication,* .

[58] A. Chiuchiolo *et al.*, *Cryogenic temperature profiling of high power superconducting lines using local and distributed optical fiber sensor,* EuCARD-2 Publication (2015).

[59] A. Chiuchiolo, *Cryogenic Fiber Optic Sensors for Superconducting Magnets and Power Transmission Lines in High Energy Physics Applications*, Ph.D. thesis, Sannio U (2015).

[60] A. Chiuchiolo, *Private communication,* .

[61] G. de Rijk, *Private communication,* .

[62] A. Dudarev *et al.*, *New fast response thin film-based superconducting quench detectors,* IEEE Transactions on Applied Superconductivity **24**, 1 (2014).

[63] J. Feuvrier, *Private communication,* ().

[64] A. Fernandez, *Reliability of the Quench Protection System for the LHC Superconducting Elements*, Ph.D. thesis, University Politecnica Catalunya (2003).

[65] F. Borgnolutti *et al.*, *Construction of the cern fast cycled superconducting dipole magnet prototype,* IEEE Trans. Appl. Supercond. **22**, 4001604. 5 p (2012).

[66] M. Marchevsky *et al.*, *Axial-field magnetic quench antenna for the superconducting accelerator magnets,* IEEE Transactions on Applied Superconductivity **25**, 1 (2015).

[67] D. Leroy *et al.*, *Quench observation in lhc superconducting one meter long dipole models by field perturbation measurements,* IEEE Transactions on Applied Superconductivity **3**, 781 (1993).

[68] T. Ogitsu *et al.*, *Quench observation using quench antennas on rhic ir quadrupole magnets,* IEEE Transactions on Applied Superconductivity **32**, 3098 (1996).

[69] T. Ogitsu *et al.*, *Quench antenna for superconducting particle accelerator magnets,* IEEE Transactions on Magnetics **30**, 2273 (1994).

[70] A. Teixeira, *Private communication,* private communication.

[71] M. Bajko *et al.*, *New Cryogenic Test Station at CERN for Superconducting Magnets and their Components*, Tech. Rep. (CERN, Geneva, 2013).

[72] J. Feuvrier, *Private communication,* ().

[73] *Tr14 transient recorder,* (2011).

[74] *Compactrio developers guide,* https://www.ni.com/compactriodevguide/.